Global empirical model of the TEC response to geomagnetic activity and forcing from below

Dora Pancheva
Plamen Mukhtarov
Borislav Andonov

National Institute of Geophysics, Geodesy and Geography
Bulgarian Academy of Sciences
BL. 3 Acad. Georgi Bonchev
Sofia 1000 BULGARIA

Report Date: April 2014

Final Report from 2 April 2012 to 1 April 2014

Air Force Research Laboratory
Air Force Office of Scientific Research
European Office of Aerospace Research and Development
Unit 4515, APO AE 09421-4515

REPORT DOCUMENTATION PAGE

Form Approved OMB No. 0704-0188

Public reporting burden for this collection of information is estimated to average 1 hour per response, including the time for reviewing instructions, searching existing data sources, gathering and maintaining the data needed, and completing and reviewing the collection of information. Send comments regarding this burden estimate or any other aspect of this collection of information, including suggestions for reducing the burden, to Department of Defense, Washington Headquarters Services, Directorate for Information Operations and Reports (0704-0188), 1215 Jefferson Davis Highway, Suite 1204, Arlington, VA 22202-4302. Respondents should be aware that notwithstanding any other provision of law, no person shall be subject to any penalty for failing to comply with a collection of information if it does not display a currently valid OMB control number.
PLEASE DO NOT RETURN YOUR FORM TO THE ABOVE ADDRESS.

1. REPORT DATE *(DD-MM-YYYY)* 12 April 2014	2. REPORT TYPE Final Report	3. DATES COVERED *(From – To)* 2 April 2012 – 1 April 2014

4. TITLE AND SUBTITLE	5a. CONTRACT NUMBER
Global empirical model of the TEC response to geomagnetic activity and forcing from below	**FA8655-12-1-2057**
	5b. GRANT NUMBER
	Grant 12-2057
	5c. PROGRAM ELEMENT NUMBER
	61102F

6. AUTHOR(S)	5d. PROJECT NUMBER
Dora Pancheva Plamen Mukhtarov Borislav Andonov	
	5d. TASK NUMBER
	5e. WORK UNIT NUMBER

7. PERFORMING ORGANIZATION NAME(S) AND ADDRESS(ES) National Institute of Geophysics, Geodesy and Geography Bulgarian Academy of Sciences BL. 3 Acad. Georgi Bonchev Sofia 1000 BULGARIA	8. PERFORMING ORGANIZATION REPORT NUMBER N/A

9. SPONSORING/MONITORING AGENCY NAME(S) AND ADDRESS(ES) EOARD Unit 4515 APO AE 09421-4515	10. SPONSOR/MONITOR'S ACRONYM(S) AFRL/AFOSR/IOE (EOARD)
	11. SPONSOR/MONITOR'S REPORT NUMBER(S) **AFRL-AFOSR-UK-TR-2014-0025**

12. DISTRIBUTION/AVAILABILITY STATEMENT

Distribution A: Approved for public release; distribution is unlimited.

13. SUPPLEMENTARY NOTES

14. ABSTRACT

This report presents the final results of the project with the following main objectives:
a) Development of global empirical background TEC model
b) Statistical evaluation of the global background TEC model
c) Development of global empirical model of TEC response to geomagnetic activity
d) On-line implementation of both global empirical TEC models: background and TEC response to geomagnetic activity and creating of their mobile versions.
e) Development of a hybrid global TEC model - an attempt to mitigate the global background TEC model's error by using regularly arriving new CODE TEC data
f) Winter-time assessment of the global TEC dependence on the stratospheric temperature and solar radiation

15. SUBJECT TERMS

EOARD, ionoshere, total electron content, TEC

16. SECURITY CLASSIFICATION OF:			17. LIMITATION OF ABSTRACT	18, NUMBER OF PAGES	19a. NAME OF RESPONSIBLE PERSON Thomas Caudill
a. REPORT	**b. ABSTRACT**	**c. THIS PAGE**	SAR	59	
UNCLAS	UNCLAS	UNCLAS			**19b. TELEPHONE NUMBER** *(Include area code)* +44 (0)1895 616186

Standard Form 298 (Rev. 8/98)
Prescribed by ANSI Std. Z39-18

Project Title

Global empirical model of the TEC response to geomagnetic activity and forcing from below

Deliverable 002: Final Report
EOARD Contract No FA8655-12-1-2057

Authors

Dora Pancheva, Plamen Mukhtarov, and Borislav Andonov
(National Institute of Geophysics, Geodesy and Geography, Bulgarian Academy of Sciences)

April 2014

Table of Contents

List of Figures

Figure 13 Latitude-LT cross sections of the real (left column of plots) and model (right column of plots) *RMSE* for 15 January (upper row of plots), 15 March (second from above row of plots), 15 July (third from above row of plots) and 15 October (bottom row of plots) at high solar activity 2001.

Figure 14 The same as Figure 5 but at low solar activity 2008.

Figure 15 The same as Figure 5 but at middle solar activity 2004.

Figure 16 Two-dimensional (longitude-time lag) cross-correlation functions calculated between the rTEC and K_p-index for January at equator (upper most plot), $\pm 20^o$ (upper row of plots), $\pm 40^o$ (middle row of plots) and $\pm 70^o$ (bottom row of plots); the zero time lag is marked by tick black line.

Figure 17 Two-dimensional (LT-time lag) cross-correlation functions calculated between the rTEC and K_p-index for September at equator (upper most plot), $\pm 20^o$ (upper row of plots), $\pm 40^o$ (middle row of plots) and $\pm 70^o$ (bottom row of plots); the zero time lag is shown by tick black line.

Figure 18 Two-dimensional (modip latitude-time lag) cross-correlation functions calculated between the rTEC and K_p-index for months: January (upper row of plots), March (second row of plots), June (third row of plots) and September (bottom row of plots) and at 0^oE (left column of plots) and 270^oE (right column of plots); the zero time lag is shown by tick black line.

Figure 19 Comparison between the theoretical cross-correlation function (upper plot) calculated for T_1=12 h, T_2=32 h, α=1, β=-1 and for simplicity the variance is accepted to be 1, and the empirical cross-correlation function between the K_p-index and *rTEC* for August and at (40^oN, 0^oE) (bottom plot).

Figure 20 The empirical dependence between the K_p and rTEC calculated for different months and geographical points noted at the plots.

Figure 21a Temporal variability of the Kp-index during the geomagnetic storm in April 5-13, 2000.

Figure 21b Comparison between the model (right column of plots) and observed (left column of plots) rTEC longitude-hour cross-sections for the considered geomagnetic storm at different modip latitudes noted above the plots.

Figure 22a Temporal variability of the Kp-index during the geomagnetic storm in November 6-13, 2004.

Figure 22b Comparison between the model (right column of plots) and observed (left column of plots) rTEC longitude-hour cross-sections for the considered geomagnetic storm at different modip latitudes noted above the plots.

Figure 23 Modip latitude-month cross-section of the model *RMSE* calculated for the entire (January 1999 – December 2011) time interval.

Figure 24 Comparison between the model (right column of plot) and CODE TEC maps for November 8, 2004 geomagnetic storm at 00UT (upper row of plots), 06UT (second row of plots), 12UT (third row of plots) and 18UT (bottom row of plots). The modip latitude is also marked by white line.

Figure 25 The block chart of the global TEC model for short-time prediction.

Figure 26 Geomagnetic Kp-index forecast based on the MAK model.

Figure 27 (upper plot) The Kp-index for 29 Oct-01 Nov 2003; comparison between the rTEC (upper row) and TEC maps (bottom row) between the CODE data (left column) and model results (right column).

Figure 28 Global empirical TEC models based on the CODE TEC data

Figure 29 Temporal variability of the model residuals calculated for points with longitude of 00° and modip latitudes of 00° (upper plot), 40°N (left plot) and 40°S (right plot) for 00 LT.

Figure 30 Normalized autocorrelation functions calculated for equator (uppermost plot) and at modip latitudes of: 40°N (left upper plot); 40°S (right upper plot); 80°N (left bottom plot) and 80°S (right bottom plot).

Figure 31 Comparison between the observed TEC data (thin solid line), not corrected model TEC (thick solid line) and corrected model TEC (dashed line) at offsets of: 15 days (left upper plot), 30 days (right upper plot), 45 days (left bottom plot) and 60 days (right bottom plot) calculated for 30°N and 0°E at 12 UT.

Figure 32 Comparison between the *RMSE* of the not corrected background TEC model (thick solid line) and corrected global TEC model (thin solid line with symbols) calculated for different offsets for the period for time 2007-2012.

Figure 33 (left plot) Latitude structure of the cross-correlation functions between the ZM TEC and ZM temperature at latitude of 60°N and altitude of ~40 km; the same as the left plot but the cross-correlation is with the DW1 TEC.

Figure 34 **(a)** Daily values of F10.7 for the period of time 2005-2010; **(b)** Latitude structure of the cross-correlation functions of F10.7 with ZM TEC (left plot) and DW1 TEC (right plot).

Figure 35 (a) Modip latitude dependence of the regression coefficients which describe ZM TEC (left plot) and DW1 TEC (right plot); **(b)** Modip latitude dependence of the model RMSE (in TECU) calculated for ZM TEC (purple) and DW1 REC (magenta).

Figure 36 Modip latitude dependence of the standard deviations of ZM TEC (left plot) calculated from the CODE data (magenta), full model (green), solar part of the model (red) and temperature part of the model (blue); (right plot) the same as the upper plot but for the standard deviations of DW1 TEC.

Abstract

This report presents the final results of the project "Global empirical model of the TEC response to geomagnetic activity and forcing from below" (FA8655-12-1-2057) with the following main objectives:

a) Development of global empirical background TEC model

b) Statistical evaluation of the global background TEC model

c) Development of global empirical model of TEC response to geomagnetic activity

d) On-line implementation of both global empirical TEC models: background and TEC response to geomagnetic activity and creating of their mobile versions.

e) Development of a hybrid global TEC model - an attempt to mitigate the global background TEC model's error by using regularly arriving new CODE TEC data

f) Winter-time assessment of the global TEC dependence on the stratospheric temperature and solar radiation

Introduction

Description of the problem

The high sensitivity of the ionosphere to the external forcing related to changes in solar EUV and UV radiation and geomagnetic activity, and the continuous action of the lower atmospheric forcing, as the wave forcing particularly effective during low solar activity conditions, causes significant ionospheric variability on different time and spatial scales. To understand and forecast such variability is the main tasks of space weather research. Such task can be solved by building of ionospheric models which play an important role in specifying the ionospheric environment as realistically as possible. The total electron content (TEC) has received a great deal of attention recently, because it is a key parameter related to the phase delay effects on the signals of Global Navigation Satellite Systems (GNSS). The ionospheric effect is the largest error source in GNSS positioning, timing and navigation. The accuracy of the GNSS such as the Global Positioning System (GPS), the Russian GLONASS, the Chinese BeiDou and the European Galileo, is heavily affected by the ionosphere. The accurate TEC prediction, particularly during periods of solar disturbances, is a strong requirement for the reliable performance of many applications including HF communications, satellite positioning, navigation applications, detection and tracking of missiles and other targets. Most of the ionospheric error, or so called first-order range error, has been already eliminated by differential measurements in dual frequency systems like GPS, 1575.42 MHz at L1 and 1227.60 MHz at L2. However, ionosphere dual-frequency algorithms used for positioning applications remove only first-order range error but do not take into account its higher-order terms. Also, the ray paths and TEC are assumed to be the same for both frequencies which is away from the reality particularly considering the horizontal gradients of the ionosphere electron density. Additionally, there are still numerous single frequency applications which need additional information for mitigating the ionospheric propagation error. Such GNSS users can be provided by adequate ionospheric corrections obtained by an autonomous ionospheric TEC model (without any ionospheric measurements).

Different empirical TEC models, based on existing empirical models of the electron density distribution such as IRI or NeQuick or different TEC measurements, have been already built. They

however consider only the external forcing of the ionosphere, i.e. variable solar EUV and UV radiation and geomagnetic activity. Often, and especially recently when the level of solar activity is very low, quite large day-to-day changes of the ionosphere have been observed. With the recent accumulation of satellite measurements, attention is now being directed towards investigating the impact of the processes from below and particularly the wave forcing from the lower atmosphere. Various ionospheric observations have shown the development of longitudinal wave-like patterns (as wave number three (WN3), or wave number four (WN4) structures that revealed quite stable seasonal behavior. The evidence has emerged from different measurements and all of them unambiguously display manifestations of lower atmospheric dynamics on the upper atmosphere and ionosphere. Therefore, it is time a new type of global empirical TEC model to be built where both types of forcing, from above and from below, to be included.

Summary of the main results

In order to build a new type of global empirical TEC model, where the forcing from below is included as well, a serious knowledge on the coupling process of the atmosphere-ionosphere system is requited. The generation and propagation of atmospheric waves is a dominant aspect of the atmosphere and is a key component linking different regions. Recent studies based on the observations made by the Sounding of the Atmosphere using Broadband Emission Radiometry (SABER) and the TIMED Doppler Interferometer (TIDI) instruments on the Thermosphere-Ionosphere-Mesosphere-Energetics and Dynamics (TIMED) satellite have provided new insight into wave fields and revealed the global distribution and climatology of the most important wave components in temperature and neutral winds respectively. The research group from the NIGGG-BAS has serious contribution for clarifying the global distribution and temporal variability of the main atmospheric wave fields, as tides and planetary waves, which have impact on the ionosphere. Pancheva et al. (2009a, 2009b) created an advanced method for analysis of satellite measurements on the basis of which the authors have been able to study in detail the wave forcing of the ionosphere from lower stratosphere to lower thermosphere, i.e. up to the dynamo region where the waves directly or indirectly (by electrodynamics) can have impact on the ionosphere. By using this advanced approach the climatological features of the following atmospheric waves have been investigated: migrating diurnal tide (Mukhtarov et al., 2009), migrating semidiurnal tide (Pancheva et al., 2009c), nonmigrating tides (Pancheva et al., 2009d; 2010a) and different stationary and zonally propagating planetary waves (Pancheva et al., 2007, 2009b, 2010b; Mukhtarov et al., 2010a; Lu et al., 2012). Very recently the climatology of the migrating terdiurnal tide has been reported also (Pancheva et al., 2013). The detailed picture of the spatial structure and temporal variability of the atmospheric tides and planetary waves obtained from satellite measurements and summarized in the Springer book chapter by Pancheva and Mukhtarov (2011a) has already served as a benchmark and guide for numerical modeling studies aimed at better understanding the coupling processes by tidal and planetary wave patterns.

The next step in the atmosphere-ionosphere coupling studies is clarifying the ionospheric response to different tides and planetary waves. For this purpose the ionospheric measurements of the Constellation Observing System for Meteorology, Ionosphere, and Climate (COSMIC), as the COSMIC electron density profiles in the altitude range of 100-800 km, have been used. The crucial point in studying the ionospheric response to wave forcing from below is the application of one and the same data analysis method to both data sets, atmospheric (SABER/TIMED satellite data) and ionospheric (COSMIC electron density) data. By using two data sets Pancheva and Mukhtarov (2010) for the first time provided evidence showing that the ionospheric WN4 and WN3 are generated mainly by eastward propagating nonmigrating diurnal tides with wavenumbers 3 and 2 respectively. The spatial structures of the ionospheric response to some migrating and nonmigrating tides have been presented in Mukhtarov and Pancheva (2011) and Pancheva and Mukhtarov (2012a), while the ionospheric response to planetary waves is considered in Mukhtarov et al.

(2010b) and Pancheva and Mukhtarov (2012b). The detailed picture of the spatial structure and temporal variability of the ionospheric response to waves forced from below has been summarized in the Springer book chapter by Pancheva and Mukhtarov (2012c). The obtained main features of the ionospheric response to different tides forced from below have been supported by the first detailed comparison between simulated, by the whole atmospheric model called GAIA, and observed COSMIC global electron density responses (Pancheva et al., 2012). Recently a special attention has been paid to the vertical coupling during anomalous stratospheric events like sudden stratospheric warmings (SSW). Pancheva and Mukhtarov (2011b) by using atmospheric and ionospheric satellite measurements for the first time presented experimental evidence that the ionosphere regularly responds to almost all SSW stratospheric temperature pulses at high stratospheric latitudes. Later by combining the observations with simulations done by the GAIA model further insight on the ionospheric response to the SSW events has been obtained (Jin et al., 2013).

Besides knowledge on atmosphere-ionosphere coupling the NIGGG-BAS research group has serious experience in empirical modeling also. It participated in almost all COST actions devoted to the applied ionospheric research and specialized in empirical modeling of ionosphere and development of methods for nowcasting and forecasting ionospheric parameters of interest to radio communications and GNSS navigation. The single-station model approach for long-term prediction was developed quite long time ago by Pancheva and Mukhtarov (1996, 1998). The idea for describing the solar activity by two parameters, i.e. the level of solar activity and its tendency, was introduced for the first time by Pancheva and Mukhtarov (1996) in modeling the monthly median critical frequency of the ionospheric F-region, f_oF2, above Sofia and is used in the newly developed background TEC model (Section 1). A method for "weighted extrapolation" of past measurements of the f_oF2 has been developed by using the linear regression method, which coefficients were obtained from its autocorrelation function (Muhtarov and Kutiev, 1999). Based on this method, a series of single-station models for short-term forecasting (up to 3 days ahead) of f_oF2 have been developed. The basic model (Kutiev et al, 1999, Muhtarov et al, 2001) has been implemented in STIF software at Rutherford Appleton Laboratory, UK. Muhtarov et al, (2001) introduced a new term in the autoregressive formula for prediction of foF2, representing the changes of geomagnetic activity. This, so called geomagnetically-correlated autoregression method was implemented in the forecasting software of DIAS system (http://www.iono.noa.gr/DIAS). Important improvement of forecasting methodology was made by separation of the seasonal variations of foF2, represented by monthly medians, from the deviations presumably invoked by geomagnetic activity; this approach is applied in the created new global TEC model response to geomagnetic activity (Section 3). The relative deviations of f_oF2 (denoted as rf_oF2) from its median values were represented by analytical functions of the geomagnetic K_p-index. Another models, as the midlatitude model of f_oF2 (Kutiev and Muhtarov, 2001) and the global model of monthly average deviations as function of K_p (Kutiev and Muhtarov, 2003) have been developed in the framework of COST actions and reflected the European level of applied ionospheric research, which in many cases was leading in the global scale.

All above mentioned studies have been related mainly to the ionospheric parameters defined by ionosonde stations. Recently Andonov et al. (2011) have presented an empirical TEC model response to the geomagnetic activity for the American sector but particularly valid for low solar activity. It was based on the two-dimensional (2D) cross-correlation analysis which revealed both positive and negative phases of the response. The both phases of the ionospheric response have different duration and time delay with respect to the geomagnetic activity, season and geographical latitude. The same approach is applied and developed further in the created new global TEC model response to geomagnetic activity (Section 3).

Based on the above described knowledge and experience two global empirical TEC models have been built during the first year of the project. The first model is a background TEC model (Mukhtarov et al., 2013a) for describing the mean behavior of the ionosphere under both its

primary external driver, i.e. the direct photo-ionization by incident solar radiation, and regular wave particularly tidal forcing from the lower atmosphere. Moreover, we aim to make this model applicable under quiet geomagnetic conditions for long-term prediction of the average TEC variability. This model is statistically evaluated and even an error model is suggested (Mukhtarov et al., 2013b). The second model is a global empirical model of the TEC response to geomagnetic activity (Mukhtarov et al., 2013c) described by the Kp-index which is aimed at short-term prediction (a day ahead) of the TEC variability.

1. Development of empirical background TEC model

1.1 TEC Data Set

It is known that empirical models typically represent the gross features in the ionosphere quite well, but are limited to the way the model was built, the data that was used to construct it, and the conditions that were occurring while the data was taken. Recently, the GPS measurements obtained from the global and regional networks of International GNSS Service (IGS) ground receivers have become a major source of TEC data over large geographic areas. This system offers low cost information characterized by its accuracy, high temporal and spatial resolution, and availability. The present background TEC model is constructed on the base of vertical TEC maps generated by the CODE at Astronomical and Physical Institutes of the University of Bern (http://cmslive3.unibe.ch/unibe/philnat/aiub/content/e15/e59/e126/e440/e447/index_eng.html). We particularly note that TEC everywhere means vertical TEC. The data for full 13 years, 1 January 1999 – 31 December 2011, provided from the CODE FTP directory: ftp://ftp.unibe.ch/aiub/CODE/ are used. The two-hourly sets are derived from GPS data of the global IGS network of about 200 stations. The GIM/CODE is regarded as one of the most precise TEC maps generated from GNSS observations. The used global IGS TEC data have a time resolution of 2 h and a grid spacing of 5° x 2.5° in longitude and latitude, respectively with errors of several TEC Units (TECU, 1 TECU = 10^{16} el/m^2).

The original global TEC data were arrayed in terms of the coordinate system of geographical latitude (from -87.5^{o} to 87.5^{o} at each 2.5^{o}) and longitude (from -180° to 180° at each 5°). It is known however that the neutral wind and electric field effects on the ionosphere are dependent on the geomagnetic field configuration as the electrons are constrained to the magnetic field lines. That is why the distribution of the ionospheric parameters, including TEC as well, is usually presented in geomagnetic latitude instead of geographic one. We use the modified dip latitude (modip), introduced by *Rawer* (1963). The modified dip (modip) latitude which is adapted to the real magnetic field, e.g., to the magnetic inclination (dip), is defined by: $\tan \mu = I \left/ \sqrt{\cos\Phi} \right.$, where μ is the modip latitude, I is the true magnetic dip (usually at a height of 350 km), and Φ is the geographic latitude. Modip equator is the locus of points where the magnetic dip (or inclination) is 0. In the equatorial zone, the lines of constant modip are practically identical to those of the magnetic inclination but as latitude increases they deviate and come nearer to those of constant geographical latitude. The poles are identical to the geographic ones. For the purpose of this study the global TEC data were re-arrayed in terms of the coordinate system of modip latitude, from -80° to 80° at each 5°, and geographic longitude, from -180° to 180° at each 15°. The TEC data falling into the area 5° (modip latitude) x 15° (longitude) were averaged.

Usually the background ionospheric models are formulated in terms of monthly median parameters because such parameters are not affected by large but short-time lasting disturbances generated by strong geomagnetic storms. In the present study we use sliding medians defined by a 31-day moving window and the median value is assigned to the central day of the window, i.e. to the 16th day of the window. The sliding medians are calculated independently for each point of the grid (as it is done with single station data). In this way the daily TEC time series are obtained at each modip

latitude, longitude and UT. It is worth noting that the perturbations from geomagnetic origin or related to solar rotation period are filtered from these time series.

1.2 Basic Approach of the Model Construction

The basic idea of each global empirical background TEC model, used for long-term prediction, is to define a set of empirical functions which describes the most probable TEC values at given solar activity, day of the year (DOY), geographic location and UT. In the present study we accepted: (i) longitude and UT as independent variable quantities; the conversion into LT is a simple procedure, and (ii) at each modip latitude a separate model is constructed; the values of the model TEC which do not belong to the 5° modip grid are obtained by an interpolation procedure that will be described later. The latter is done because if a latitudinal approximation is used first the number of model constants will increase and second an additional error will be introduced in the model.

According to the above mentioned approach the TEC values at each modip latitude circle can be presented as a function of:

TEC (solar activity, DOY, longitude, UT) (1)

Ideally the solar activity should be described by an index that tracks the solar cycle changes in the EUV wavelength range, since this part of the solar spectrum affects the ionosphere. However, such indices cannot be observed at the ground and are only available for relatively short time periods covered by satellite UV instruments. Thus, most ionospheric modelers use the sunspot number (number of dark spots on the solar disc) and the solar radio flux at 10.7 cm wavelength (F10.7) as solar indices, since both can be observed from the ground, long data records exist and they can be predicted. These indices together with their 6-month predictions are regularly published by NOAA Space Weather Prediction Center (http://www.swpc.noaa.gov/index.html). In the present study F10.7 is used as a proxy for the solar activity. It is known however that the ionosphere behaves differently at the rising and declining phase of the solar cycle at one and the same F10.7. To include this ionospheric feature in the model an additional parameter K_F is used which describes the linear rate of change of F10.7. As has been already mentioned this idea was introduced for the first time by Pancheva and Mukhtarov (1996). Figure 1 shows the temporal variability of the used two solar parameters *F10.7* in solar flux units (10^{-22}W m^{-2} Hz^{-1}) and K_F for the considered 13 years (1999-2011).
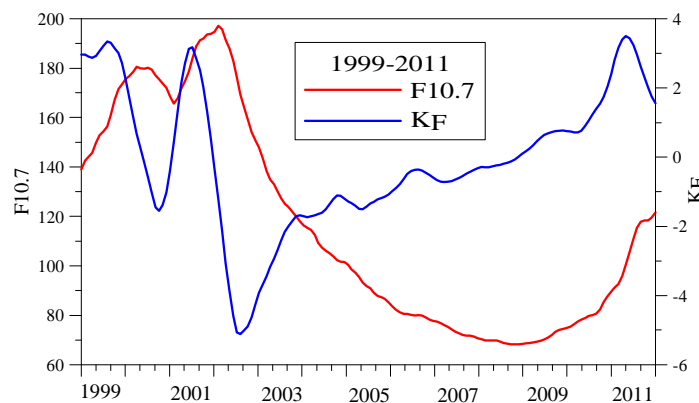
Figure 1 Monthly mean solar radio flux *F10.7* (red line) and its linear rate of change K_F (blue line) obtained by a sliding 11-month time derivatives of *F10.7*.

The seasonal variability of the vertical TEC is characterized mainly by annual and semiannual components whose amplitudes and phases depend on solar activity, geographic/geomagnetic location and UT. The seasonal components with periods shorter than 6 months have also some contribution but they are weaker than annual and semiannual components. In general, the

semiannual behavior is characterized by a larger peak in March-April than that in September-October; the difference is particularly strong (up to 40%) during high solar activity.

In all existing so far empirical models the diurnal TEC variability is described only by the migrating "tidal" components, i.e. components with periods 24, 12, 8 hours, etc., which propagate with the apparent motion of the Sun to a ground-based observer. In this way it is assumed that the diurnal variability of the ionosphere is forced mainly by the diurnal cycle of the photo-ionization. However, only within the past 5-6 years has the realization emerged that "troposphere weather" contributes significantly to the "space weather" of the thermosphere, especially during solar minimum conditions. Much of the attendant variability is attributable to upward-propagating solar tides excited by latent heating due to deep tropical convection, and solar radiation absorption primarily by water vapor and ozone in the troposphere and stratosphere, respectively. Recent studies based on the modern satellite-board data (electron densities from COSMIC and temperatures from SABER/TIMED) revealed the importance of the ionospheric forcing from below (see previous section). There is another reason also for including the nonmigrating tidal variability in the TEC model. It is related to the offset between the geographic and modip latitudes. The dynamics of the thermosphere (defined mainly by prevailing winds and atmospheric tides) is defined in a geographic frame but its effect on the ionosphere depends on the geomagnetic field configuration. The photo-ionization depends also on geographic frame (solar zenith angle) however as the electrons are constrained to the magnetic field lines its effect is geomagnetic field dependent. The offset between geographic and geomagnetic frames generate additional tidal ionospheric responses which can originally not be present in the forcing from below. These additional ionospheric tides are much weaker than the real ones (on the average ~3-10%) but they have some contribution to the diurnal variability of the ionosphere particularly in shaping some quasi-stationary structures.

As the time scales of the solar cycle, seasonal and diurnal influences on the TEC variability are very different (they differ at least an order of magnitude) then the shorter-period TEC variabilities are usually modulated by the longer ones. In this case the TEC spatial-temporal variability can be represented as a multiplication of three separable functions, i.e. (1) can be expressed in the following way:

$$TEC(F, K_F, DOY, lon, UT) = \Phi_1(F, K_F)\Phi_2(DOY)\Phi_3(lon, UT) \tag{2}$$

The above right hand side unknown functions Φ_k *(k=1,2,3)* can be represented by their series expansions; Φ_1 can be expanded in Taylor series, while Φ_2 *and* Φ_3, which are periodic functions with periods respectively a year and a solar day, can be expanded in Fourier series. Therefore, the background TEC model can be described by the following functions:

$$TEC(F, K_F, DOY, lon, UT) = \left(\alpha_0 + \alpha_1 F + \alpha_2 K_F + \alpha_3 F K_F + \alpha_4 F^2 + \alpha_5 K_F^2\right) \times$$
$$\left(\beta_0 + \sum_{i=1}^{4} \beta_i \cos\left(i\frac{2\pi}{365}day - \varphi_i\right)\right) \times \tag{3}$$
$$\left(\gamma_0 + \sum_{i=1}^{4}\sum_{s=-4}^{4} \gamma_{is} \cos\left(i\frac{2\pi}{24}UT - s\frac{2\pi}{360}lon - \psi_{is}\right) + \sum_{s=1}^{4} \delta_s \cos\left(s\frac{2\pi}{360}lon - \zeta_{is}\right)\right)$$

The expression in the first right hand bracket, i.e. the Taylor series expansion up to degree of 2, represents the solar activity term which modulates the seasonal and diurnal behavior of the ionosphere. The seasonal term (expression in the second right hand bracket) includes 4 subharmonics of the year, i.e. annual, semiannual, 4- and 3-month components; it modulates the diurnal behavior of the ionosphere. The diurnal variability of the TEC model (expression in the third right hand bracket) is composed by three parts: mean TEC (γ_0), a part describing migrating and nonmigrating tides and a part representing the effect of the stationary planetary waves (SPWs). The contribution of the migrating and nonmigrating tides is presented by 2D (longitude-time) sine

functions with zonal wavenumbers up to 4 and 4 subharmonics of the solar day (24-, 12-, 8- and 6-hour components). The last part, describing the contribution of the SPWs, includes waves with zonal wavenumbers up to 4. The presence of these wave structures in the ionosphere can be related to a few reasons: (i) offset between geographic and modip frames; (ii) can be generated by coupling processes between migrating and nonmigrating tides with one and the same periods, and (iii) some effect of the SPW1 temperature field in the lower thermosphere on the ionosphere, particularly at middle-high and high latitude ionosphere; *Mukhtarov et al.* (2010a) found strong evidence indicating that the auroral heating is a main origin of the lower thermospheric SPW1 structure.

The background TEC model described by (3) contains 4374 constants and they are determined by least squares fitting techniques. The numbers of the included components in the above described Taylor and Fourier expansion series are defined experimentally. We accepted only the above mentioned solar, seasonal and diurnal components because the addition of more components does not improve the model error.
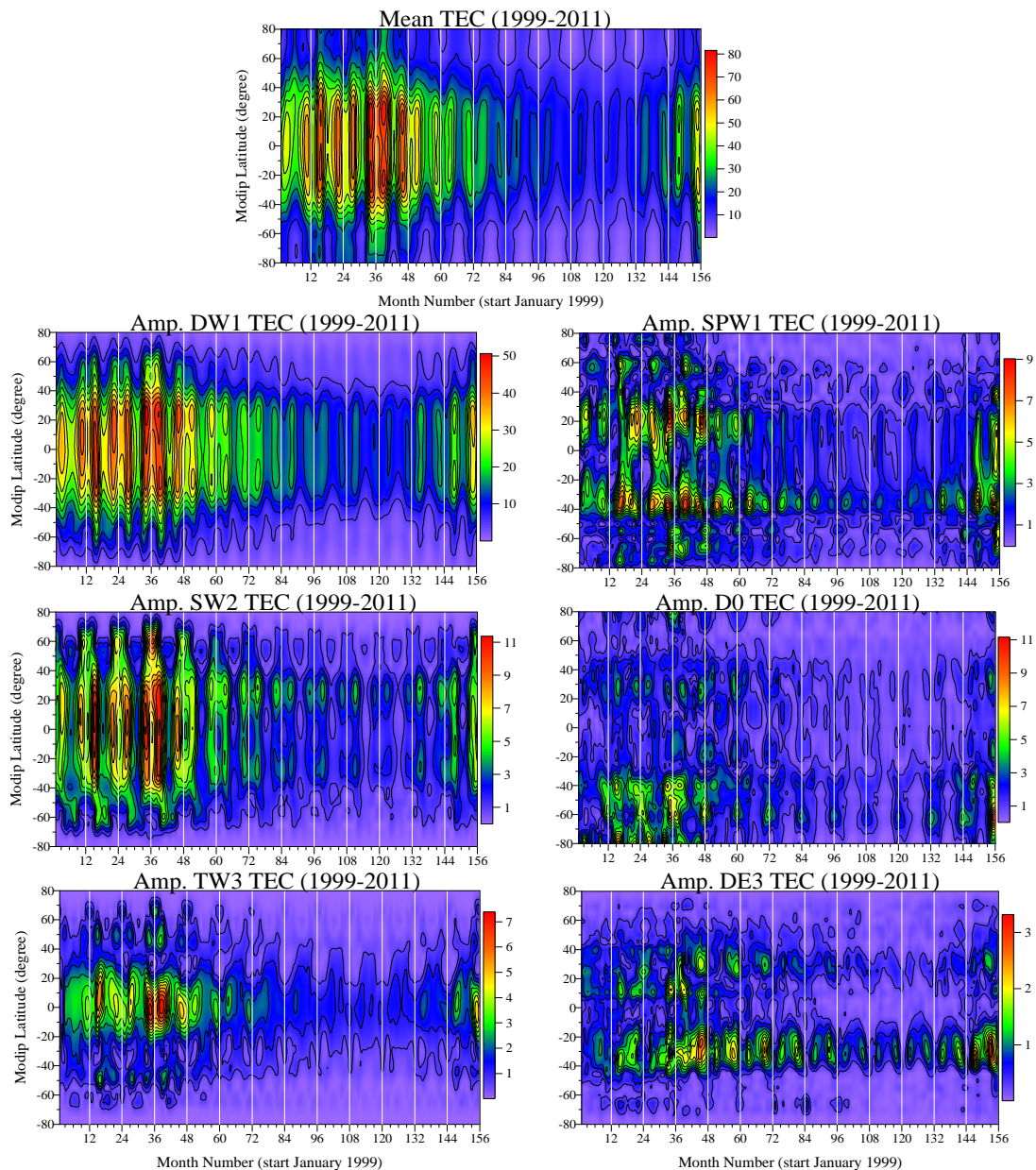
Figure 2 Latitude-time cross-sections of the following TEC components: (i) zonal and time mean TEC (upper most plot); (ii) left column of plots shows the amplitudes of migrating diurnal (DW1, upper plot), semidiurnal (SW2, middle plot) and terdiurnal (TW3, bottom plot) tides, and (iii) right column of plots shows the amplitudes of SPW1 (upper plot), nonmigrating zonally symmetric diurnal tide (D0, middle plot) and nonmigrating eastward propagating tide with zonal wavenumber 3 (DE3, bottom plot). The considered years from 1999 to 2011 are separated by thin white lines.

Figure 2 presents examples of solar cycle and seasonal modulations of some diurnal components included in the TEC model. For this purpose the TEC data are decomposed to mean TEC, migrating and nonmigrating tides, and SPWs (i.e. expressions in the third right hand bracket of (3)) by using a 31-day window. Then the 31-day window is moved forward through the time series with steps of 1 day in order to obtain the daily values of the wave characteristics for period of time 1 January 1999-31 December 2011. The monthly mean wave characteristics, shown in Figure 2, are obtained by vector averaging for each calendar month. The uppermost plot shows the latitude-time cross-section of the zonal and time mean of the TEC (first term, γ_0, in the third bracket); the considered years from 1999 to 2011 are separated by thin white lines. This diurnal TEC component follows strictly the solar activity, even the two maxima, a main maximum in 2002 (~80 TECU) and a secondary one in 2000 (~75 TECU), can be clearly distinguished. The semiannual variability is a dominant component of the seasonal behavior; on the average the vernal equinox maxima are stronger than the autumnal ones. The left column of plots present the latitude-time cross-sections of the first three migrating tides, 24-h (DW1, upper plot), 12-h (SW2, middle plot) and 8-h (TW3, bottom plot). The DW1 component is the strongest tidal component (maximum amplitude reaches ~50 TECU) and is shaped mainly by the diurnal variability of the photo-ionization. The SW2 component is significantly weaker than the DW1 one (maximum amplitude reaches ~11 TECU) and as it has been already mentioned is formed mainly by the SW2 tide forced from the lower atmosphere (Pancheva and Mukhtarov, 2012a). A clear evidence for the dominant role of the lower atmospheric SW2 tide on the TEC SW2 variability is the existence of the local winter maxima at modip latitude around $\pm 60^{\circ}$. The solar cycle and seasonal (mainly semiannual) modulations can be seen well for these diurnal components as well. While at high solar activity the separation at both sides of the equator can be well seen for the mean (γ_0) and DW1 components for the SW2 component such separation is evident better at low solar activity; at high solar activity the SW2 amplifies predominantly over the equator. The amplifications of the mean TEC, tidal DW1 and SW2 amplitudes around $\pm (20-30^{\circ})$ modip is related to the equatorial ionization anomaly (EIA) observed mainly during the daytime. Figure 2 shows that the solar activity affects not only the amplitude of the TEC equatorial anomaly but also the location of the crests; at high solar activity they are located close to $\pm 30^{\circ}$ while at low solar activity the crests move close to the equator, around $\pm 20^{\circ}$. The solar cycle and seasonal modulations are seen also on the third migrating component, TW3. The latitude structure of this diurnal component shows a main amplification over the equator and secondary ones around $\pm 50^{\circ}$ and $\pm 65^{\circ}$; the latter are particularly well seen during high solar activity.

The right column of plots present the latitude-time cross-sections of the amplitudes of the SPW1 (upper plot), nonmigrating zonally symmetric diurnal (D0, middle plot) and nonmigrating eastward propagating diurnal tide with zonal wavenumber 3 (DE3, bottom plot). All these diurnal components demonstrate regular solar cycle and seasonal variability. Their amplitudes are weaker than the DW1 tide but are comparable with those of the SW2 and TW3 tides. The D0 is the strongest nonmigrating component with maximum amplitude of ~11 TECU (the same as that of SW2). It amplifies mainly in the Southern Hemisphere (SH) at high latitudes; similar distributions have also the other zonally symmetric tidal components but their amplitudes are weaker than that of D0 (not shown here). All zonally symmetric tidal components show amplifications like stripes between -40° and -70° modip latitude that can be distinguished even at low solar activity. Similar amplifications are evident for SPWs components, but they are present at both hemispheres. Later it will be shown that just these zonally symmetric nonmigrating and SPW components have predominant contribution to the so called Weddell Sea Anomaly (WSA). This anomaly appears as an evening enhancement in electron density, i.e. larger nighttime electron density than during the day, in the region near the Weddell Sea, Antarctica peninsula. The WSA occurs mostly in southern summer and can extend from South America and Antarctica to the central Pacific. The TEC DE3 component (bottom plot), similarly to the other diurnal components, is strongly modulated by the solar cycle and shows clear semiannual variability. In this case however the autumnal maxima are

stronger than the vernal ones. This is due to fact that the neutral DE3 tide forced from below is the main driver of the ionospheric DE3 variability (Pancheva and Mukhtarov, 2010); the authors presented unambiguous evidence that the ionospheric DE3 variability is forced from below. We pay special attention to the TEC DE3 nonmigrating diurnal component as it has the main contribution to the so called WN4 longitude structure observed in many ionospheric parameters particularly during low solar activity. Later we will demonstrate the ability of this background model to reproduce the WN4 and WN3 ionospheric structures.

1.3 Model Results

The basic aim of each global TEC model used for long-term prediction is to construct the global distribution of the TEC, i.e. to obtain global TEC maps, at given solar activity, day of the year and UT. The TEC maps are constructed by interpolation of the TEC values from the used grid with a 5° step in modip latitude and 15° in longitude. The interpolation between obtained from the model TEC values is done by using Inverse Distance Method (*Shepard, D.*, 1968). Then the modip frame is converted to geographical one. The TEC values assigned to both poles are found by interpolation between the known from the model points which have the highest northern and southern latitudes. The model maps are arrayed in terms of the coordinate system of geographical latitude from -90° to 90° at each 5° and longitude from -180° to 180° at each 5°.

First we will show how the background TEC model describes the WSA. The zone of anomalous diurnal variations in foF2, which is characterized by an excess of nighttime foF2 values over daytime ones, occupies the longitudes of 0°-180°W and the latitudes of 40°-80°S as the effect is maximal (up to ~5 MHz for the critical frequency of the F-region, foF_2) at longitudes of 40°-105°W and latitudes of 60°-70°S. Figure 3 presents the global map in geographical coordinate system calculated from the empirical background TEC model (upper plot) and compared with the CODE TEC map (bottom plot) at 08UT for 12 December 2012. The stripe TEC amplification in the Western Hemisphere at latitudes of ~50-80°S, i.e. the WSA, can be clearly distinguished at both model and CODE TEC maps; the maximal effect at both maps is near 70°S and longitudes of ~0-100°W. The presence of the WSA is a reason for appearing of an additional to the equatorial anomaly TEC amplification around 30-40°S and at the most Western Hemisphere; this feature is also well reproduced by the model. The model TEC map describes well also the hemispheric asymmetry of the equatorial anomaly revealing that the summer crest is stronger than the winter one.
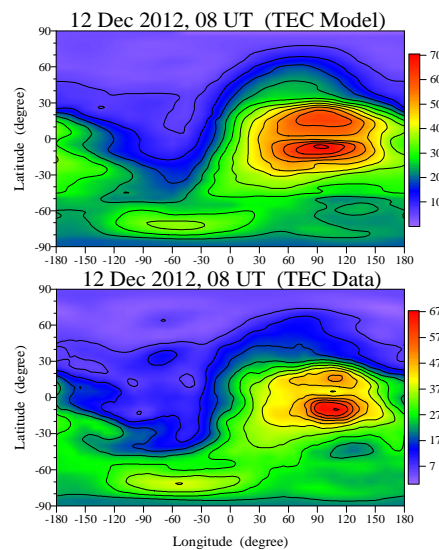
Figure 3 Global map in geographical frame calculated from the empirical background TEC model (upper plot) compared with the CODE TEC map (bottom plot) at 08 UT for 12 December 2012.

To demonstrate how the model reproduces some longitude wave-like structures we re-arrayed the model and CODE TEC data sets in local time (LT). It has been already mentioned that usually the ionospheric wave-like longitude structures are observed during low solar activity as the WN4 is

seen in August-October while the WN3 in December-January. Figure 4 shows the comparison between the global TEC model maps in modip latitude (upper row of plots) and CODE TEC maps (bottom row of plots) which represent the ionospheric WN4 (left column of plots) and WN3 (right column of plots) structures. The example for the WN4 structure is for October 2008 at 23LT, i.e. night-time, and that is why there is no the splitting of the irregularities at both sides of the equator. Four peaks around longitudes: -150°, -60°, 30° and 120° can be clearly distinguished at both model and CODE TEC maps. There is not only qualitative but also quantitative similarity between the model and observations. The example for the WN3 structure is for January 2008 at 14LT, i.e. daytime, when the equatorial anomaly is present. The splitting of the irregularities at both sides of the equator is seen at both model and CODE TEC maps. However, the WN3 structure is well developed and significantly stronger in SH. This hemispheric asymmetry is due to the asymmetry of the ionospheric DE2 variability, reported by Mukhtarov and Pancheva (2011), which is the main contributor of the WN3 structure. The three peaks particularly in the SH are located at longitudes of -150°, 0° and 120°. They are not exactly equidistant most probably because the contribution of other nonmigrating tides, as DW4 and SE1, and SPW3 (Pancheva and Mukhtarov, 2012a, 2012c). There are some signatures for the first and third peaks at NH evident at both model and CODE TEC maps.
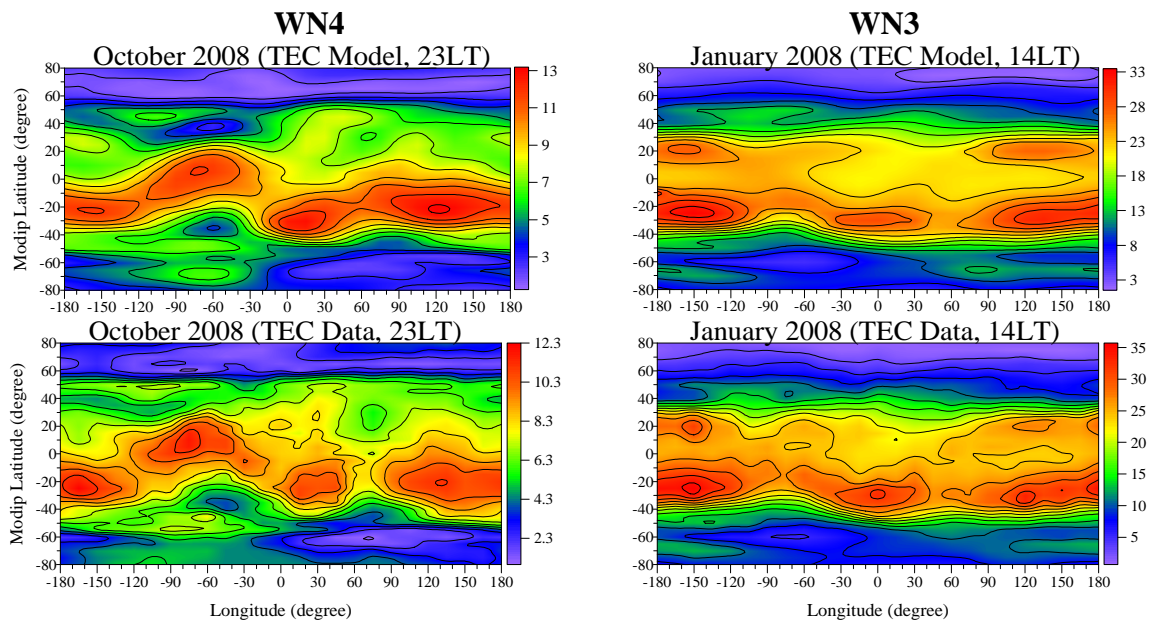
Figure 4 Comparison between the global TEC model maps in modip latitude (upper row of plots) and CODE TEC maps (bottom row of plots) which shows the ionospheric WN4 (left column of plots, at 23 LT for 15 October 2008) and WN3 (right column of plots, at 14 LT for 15 January 2008) structures.

The ability of the background TEC model to reproduce the temporal-spatial feature of the input CODE TEC data will be displayed by a comparison between the model and CODE TEC maps for different solar activity, seasons and UT. While Figure 5a shows the global maps in geographical coordinate system calculated from the empirical background TEC model (left column of plots) which are compared with the CODE TEC maps (right column of plots) at 12UT for 15 January 2001 (upper row of plots) and 15 March 2001 (bottom row of plots) during high solar activity 2001 Figure 4b shows the same but during low solar activity 2008. The modip latitude is also marked at the plots by white line as the low-latitude plasma bulk follows the modip frame. At both solar cycle conditions it is seen that the model maps reproduce very well the main features of the CODE TEC maps; some quantitative difference is evident only at winter model map where the equatorial anomaly is slightly weaker than that at the CODE TEC map (Figure 5a, upper row of plots). The hemispheric asymmetry of the equatorial anomaly, generated mainly by the thermospheric transequatorial neutral winds blowing from the summer to winter hemisphere, is evident well at both model and CODE maps but only at low solar activity (Figure 5b, upper row of plots). The

hemispheric symmetry of the equatorial anomaly during vernal equinox is also well evident at both model and CODE maps during high and low solar activity (Figures 5a and 5b, bottom rows of plots).
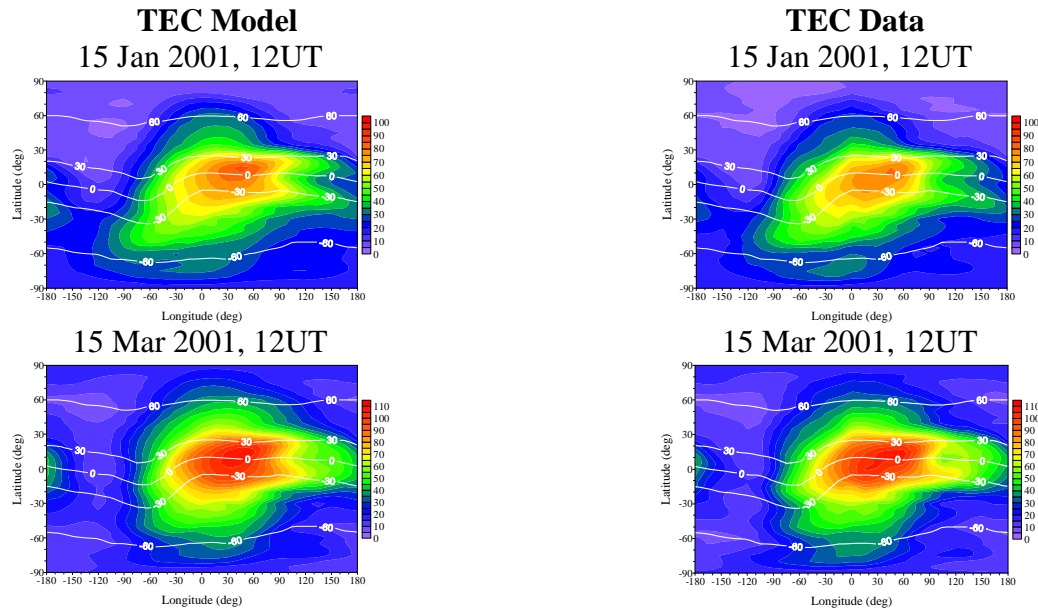
Figure 5a Global maps in geographical frame calculated from the empirical background TEC model (left column of plots) which are compared with the CODE TEC maps (right column of plots) at 12 UT for 15 January 2001 (upper row of plots) and 15 March 2001 (bottom row of plots) during high solar activity 2001. The modip latitude is also marked by white line.
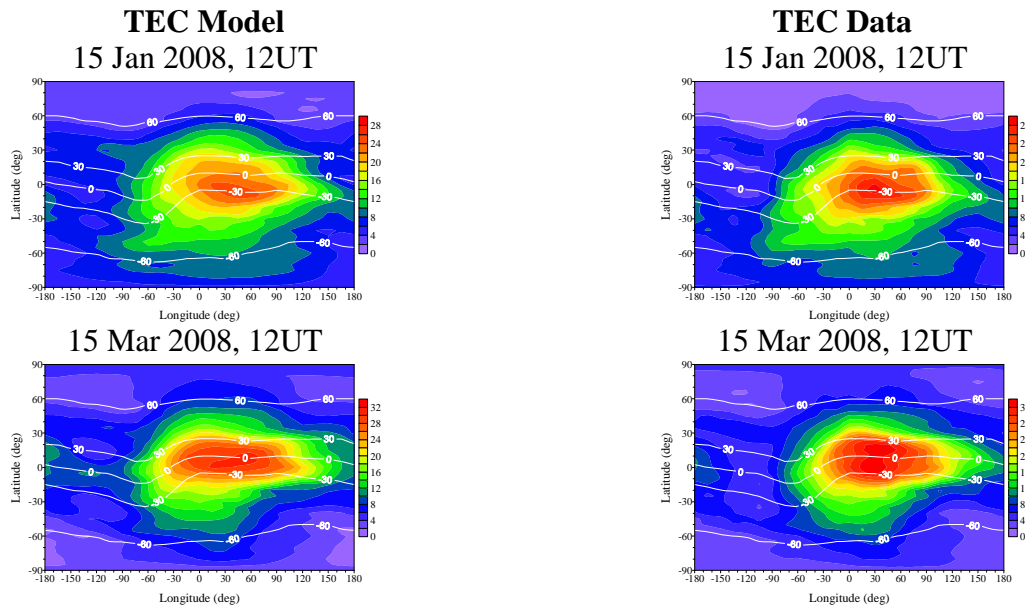
Figure 5b The same as in Figure 5a, but during low solar activity 2008.

Figure 6a presents the global maps from the background TEC model (left column of plots) compared with the CODE TEC maps (right column of plots) at 12UT for 15 July 2001 (upper row of plots) and 15 October 2001 (bottom row of plots) during high solar activity 2001while Figure 6b shows the same but for low solar activity 2008. Again the degree of similarity between model and CODE TEC maps is very high. Some undervalue of the model TEC is seen in July at most northern latitudes at both high and low solar activity (Figures 6a and 6b, upper row of plots). The model however reproduces very well the four TEC amplifications seen between ~50°N and ~40°S at the most western longitudes and two TEC amplifications at most eastern longitudes in July 2008

(Figure 6b, upper row of plots). It is worth noting that both model and CODE maps show the following features: (i) do not display hemispheric asymmetry of the equatorial anomaly during July at both solar activity conditions, (ii) the January TEC is larger than that in July at high and low solar activity (so called winter anomaly), and (ii) while the March TEC is higher than the October one during low solar activity the opposite feature is evident during high solar activity. We remind also that all the above mentioned features are seen at 12UT.
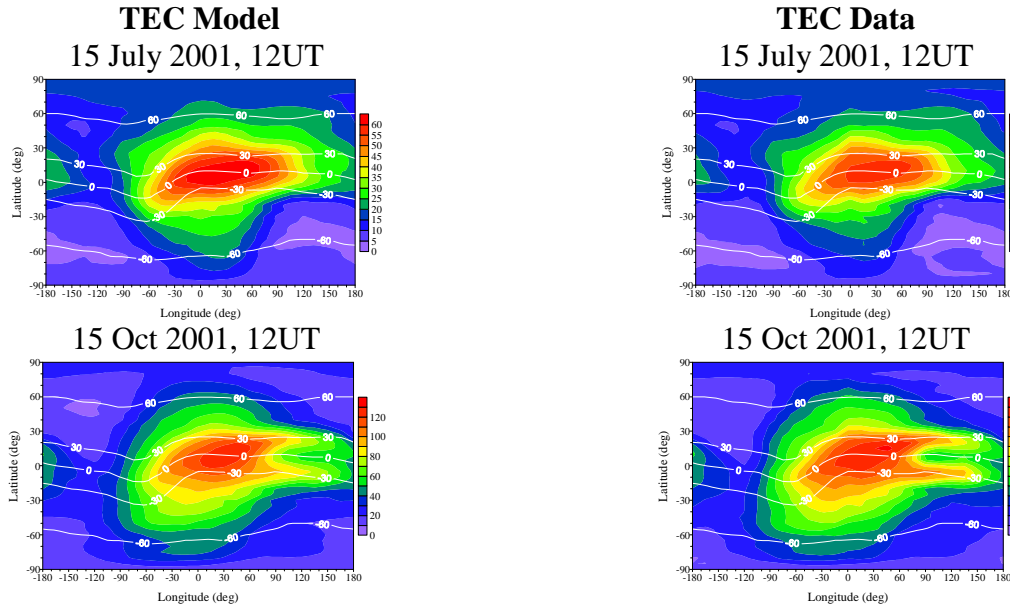

Figure 6a Global maps in geographical frame calculated from the empirical background TEC model (left column of plots) which are compared with the CODE TEC maps (right column of plots) at 12 UT for 15 July 2001 (upper row of plots) and 15 October 2001 (bottom row of plots) during high solar activity 2001. The modip latitude is also marked by white line.
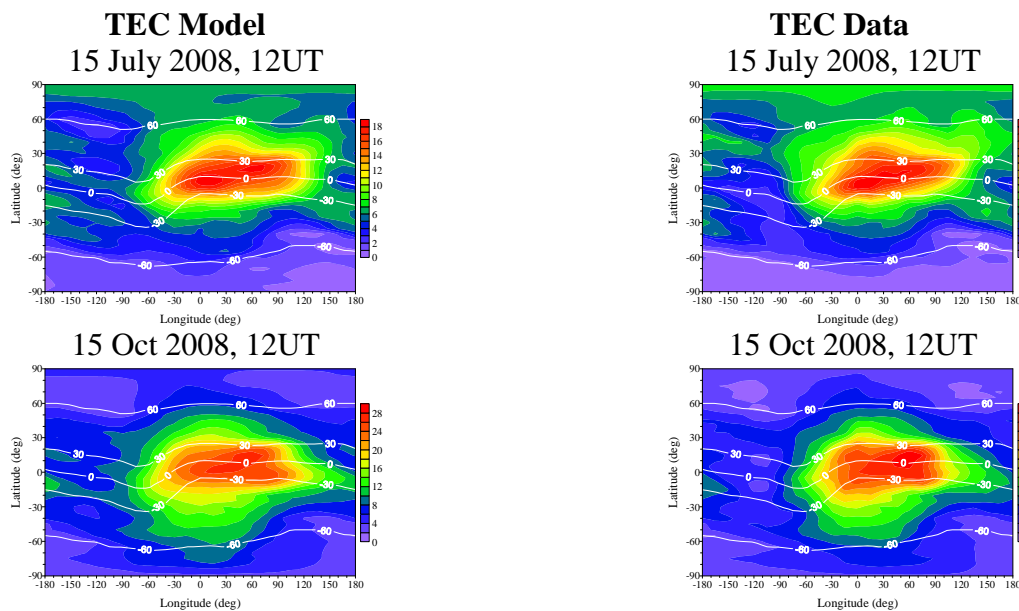

Figure 6b The same as in Figure 5a, but during low solar activity 2008.

The comparisons for the middle solar activity 2004 are presented in Figures 7a and 7b; in this case only maps for July at different UT are shown in order to trace out better the diurnal variability of the low latitude plasma bulk. Figure 7a shows global maps from the background TEC model (left column of plots) which are compared with the CODE TEC maps (right column of plots) at 00UT

(upper row of plots) and 06UT (bottom row of plots) for 15 July 2004 while Figure 7b presents the same but at 12UT (upper row of plots) and at 18UT (bottom row of plots). Again the comparison shows high degree of similarity; even some details in the spatial TEC distribution are well reproduced (see, for example, Figure 7a).
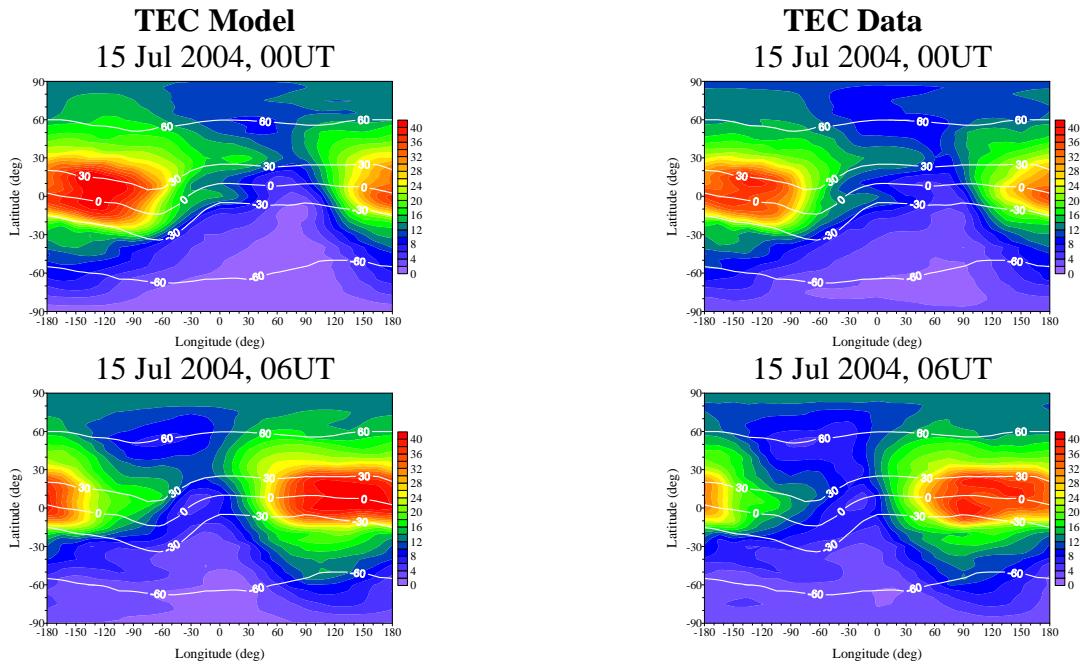
Figure 7a Global maps in geographical frame calculated from the empirical background TEC model (left column of plots) which are compared with the CODE TEC maps (right column of plots) at 00 UT (upper row of plots) and 06 UT (bottom row of plots) for 15 July 2004 during middle solar activity (2004). The modip latitude is also marked by white line.
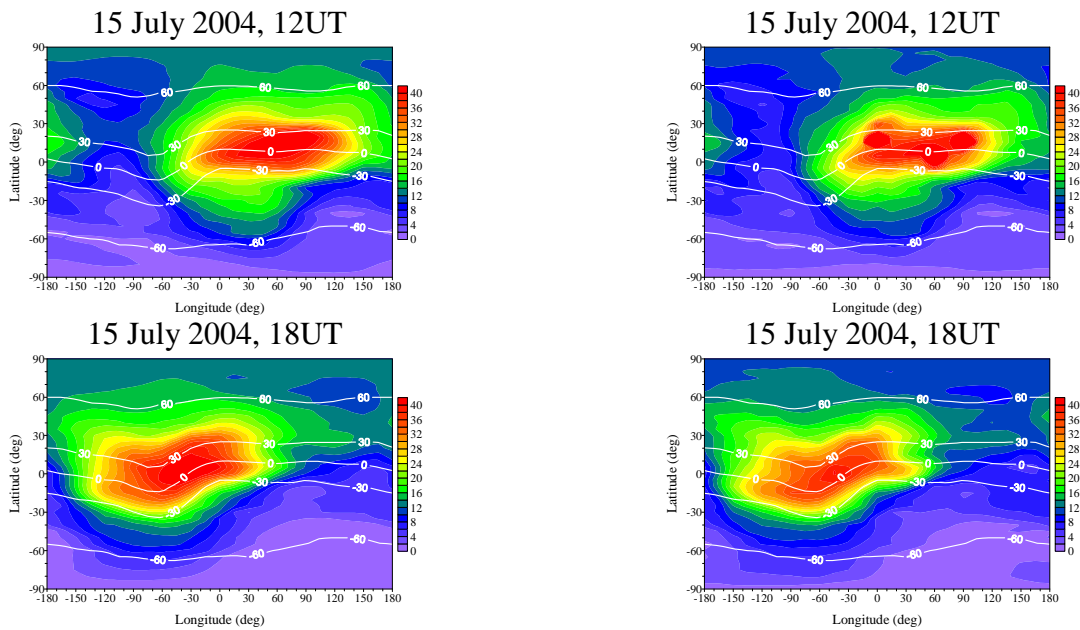
Figure 7b The same as in Figure 7a, but at 12 UT (upper row of plots) and 18 UT (bottom row of plots).

The above shown comparisons indicate that the empirical background TEC model can reproduce very well the main spatial-temporal variability of the CODE TEC maps. Each empirical model needs to be statistically evaluated. A detailed description of the model error will be done in the next

section. Here however only the main statistics based on the entire data set will be presented. It has been accepted that the mean (systematic) error (*ME*), root mean squares error (*RMSE*) and the standard deviation error (*STDE*) are the main error characteristics of each model. They are defined as:

$$ME = \frac{1}{N} \sum_{i=1}^{N} \left(TEC_{\text{mod}} - TEC_{obs} \right)$$

$$RMSE = \sqrt{\frac{1}{N} \sum_{i=1}^{N} \left(TEC_{\text{mod}} - TEC_{obs} \right)^2} \tag{4}$$

$$STDE = \sqrt{RMSE^2 - ME^2}$$

The application of (4) to all data for the considered period of time (1 January 1999-31 December 2011) gives the following errors: *ME*=0.003 TECU, i.e. the model has practically zero systematic error. In this case *RMSE=STDE*=3.387 TECU. In order to have an idea if such errors are high or low we compare this model with the similar to some extend new global TEC model built recently by Jakowski et al. (2011) and called NTCM-GL model. The statistical assessments of the NTCM-GL model are: *ME*=-0.3 TECU and *RMSE*=7.5 TECU. Hence, the errors of the present background TEC model are significantly smaller than those of the NTCM-GL model. We have to note that nevertheless that both models are climatological, i.e. they describe the average behavior under quiet geomagnetic conditions, the TEC model constructed by Jakowski et al. (2011) needs only 12 coefficients and a few empirically fixed parameters for describing a broad spectrum of TEC variation at all levels of solar activity. We however do not consider the large number of coefficients in the present background TEC model, 4374, as its weak point. They are calculated only once and are fixed later at the model applications.

1.4 Concluding comments and on-line implementation of the background TEC model

A global background TEC model is built on the basis of full 13 years (1999-2011) of CODE TEC data (Mukhtarov et al., 2013a). The model describes the climatological, i.e. under quiet geomagnetic conditions, behaviour of the ionosphere and can be used for long-term prediction. For this purpose at given day of the year, geographic location and UT the model needs as input parameters only the predicted level of solar activity (F10.7 is used here as a proxy for solar activity). The model maps are arrayed in terms of the coordinate system of geographical latitude from -90° to 90° at each 5° and longitude from -180° to 180° at each 5°.

The model describes very well such structures as the WSA (Figure 3) and the well-known WN4 and WN3 longitude structures (Figure 4). This was possible mainly because of the nonmigrating tides and SPW inclusion in describing the diurnal variability of the TEC. The presented comparison between the model and CODE TEC maps at different solar activities and seasons (Figures 5, 6 and 7) also demonstrated high degree of similarity. The zero systematic error and its low *RMSE* (3.387 TECU) provides the model significant advantage over the other similar models.

The present background model can be used for both science and applications. In science the model can be utilized as a background condition on the basis of which the perturbations can be estimated. It is particularly useful for investigating the geomagnetic perturbations, or ionospheric disturbances related to the sudden stratospheric warmings, by incoherent scatter radars where the measurements are available only for several days; in this case the background condition described by the monthly median TEC values cannot be determined. This model can be useful for numerous single frequency GPS applications which need additional information for mitigating the ionospheric propagation

error. Such GNSS users can be provided by adequate ionospheric corrections obtained by this autonomous ionospheric TEC model.

This model will be used for long-term prediction of the TEC. The online software has been already implemented on the website (http://www.geophys.bas.bg/tec/page/tec_index_en.htm), but it is still in testing mode. Figure 8 shows its block-chart. It will be officially implemented at the institute website when the paper Mukhtarov et al. (2013a) is published (it has been accepted for publication in *J. Geophys. Res. – Space Physics*).
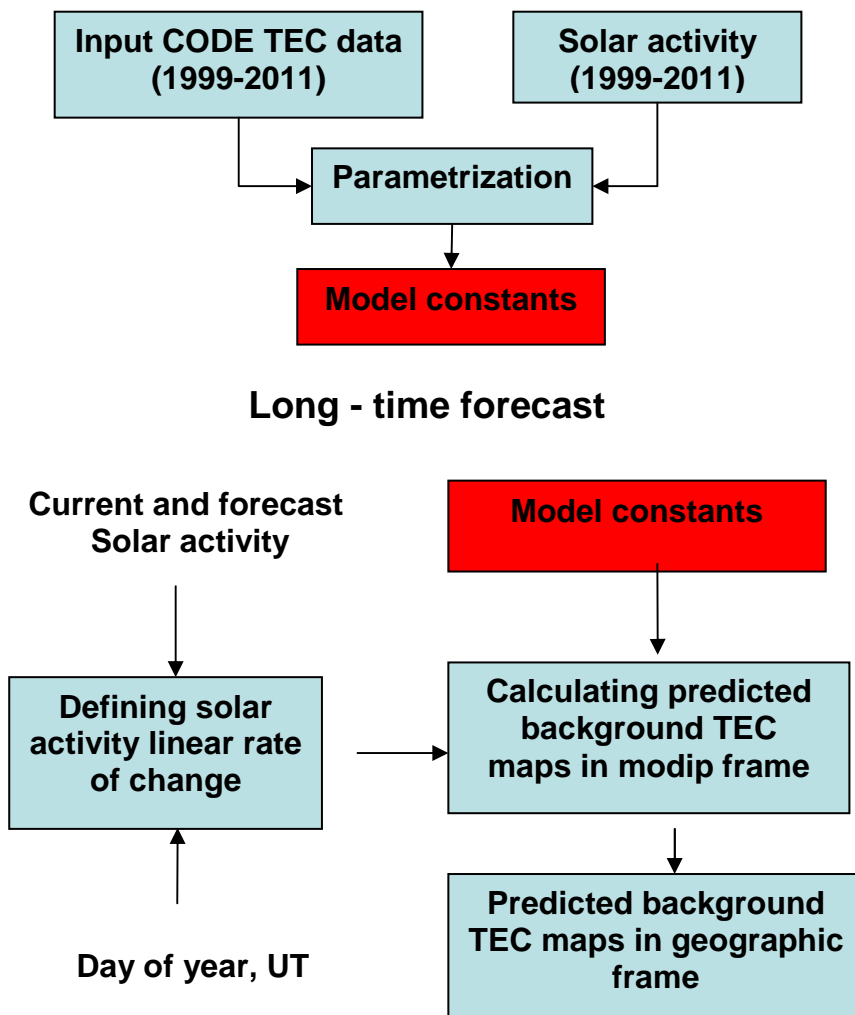
Figure 8 The block chart of the TEC model for long-term prediction

2. Statistical evaluation of the global background TEC model

2.1 General Evaluation of the Background TEC Model

An important aspect of the model development process is the evaluation of model performance comprehensively and objectively. This means that we have to represent an objective and meaningful description of the model's ability to reproduce reliable observations precisely or accurately, i.e. to determine the extent to which model-predicted events approach a corresponding set of reliable observations To gain even further insight into the nature and sources of the model's error variable we study in detail the solar, seasonal and diurnal variability of the error and on the base of the obtained results we will present an error model as well.

In Section 1 we have already presented the overall statistical assessment of the model based on the entire data set. The model performance has been represented by the mean (systematic) error (*ME*), root mean squares error (*RMSE*) and the standard deviation error (*STDE*) calculated with the expressions (4) in the Section 1. It has been found that the background model fits to the CODE TEC input data with a zero systematic error and a *RMSE=STDE*=3.387 TECU. The empirical probability density distribution of the model's error is shown in Figure 9a (black line). It is almost a symmetric function and bears a resemblance in some way to the Laplace distribution, shown in Figure 1a by red line (calculated at the same mathematical expectation and variance as the empirical one), but has also significant differences particularly around errors close to zero. The confidence limits of the error at a given probability are determined empirically by numerical integration of the probability density function shown by black line in Figure 9a. Figure 9b shows the probability for obtaining a given error expressed in times *STDE* (i.e. the empirical error function). Figure 9b reveals that the 90% probability corresponds to an error interval from -1.5*STDE* to 1.5*STDE*, i.e. from about -5 to 5 TECU. This means that there is a 90% probability that deviations larger than 5 TECU between the model and the CODE TEC data would not occur.
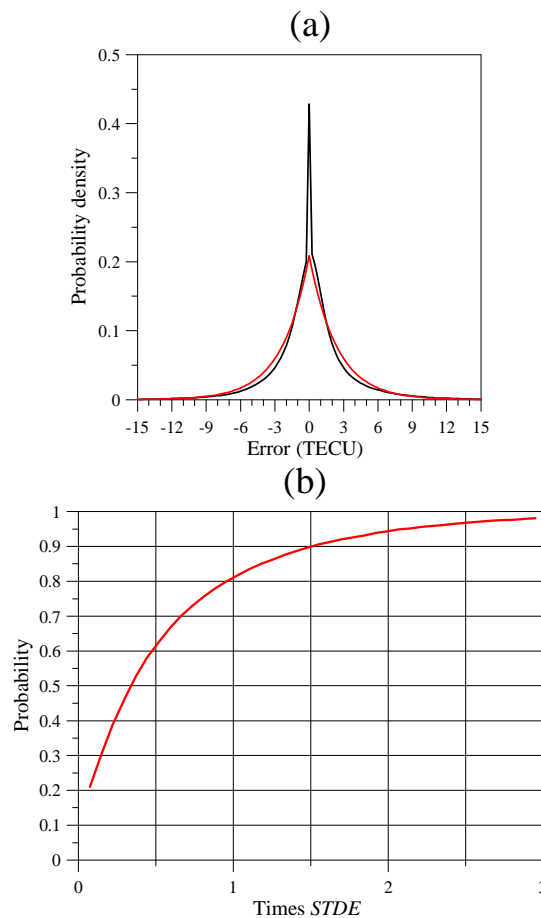
Figure 9 (a) Empirical probability density distribution of the model's error (black line) compared with the respective (calculated at the same mathematical expectation and variance as the empirical one) Laplace distribution (red line); **(b)** Probability for obtaining a given error expressed in times *STDE*.

The overall statistics of the model error can be defined more precisely by showing its dependence on LT and modip latitude. Figure 10 shows the mean (systematic) error (*ME*) dependence on modip latitude and LT. It is seen that it reaches the largest values of ±0.7 TECU (insignificant error) mainly at low- and low-middle latitudes. The *ME* variability reflects the fact that the fifth harmonics of the solar day (4.8-hour tidal component) is not included in the background TEC model.
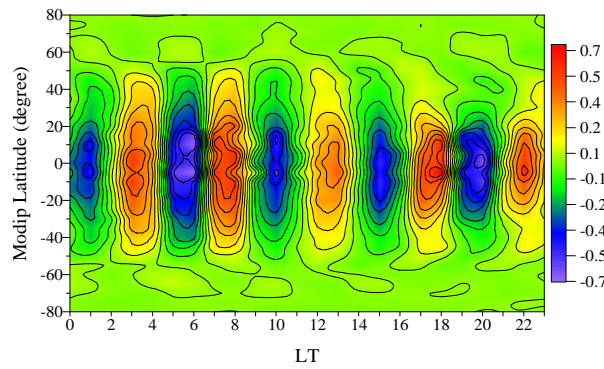
Figure 10 Mean (systematic) error dependence on modip latitude and LT
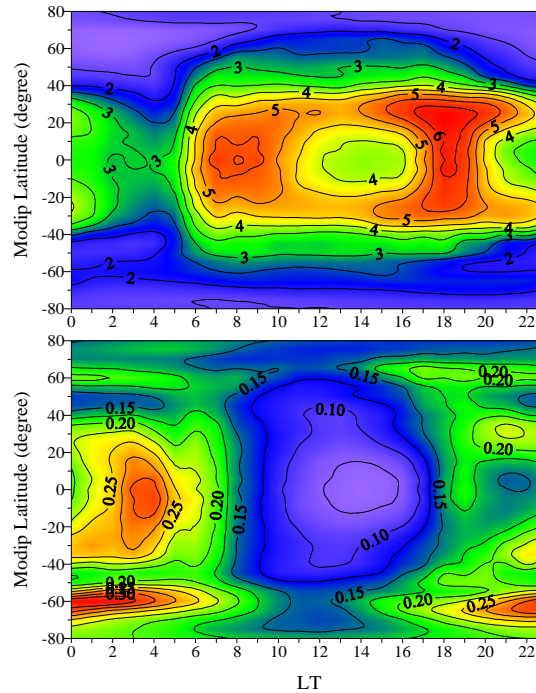
Figure 11 Dependence of *RMSE* (upper plot; the contour distance is 0.5 TECU) and relative *RMSE* (bottom plot, the contour distance is 0.025) on modip latitude and LT.

Figure 11 shows the *RMSE* distribution (upper plot; the contour distance is 0.5 TECU) with respect to the modip latitude and LT. The largest errors are obtained around sunrise (~8 LT) and sunset (~18 LT). While the sunrise errors maximise above the equator (and this is normal because of the absence of equatorial ionization anomaly those at sunset maximise not only above the equator but also at $\pm30^o$ modip latitude, i.e. at the equatorial anomaly crests. The errors at the northern equatorial anomaly crest are slightly larger than those at the southern crest. This result could be connected with the asymmetric behaviour of the migrating diurnal (DW1) and semidiurnal (SW2) tidal components seen at the left column of plots in Figure 2 of Section 1. Both tidal components are stronger in the Northern Hemisphere (NH) however this asymmetry for the DW1 is better expressed at high solar activity while for the SW2 is well seen at low solar activity. This asymmetric tidal behaviour is not well described by the background TEC model. The bottom plot of Figure 11 presents the relative *RMSE* distribution (the contour distance is 0.025) with respect to the modip latitude and LT. It is seen that the relative error is small during the daytime (between 8 and 18 LT) everywhere; it is particularly small, not more than 5%, between 12 and 16 LT around the dip equator. The largest relative errors of ~30% can be distinguished between 2 and 4 LT above the dip equator and between 18 and 6 LT (night-time) at around -60° modip latitude. The former largest relative error area is most probably related to the temperature and broad plasma anomalies (*Huang at al.*, 2012) observed above the equator around and after midnight; they are considered as part of the tidal pattern. The latter largest relative error area is surely related to the WSA discussed in the

Section 1. This means that nevertheless that the background TEC model is able to model the WSA its variability is a source of large errors. Some increase of the relative error is seen also at about $\pm30^{o}$ modip latitude between 20 and 23 LT which is most probably related to oscillations in the equatorial evening pre-reversal electric field (F-region vertical drift) and their effect on the variability of the plasma irregularities.

2.2 Basic Approach of the Error Model Construction

In order to asses the dependence of the error on the solar activity, seasons and LT we have to demonstrate how the model's error changes at different conditions. For this purpose we calculated the monthly mean values of the *RMSE* for the considered period of time, 1 January 1999 – 31 December 2011. The left column of plots in Figure 12 shows the modip latitude-time cross sections of the monthly mean *RMSE* at different LT: 00LT (most upper plot), 08LT (second from above plot), 12LT (third from above plot) and 18LT (bottom plot). It is clearly evident that the model's errors are larger during high solar activity (i.e. solar cycle dependence), at equinoxes (i.e. have seasonal dependence) and they depend on LT. All the above mentioned dependences are very similar to those of the TEC itself. Similarly to the TEC model here also the time scales of the error variability related to the solar cycle, season and LT are very different. Therefore for building the error model we use the same approach as that applied in constructing the background TEC model and the RMSE can be represented as:

$$RMSE(F, K_F, month, LT) = \Psi_1(F, K_F)\Psi_2(month)\Psi_3(LT) \qquad (5)$$

Similarly to the TEC model here also the above right hand side unknown functions Ψ_k *(k=1,2,3)* can be represented by their series expansions; Ψ_1 can be expanded in Taylor series, while Ψ_2 *and* Ψ_3, which are periodic functions with periods respectively a year (12 months) and a solar day (24 hours), can be expanded in Fourier series. Therefore, at each modip latitude the error model can be described by the following functions:

$$RMSE(F, K_F, month, LT) = \left(a_0 + a_1 F + a_2 K_F + a_3 F^2 + a_4 F K_F + a_5 K_F{}^2\right) \times$$
$$\left(b_0 + \sum_{i=1}^{4} b_i \cos\left(i\frac{2\pi}{12}month - \theta_i\right)\right) \times \qquad (6)$$
$$\left(c_0 + \sum_{i=1}^{4} c_i \cos\left(i\frac{2\pi}{24}LT - \lambda_i\right)\right)$$

The expression in the first right hand bracket, i.e. the Taylor series expansion up to degree of 2, represents the solar activity term which modulates the seasonal and diurnal behavior of the *RMSE*. Similarly to the Section 1 here also *F* is the solar radio flux at 10.7 cm wavelength (F10.7) and K_F describes the linear rate of change of F10.7. The seasonal term (expression in the second right hand bracket) includes besides the yearly mean (b_0) also 4 subharmonics of the year, i.e. annual, semiannual, 4- and 3-month components; it modulates the diurnal behavior of the *RMSE*. In this case the diurnal variability of the *RMSE* model (expression in the third right hand bracket) is composed however only by two terms: daily mean *RMSE* (c_0) and a term describing the migrating tides. This is due to the fact that the *RMSE* depends mainly on the LT. The contribution of the migrating tides in (6) includes 4 subharmonics of the solar day, i.e. 24-, 12-, 8- and 6-hour components.

The error model described by (6) contains 486 constants (we remind that (6) is applied at each modip latitude) and they are determined by least squares fitting techniques. Similarly to the TEC model here also the numbers of the included components in the Taylor and Fourier expansion series are defined experimentally. We accepted only the above mentioned solar, seasonal and diurnal

components because the addition of more components does not improve significantly the error of the error model.
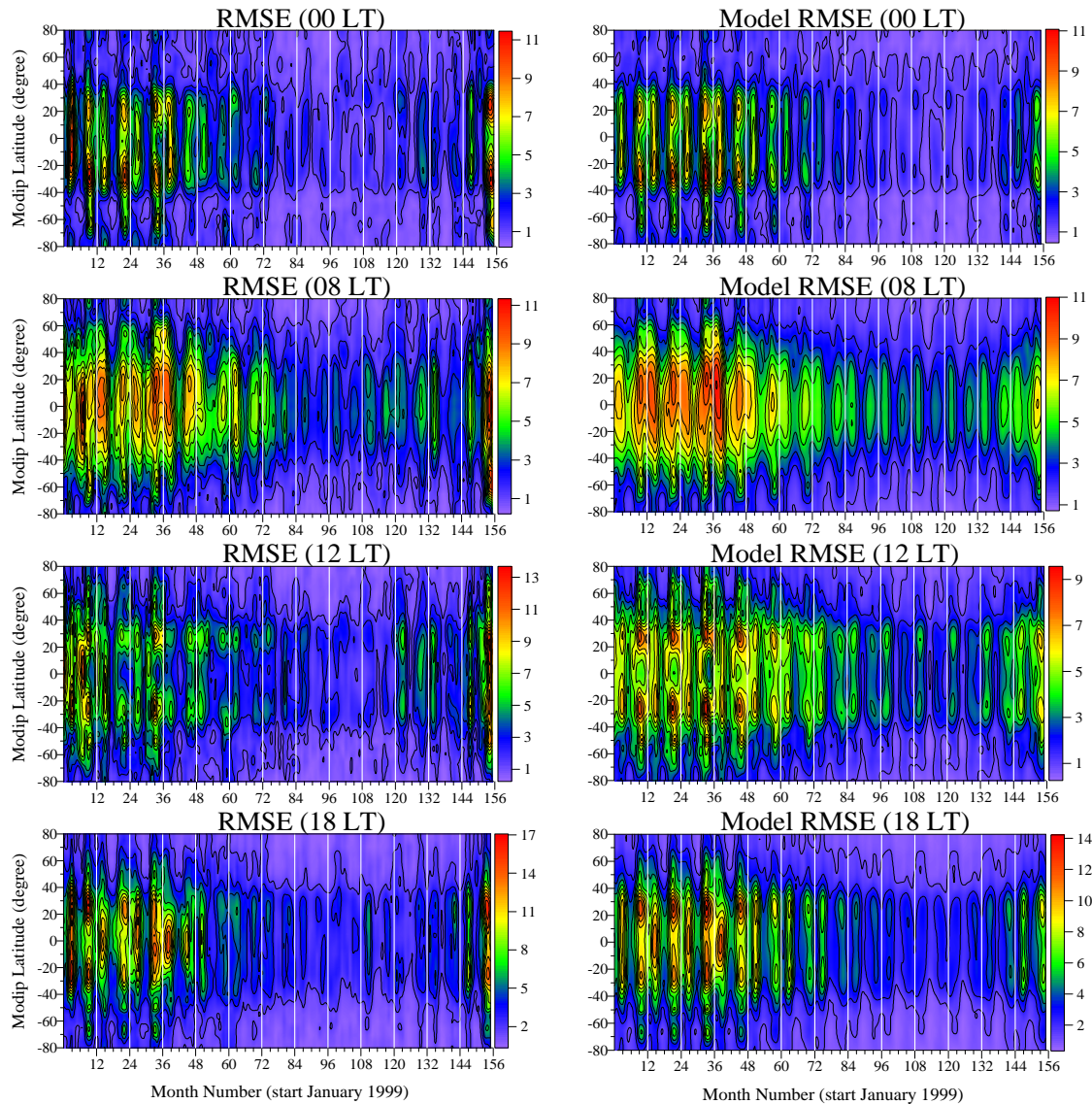
Figure 12 (left column of plots) Modip latitude-time (months) cross-sections of the calculated monthly mean *RMSE* at different local times: 00 LT (most upper plot), 08 LT (second from above plot), 12 LT (third from above plot) and 18 LT (bottom plot); (right column of plots) the same as the left column of plots but for the model *RMSE*.

The error model offers a prediction approach on the basis of which we can predict the *RMSE* depending on the solar activity, season and LT. Therefore, we've built not only a global empirical background TEC model but also a global prediction of the model's error at different solar, seasonal and LT conditions. The overall standard deviation of the predicted *RMSE* with respect to the empirical obtained one is 0.7 TECU. The right column of plots in Figure 12 presents the same results as the left column of plots but for the model *RMSE*. The detailed comparison between the real and model RMSE reveals some important features. The error model describes very well the real *RMSE* at 00 and 08 LT; it is able to reproduce not only qualitatively, but also quantitatively solar and seasonal dependences of the *RMSE*. The error model is able to reproduce even the hemispheric asymmetry of the *RMSE* well seen particularly at high solar activity; it is larger in the SH at 00 LT and in the NH at 08 LT. The error model performance at 12 and 18 LT is not as good as that at 00 and 08 LT. The model has not been able to reproduce well particularly the large errors seen in 1999,

2001 and 2011. Generally however the error model describes correctly the solar and seasonal dependences of the RMSE and its global distribution.

2.3 Application of the Error Model

The global empirical background TEC model, described in Section 1, offers TEC maps which depend on geographic coordinates (5^ox5^o in latitude and longitude) and UT at given solar activity and day of the year. The error model however does not depend on the geographic longitude because only the contribution of the migrating tidal components is considered in the model. In this way the error maps depending on the geographic latitude and LT at given solar activity and month of the year have to be constructed. The conversion of the modip latitude to geographic one is done at the Greenwich meridian. The error values assigned to both poles are the same as those at the highest northern and southern latitudes.

In order to demonstrate the ability of the error model to reproduce the spatial-temporal features of the real *RMSE* at different solar activity and seasons we use the examples given in the Section 1 (Figures 5, 6 and 7), i.e. we will compare the real and model *RMSE* for 2001, 2004 and 2008 as years representing high, middle and low solar activity and months January, March, July and October as typical winter, spring, summer and autumn months.
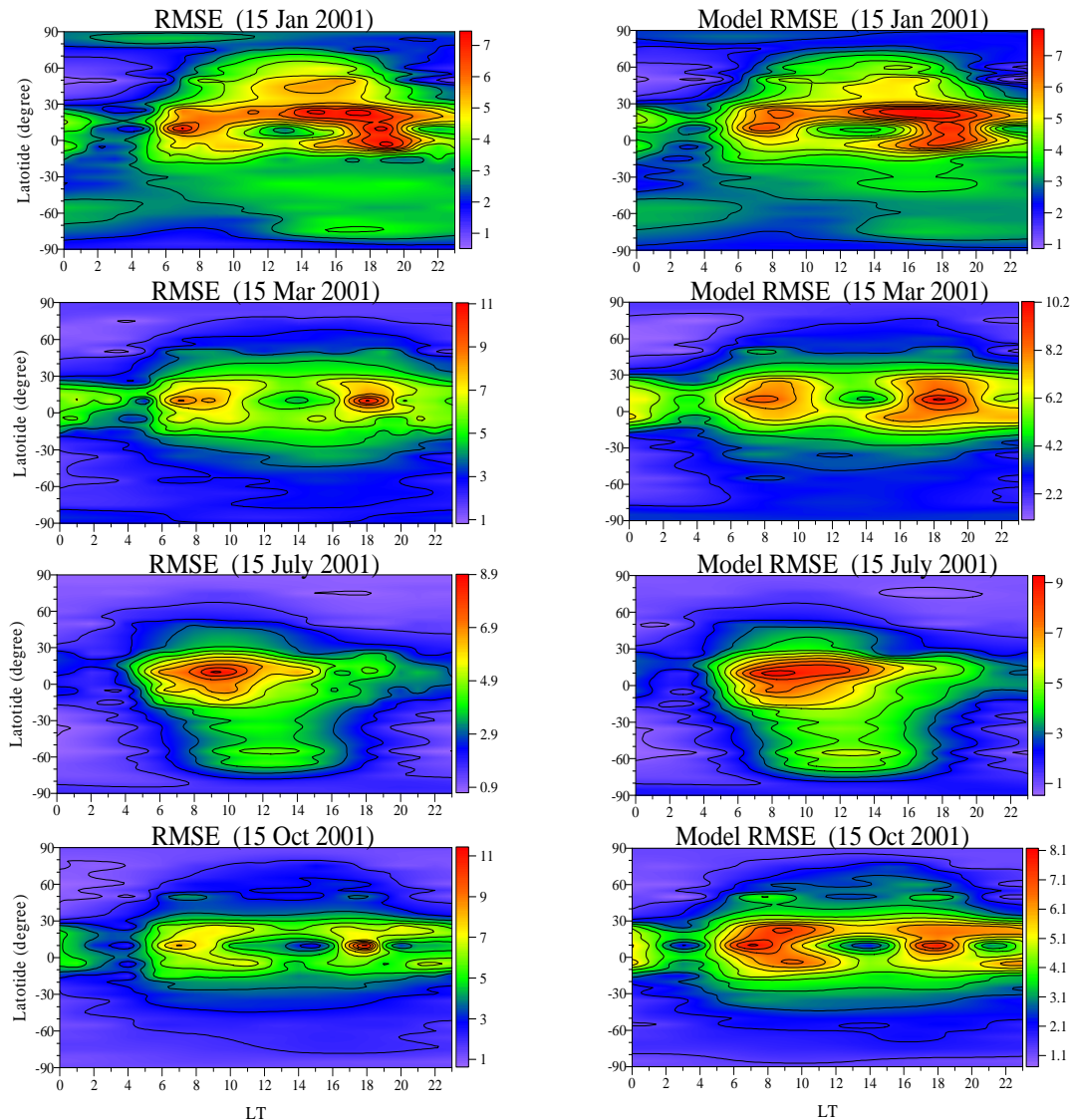
Figure 13 Latitude-LT cross sections of the real (left column of plots) and model (right column of plots) *RMSE* for 15 January (upper row of plots), 15 March (second from above row of plots), 15 July (third from above row of plots) and 15 October (bottom row of plots) at high solar activity 2001.

Figure 13 presents latitude-LT cross sections of the real (left column of plots) and model (right column of plots) *RMSE* for 15 January (upper row of plots), 15 March (second from above row of plots), 15 July (third from above row of plots) and 15 October (bottom row of plots) at high solar activity 2001. The latitude-LT distributions of the real and model *RMSE* in January (upper row of plots) are very similar not only qualitatively but quantitatively as well. As usually the largest errors are seen at both plots around sunrise (~6-8 LT) and sunset (~16-20 LT); large errors are found at both plots also near 20°N mainly during the daytime (~6-20 LT) and above the equator at sunset. The degree of similarity between the real and model *RMSE* in March (second from above row of plots) is also very high; at both plots the errors are symmetrically distributed with respect to latitude of ~10°N (because of difference between modip and geographic latitudes). Again the largest errors at both plots are seen near sunrise (~7 LT) and sunset (~18 LT) but while the maximum real *RMSE* is 11 TECU that of the model *RMSE* is slightly weaker, i.e. it is 10 TECU. The comparison between summer (July) real and model *RMSE* (third from above row of plots) again demonstrates high degree of similarity, qualitatively and quantitatively. In this case the largest errors are seen only in the morning hours (~8-10 LT) and at ~20°N, but not during the sunset. The qualitative similarity between the real and model *RMSE* in October is very good however the model errors are smaller than those of the real *RMSE*, i.e. they are 8.1 TECU and 11 TECU respectively.

Figure 14 The same as Figure 5 but at low solar activity 2008.

Page 26 of 57
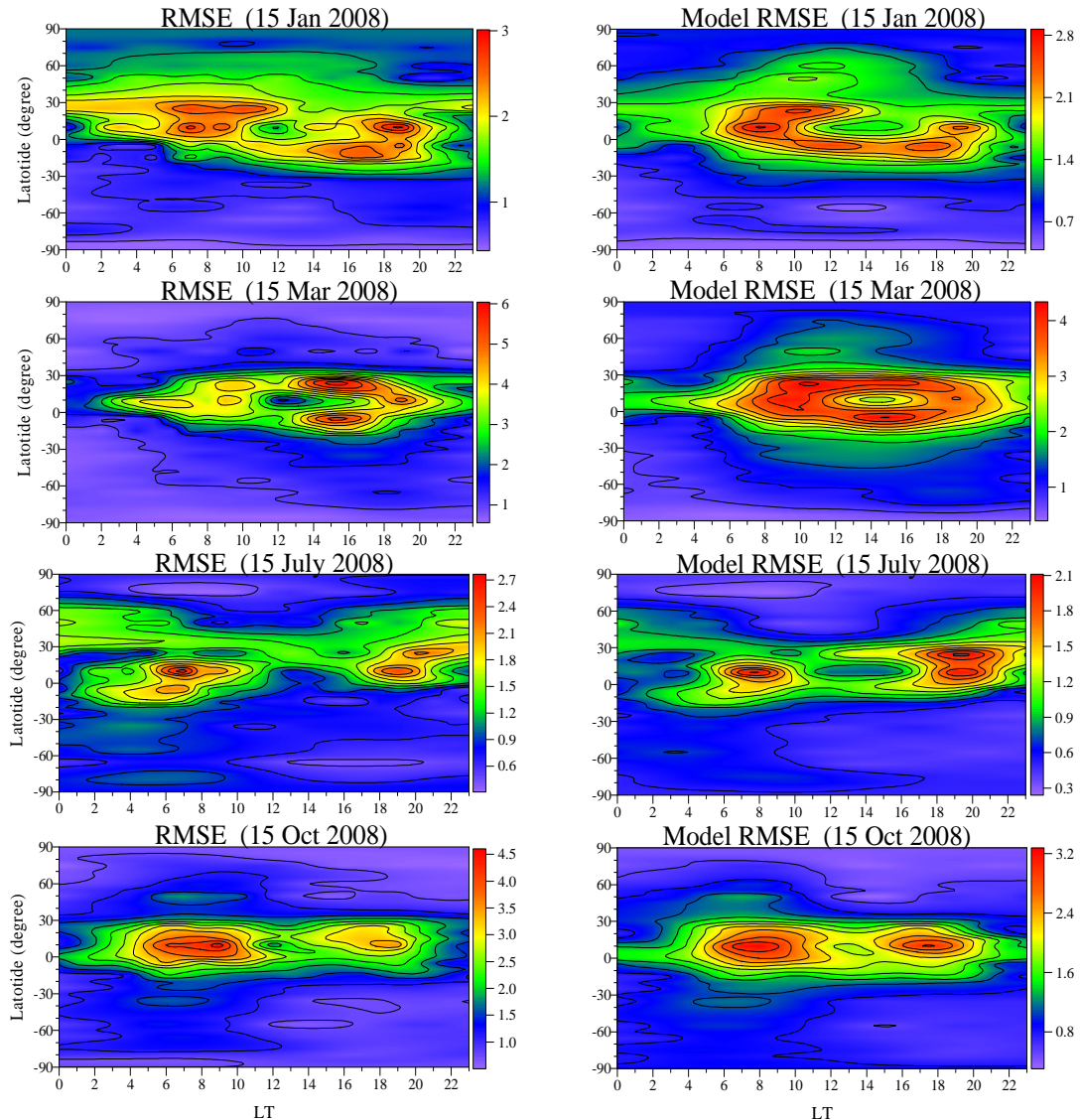
Figure 14 shows the same comparison as that in Figure 13 but for low solar activity 2008. In this case both real and model *RMSE* drastically decrease. The model describes qualitatively very well the latitude-LT distribution of the real *RMSE* at all months; there is some quantitative difference mainly during the equinoxes. As it has been expected the largest errors are found at equinoxes both in real and model *RMSE* but the error model underestimates the *RMSE*; in March the model and real *RMSE* are respectively 4 and 6 TECU, while for October the difference is smaller and they are 3.2 and 4.5 TECU. Some hemispheric asymmetry of both real and model *RMSE* is seen in winter (January) and summer (July) here as well but it is not predominantly in the NH as it was at high solar activity 2001 (Figure 13). In January both real and model *RMSE* at sunrise and morning hours are stronger in the NH while at afternoon and sunset hours they are larger in the SH. The opposite asymmetry is seen in July.
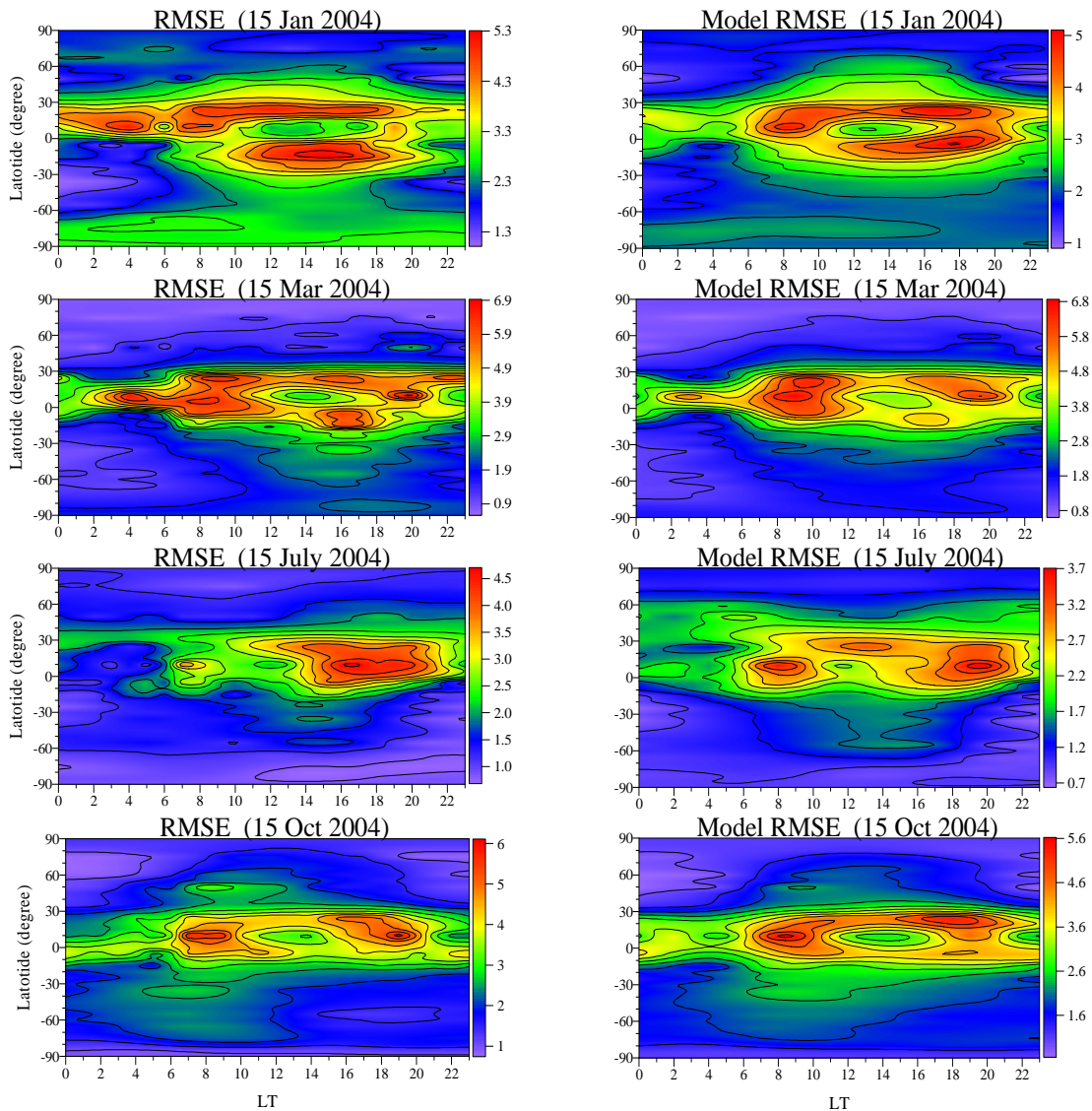
Figure 15 The same as Figure 5 but at middle solar activity 2004.

Figure 15 presents a comparison between real and model *RMSE* maps at middle solar activity 2004. It is seen that both the real and model *RMSE* at all months are between those at high (Figure 13) and low (Figure 14) solar activity, as it is expected in advance. At all months the real and model largest values are similar but in March they are almost the same, i.e. 6.9 and 6.8 TECU. The largest difference is seen in July when the maximum real *RMSE* is 4.5 TECU while the model one is 3.6

TECU. During the daytime almost at all months the NH errors are larger than those in the SH; only in January both the real and model *RMSE* distribution and the real *RMSE* in March are more hemispheric symmetric. Similarly to high solar activity here also the increase of *RMSE* during daytime and at ~20°N is a consequence of the hemispheric asymmetry of the diurnal components DW1 and SW2 contribution to the equatorial anomaly which is not well reproduced by the background TEC model. While the night time (~2-4 LT) amplification of the *RMSE* in March is comparatively well reproduced that observed in January is underestimated.

2.4 Concluding comments

A detailed statistical evaluation of the global empirical background TEC model, presented in Section 1, is done in Section 2. The model performance has been described by its mean (systematic) error (*ME*), root mean squares error (*RMSE*) and the standard deviation error (*STDE*). It was found that the background model fits to the CODE TEC input data with a zero systematic error and a *RMSE=STDE*=3.387 TECU. Based upon this overall error measures we may confidently conclude that this model is able to reproduce accurately the CODE TEC input data. It was found that the empirical probability density distribution (Figure 9a) resembles more the Laplace than the normal, or Gaussian, distribution. This result could be probably related to the non-Gaussian statistics of the ionospheric irregularities. The empirical error function shown in Figure 9b revealed that there is only 10% probability that deviations larger than 5 TECU between the model and the CODE TEC data would occur. The modip latitude-LT distributions of the model's error showed predominantly known features, as: (i) the small *ME* observed mainly at low latitudes reflects the fact that the fifth harmonics of the solar day (4.8-hour tidal component) is not included in the background TEC model (Figure 10); (ii) the *RMSE* are large at sunrise and sunset time (Figure 11 upper plot), and (iii) the relative RMSE amplifications shown in the bottom plot of Figure 11 are related to comparatively stable ionospheric anomalies which are present at some local times and latitudes (as WSA, broad plasma anomaly after midnight and evening pre-reversal plasma irregularities at equatorial latitudes).

To gain further insight into the nature and sources of the model's error variable we studied in detail the solar, seasonal and diurnal variability (LT) of the model's error. On the base of the obtained results we built an error model (Mukhtarov et al., 2013b). It actually offers a prediction approach on the basis of which we can predict the *RMSE* depending on the solar activity, season and LT. The error model was constructed by using a similar approach to that of the background TEC model itself. Similarly to the TEC model here also the time scales of the error variability related to the solar cycle, season and LT are very different. Then the spatial-temporal variability of the *RMSE* was presented as a multiplication of three separable functions (as it is shown in (6)). The solar cycle and seasonal dependences of the *RMSE* are described in the same way as in the background TEC model. The Taylor series expansion up to degree of 2 represents the solar activity function while the seasonal function includes the contribution of 4 subharmonics of the year, i.e. annual, semiannual, 4- and 3-month components. The *RMSE* depends mainly on the LT and due to this its diurnal variability is described only by the migrating tides; four subharmonics of a solar day, 24-, 12-, 8- and 6-hour components are included in the error model. It contains 486 constants which have been determined by least squares fitting techniques. The overall standard deviation of the predicted *RMSE* with respect to the empirical one is 0.7 TECU. The detailed comparisons between real and model *RMSE* shown in Figures 13, 14 and 15 clearly demonstrate that the error model describes correctly and precisely the spatial-temporal variability of the *RMSE*.

It is important to note that these two sections present not only a global empirical background TEC model (Mukhtarov et al., 2013a) but also a global prediction of the model's error at different solar, seasonal and LT conditions (Mukhtarov et al., 2013b). At given solar activity and day of the year the background TEC model offers TEC maps which depend on geographic coordinates (5°x5° in latitude and longitude) and UT. The error model offers a prediction approach on the basis of which the *RMSE* depending on the solar activity, season and LT can be predicted.

3. Development of global empirical model of TEC response to geomagnetic activity

The model is constructed on the basis of the same CODE TEC data set. The geomagnetic activity is defined by the global K_p-index. The K_p-index data are downloaded from the Space Physics Interactive Data Resource (SPIDR), Boulder, Colorado for the considered period of time. The K_p value at every hour is used in this study as it is obtained by linear interpolation of the three-hour K_p values.

In the model the TEC response to the geomagnetic activity is investigated by the relative deviation of the TEC defined as: $rTEC = (TEC_{obs}-TEC_{med})/TEC_{med}$. The terms TEC_{obs} and TEC_{med} represent observed and median TEC values respectively at a given hour. In the present study we use sliding medians defined by a 15-day moving window and the median value is assigned to the last day of the window, i.e. to the 15th day of the window. We use such type of "one-sided" median approach because in this case the model is built in a way as it will be used for short-term prediction (usually 24 hours ahead). In other words we try to predict the correction to the 15-day median values for each hour of the prediction period. The window length of 15 days is used because the preliminary examinations showed both strong depression of the ~27-day rTEC variability due to analogous variations in the EUV radiation and an insignificant effect on the 9- and 13.5-day recurrent geomagnetic activity particularly strong in declining phase of the solar activity. By considering the characteristic rTEC the effect of the regular seasonal, diurnal and solar changes is removed from the TEC variability. The data are grouped into 12-month bins as every bin contains all the available hourly data within the respective month of the year.

3.1 Cross-correlation analysis between rTEC and K_p-index and its theoretical substantiation

The investigations on the f_oF2 response to the geomagnetic activity, presented by Muhtarov and Kutiev (1998) and Kutiev and Muhtarov (2003), indicated that this is a delayed response. The authors expressed the delay in terms of the time constant of their cross-correlation function and found a time delay constant of about 18 hours. Then the first step in this study is to calculate the 2D cross-correlation functions between the K_p-index and rTEC.

3.1.1 Empirical cross-correlation functions

The effect of geomagnetic activity, described by the K_p-index, on the rTEC variability is investigated by 2D cross-correlation analysis between both parameters. In the case of building global TEC model we expect that the cross-correlation function will depend on the season, modip latitude, longitude and LT. Due to these dependences three different types of 2D cross-correlation functions are calculated: (i) longitude-time lag; (ii) LT-time lag, and (iii) modip latitude-time lag. The 2D cross-correlation functions are calculated for each month of the year because they depend on the season as well. Only some examples of the above mentioned three types of the 2D cross-correlation functions will be shown here through which the main features of the geomagnetic effects on the rTEC can be demonstrated.

Figure 16 presents 2D (longitude-time lag) cross-correlation functions calculated between the rTEC and K_p-index for January at different modip latitudes: equator (upper most plot), $\pm20^o$ (upper row of plots), $\pm40^o$ (middle row of plots) and $\pm70^o$ (bottom row of plots). The 2D cross-correlation functions from both hemispheres are shown in order to demonstrate the seasonal dependence of the TEC response to the geomagnetic activity; winter in the Northern Hemisphere (NH) and summer in the Southern Hemisphere (SH). The time lag up to 72 hours is shown because in general the response is composed by two phases, positive and negative with different duration and time delay.
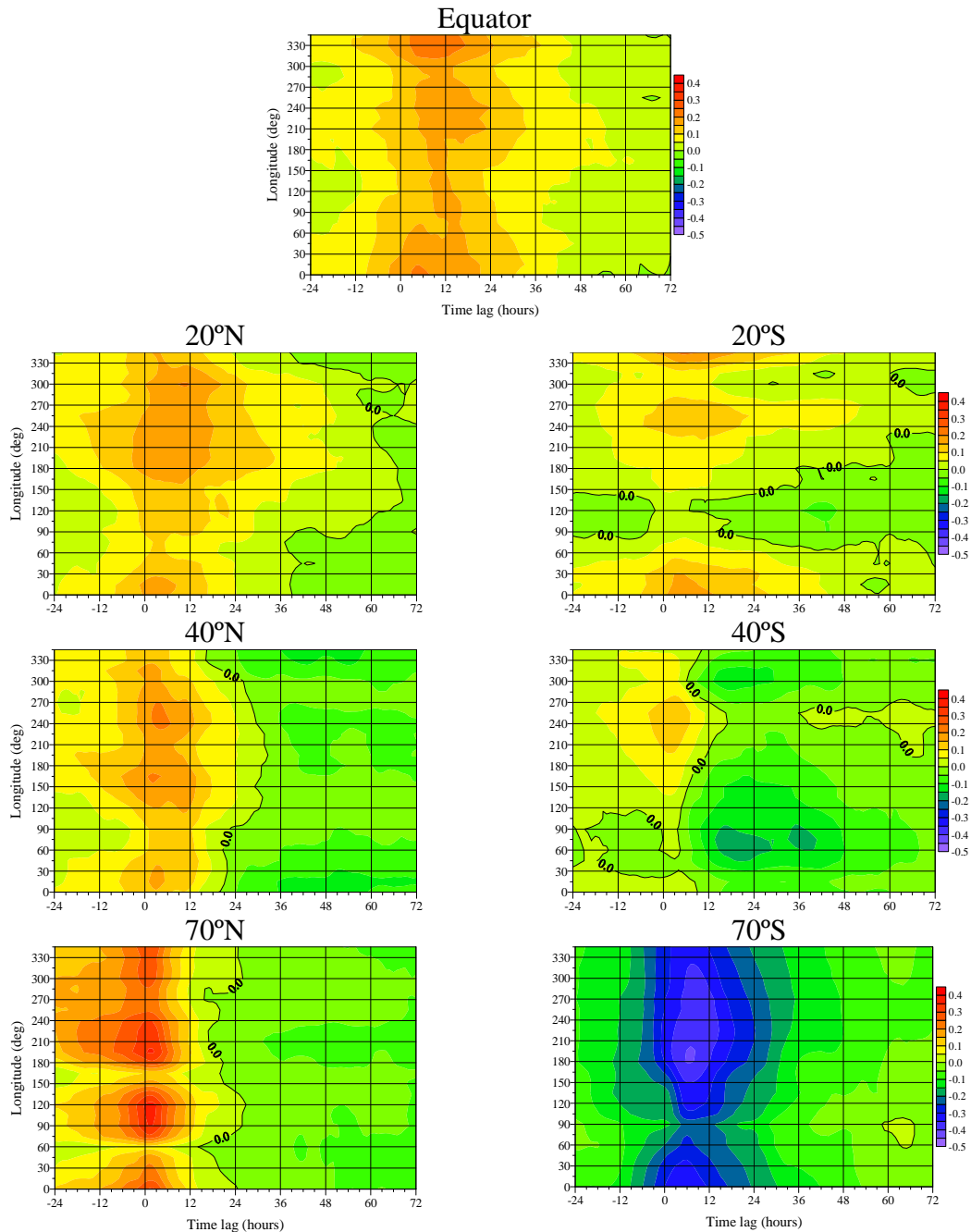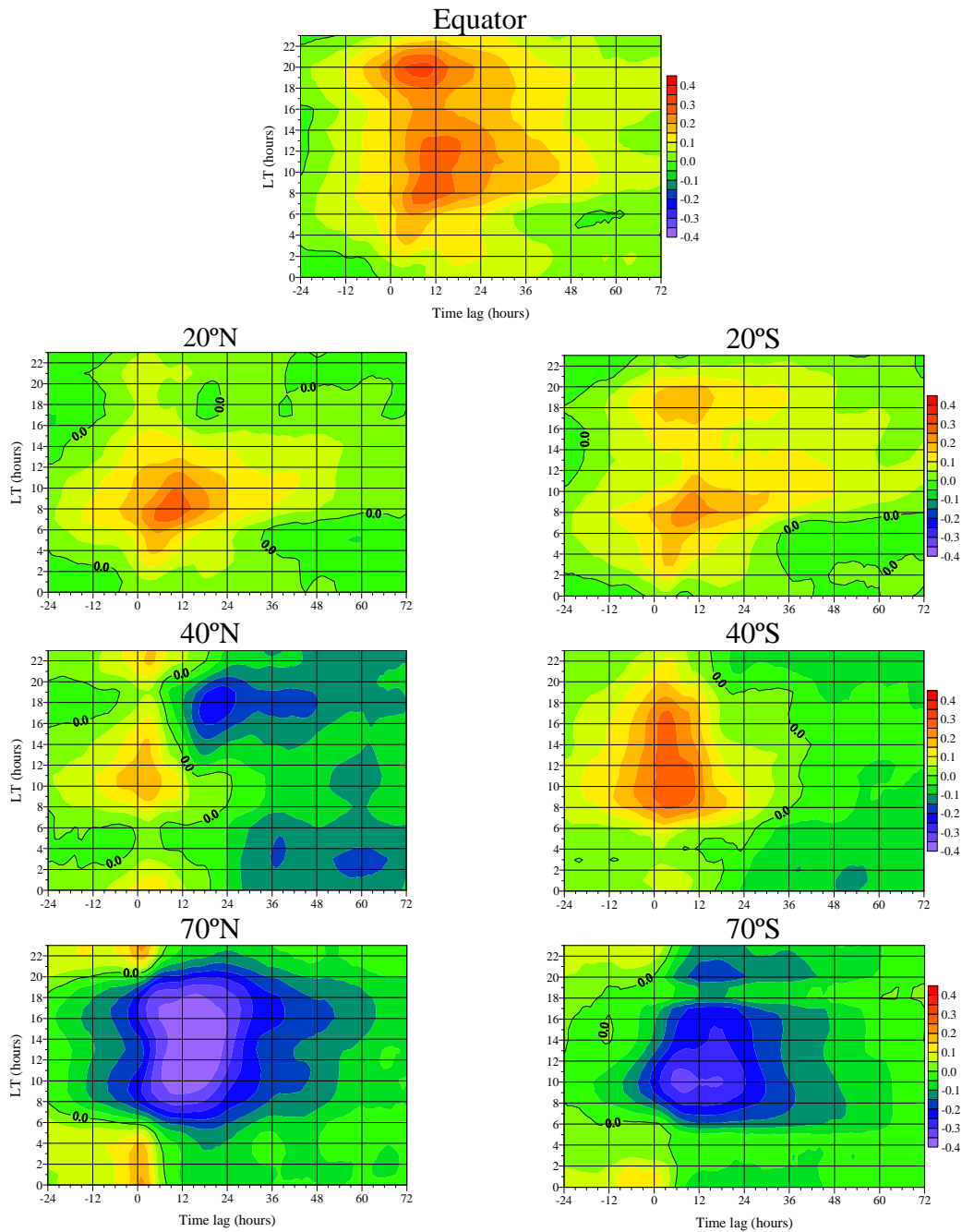
Figure 16 Two-dimensional (longitude-time lag) cross-correlation functions calculated between the rTEC and K_p-index for January at equator (upper most plot), $\pm 20^o$ (upper row of plots), $\pm 40^o$ (middle row of plots) and $\pm 70^o$ (bottom row of plots); the zero time lag is marked by tick black line.

Some main features of the cross-correlation can be distinguished from Figure 16: (i) the rTEC response to the Kp-index shows clear longitude and even some wave-like dependence; in the NH (winter) a wavenumber 3 response can be seen while in the SH (summer) and over the equator in general wavenumber 2 can be clarified; (ii) two types of response, positive and negative, can be seen at all plots (the zero time lag is marked by tick black line); first the response is positive at all modip latitudes except that at 70°S (i.e. summer high latitudes where the cross-correlation reaches maximum of -0.5 with an average time lag of 6 hours), and then it is negative; above the equator it is mainly positive; (iii) the maximum positive cross-correlation of +0.4 is seen at winter high latitudes (70°N) which is reached in the frame of 1-3 hours after the maximum Kp-index; with decreasing the modip latitude the time lag for reaching maximum increases and above the equator it

is on the average after ~9 hours. The results from Figure 16 reveal that in the global rTEC model a dependence on the longitude has to be included.

Figure 17 Two-dimensional (LT-time lag) cross-correlation functions calculated between the rTEC and K_p-index for September at equator (upper most plot), $\pm 20^o$ (upper row of plots), $\pm 40^o$ (middle row of plots) and $\pm 70^o$ (bottom row of plots); the zero time lag is shown by tick black line.

Figure 17 shows 2D (LT-time lag) cross-correlation functions calculated between the rTEC and K_p-index for September at the same modip latitudes as in Figure 16. In this case an equinoctial month is shown, autumnal month in the NH and vernal month in the SH. Again two types, positive and negative, of the rTEC response are seen at all plots. The following cross-correlation features can be summarized from Figure 2: (i) low-latitude rTEC response is mainly positive; the negative response is reached at large time lags; the maximum positive correlations are obtained between 8-10 LT and 18-20 LT with an average time lag of 6-9 hours for the tropics and 9-12 hours above the equator; (ii) middle ($\pm 40^o$) latitude rTEC response clearly indicates first positive and then negative phases with different durations; the maximum positive coefficients are reached during the day-time 10-12

Page 31 of 57

LT and around midnight with time lags of ~3 hours for the NH and between 3 and 6 hours for the SH; the negative response is stronger for the NH than that in the SH reaching maximum around 2-4 LT and ~18 LT; (iii) high ($\pm70^o$) latitude rTEC response is defined by negative phase during the day (6-20 LT) and a positive, almost instantaneous (zero time lag), response during the night; the negative response in the NH is stronger than that in the SH. The results from Figure 17 reveal that in the global rTEC model a dependence on the LT has to be included as well.
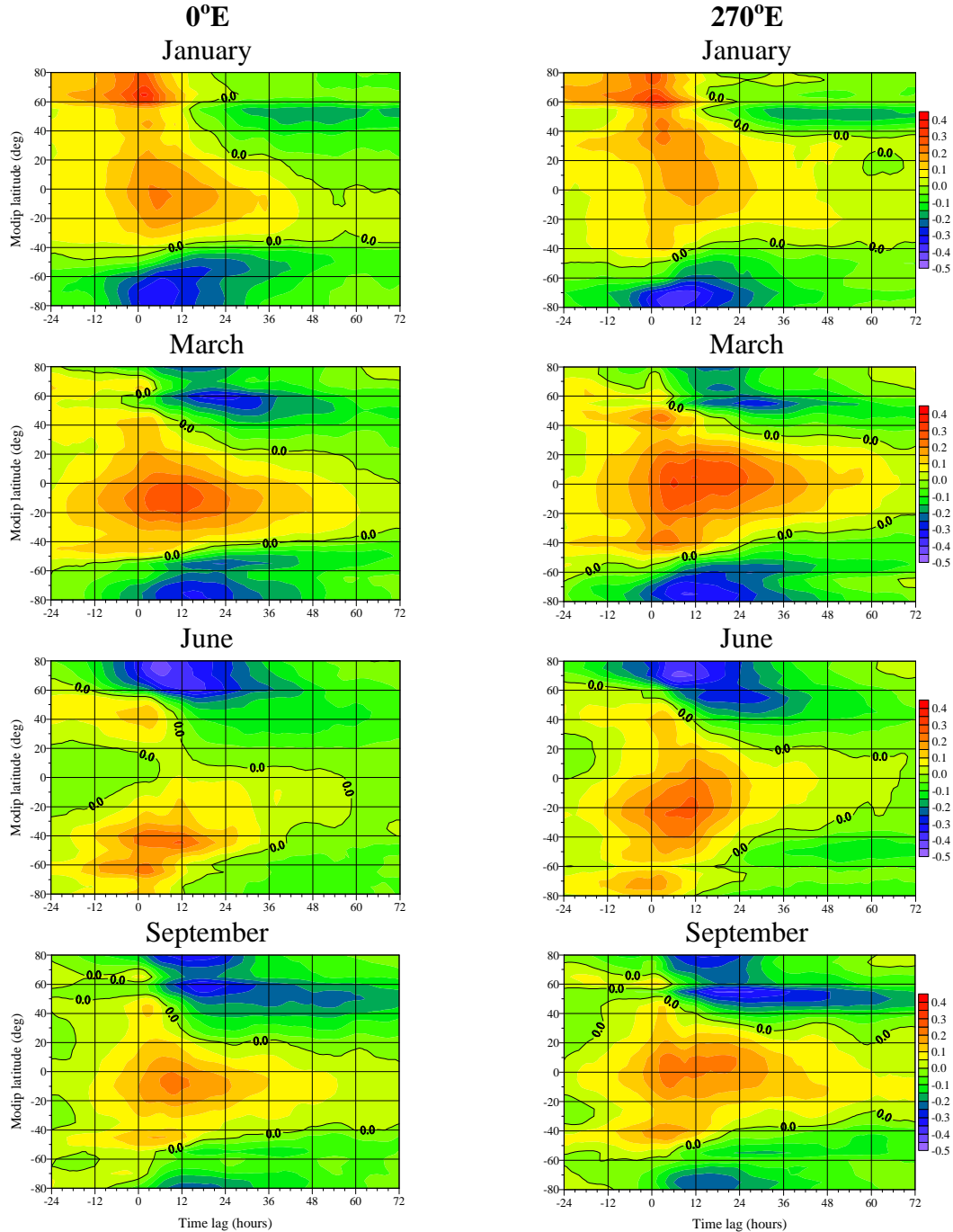

Figure 18 Two-dimensional (modip latitude-time lag) cross-correlation functions calculated between the rTEC and K_p-index for months: January (upper row of plots), March (second row of plots), June (third row of plots) and September (bottom row of plots) and at 0^oE (left column of plots) and 270^oE (right column of plots); the zero time lag is shown by tick black line.

Figure 18 presents the 2D (modip latitude-time lag) cross-correlation functions calculated between the rTEC and K_p-index for different months: January (upper row of plots), March (second row of plots), June (third row of plots) and September (bottom row of plots) and at two longitudes: 0^oE

(left column of plots) and 270°E (right column of plots). Again two types of rTEC response can be seen with different duration and time lag which depends on the season and modip latitudes. In general: (i) the tropical latitudes at all seasons have positive response with large time lags; (ii) while the winter high latitude rTEC has first positive response with short time lags and then weak negative one the summer rTEC demonstrates only negative response; (iii) the middle (up to ±50°) latitude rTEC response shows first a weak positive response with short time lags and then stronger negative response with large time lags. Considering all months of the rTEC responses the following feature can be drawn: the rTEC response in March/April is close to the winter response in the NH/SH and to the summer one in the SH/NH while the rTEC response in September/October is close to the summer response in the NH/SH and to the winter response in the SH/NH. Similar result but only for the NH was found in the regional TEC model (Andonov et al., 2011).

3.1.2 Theoretical cross-correlation function between rTEC and Kp-index

The main conclusion from all types of cross-correlation functions, shown in Figures 16, 17 and 18, is the existence of two types of the rTEC response, positive and negative, with different durations and time lags. Both responses depend on the longitude, modip latitude, season and LT. The cross-correlation results can be used for supporting the use of two different time constants in building the global empirical rTEC model in a way as it has been already done in the regional rTEC model over American sector (Andonov et al., 2011). The use of two different time constants hints for the simultaneous action of at least two different processes that define the rTEC response to geomagnetic activity. The existence of at least two processes is considered in Mukhtarov and Pancheva (2012) where the ionospheric response to the high speed solar wind streams is studied by using the COSMIC electron density measurements.

A method for modeling the cross-correlation function between the relative f_oF2 and the geomagnetic index is described in Muhtarov et al. (2002) where the delayed response is represented by a linear filter from the first order. Similar approach we apply in this study in order theoretically to base the use of two different time constants in establishing the global rTEC model response to the geomagnetic activity.

If we assume that the temporal variability of the geomagnetic index can be described as a stationary random process (for simplicity noted as $x(t)$) while the rTEC (noted here as $y(t)$) is a result of the converting the geomagnetic activity by two independent linear filters from the first order, then:

$$y(t) = \alpha \int_{-\infty}^{\infty} h_1(\xi)x(t-\xi)d\xi + \beta \int_{-\infty}^{\infty} h_2(\xi)x(t-\xi)d\xi \qquad (7)$$

The transition functions of the both filters can be denoted as:

$$h_1(t) = \begin{cases} \dfrac{1}{T_1}\exp\left(-\dfrac{t}{T_1}\right), t \geq 0 \\ 0, t < 0 \end{cases}$$

$$h_2(t) = \begin{cases} \dfrac{1}{T_2}\exp\left(-\dfrac{t}{T_2}\right), t \geq 0 \\ 0, t < 0 \end{cases} \qquad (8)$$

Thus the ionospheric response is represented as a linear combination of two delayed responses with time delay constants respectively T_1 and T_2 and coefficients of proportionality respectively α and β. Actually, the ionospheric response is not a deterministic process hence the above mentioned quantities have to be interpreted as characteristics of the most probable response at given conditions.

The cross-correlation function between the processes x and y is described by the interrelations of Wiener- Lee:

$$R_{xy}(\tau) = \int_{-\infty}^{\infty} (\alpha h_1(\xi) + \beta h_2(\xi)) R_{xx}(\tau - \xi) d\xi \qquad (9)$$

The autocorrelation function of the geomagnetic activity can be represented with sufficient accuracy [*Muhtarov et al.*, 2002] by an exponential function:

$$R_{xx}(\tau) = \sigma_x^2 \exp\left(-\frac{|\tau|}{T_g}\right) \qquad (10)$$

where the magnitude of the logarithmic decrement of $R_{xx}(\tau)$ is approximately 14 h (Muhtarov et al., 2002). Having in mind the above mentioned assumptions then the cross-correlation function can be expressed as:

$$R_{xy}(\tau) = \sigma_x^2 \left[\begin{array}{l} \alpha\left(\frac{T_g}{(T_1 - T_g)}\left(\frac{2T_1}{(T_1 + T_g)}\exp\left(-\frac{\tau}{T_1}\right) - \exp\left(-\frac{\tau}{T_g}\right)\right)\right) + \\ \beta\left(\frac{T_g}{(T_2 - T_g)}\left(\frac{2T_2}{(T_2 + T_g)}\exp\left(-\frac{\tau}{T_2}\right) - \exp\left(-\frac{\tau}{T_g}\right)\right)\right) \end{array} \right] \tau >= 0$$

$$R_{xy}(\tau) = \sigma_x^2 \left[\alpha\left(\frac{T_g}{(T_1 + T_g)}\exp\left(\frac{\tau}{T_1}\right)\right) + \beta\left(\frac{T_g}{(T_2 + T_g)}\exp\left(\frac{\tau}{T_2}\right)\right) \right] \tau <= 0 \qquad (11)$$

At $\tau=0$ both expressions and their first derivatives become equal. Figure 19 shows a comparison between the theoretical (described by formula (11)) cross-correlation function calculated for $T_1=12$ h, $T_2=32$ h, $\alpha=1$, $\beta=-1$ and for simplicity the variance of the geomagnetic activity is accepted to be 1(upper plot) and the empirical cross-correlation function between K_p-index and $rTEC$ for August
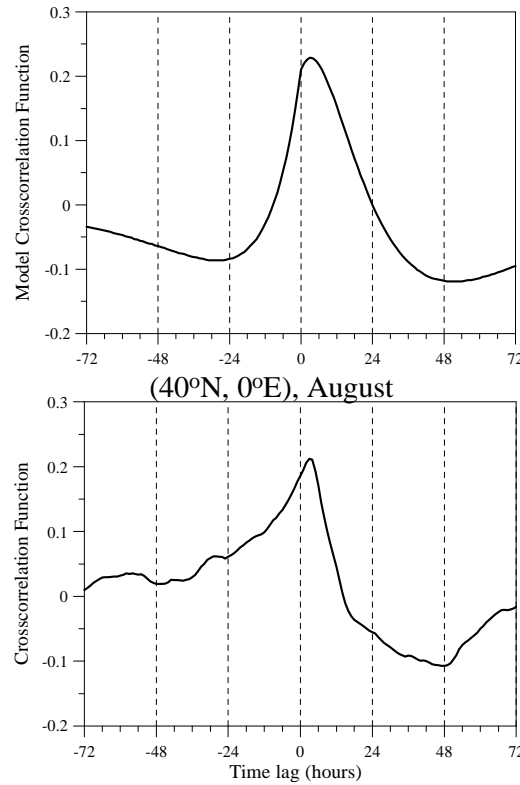
Figure 19 Comparison between the theoretical cross-correlation function (upper plot) calculated for $T_1=12$ h, $T_2=32$ h, $\alpha=1$, $\beta=-1$ and for simplicity the variance is accepted to be 1, and the empirical cross-correlation function between the K_p-index and $rTEC$ for August and at (40ºN, 0ºE) (bottom plot)

and at (40^oN, 0^oE) (bottom plot). It is seen that the main features of the two cross-correlation functions are very similar: a positive response with small time lag followed by a negative response with longer time lag. The assumption that the sum response is shaped by two responses: a positive with small time constant and negative one with three times longer time constant is set in the model. In this way at the range of positive time lag a near area of positive correlation and a distant area of negative correlation are formed. In the presence of only one process it is impossible both positive and negative correlations to be obtained. The investigation of the relative f_oF2 response to the geomagnetic activity in summer at the middle latitudes (Muhtarov et al., 2002; Kutiev and Muhtarov, 2003) indicated that the response is negative. In this study however the rTEC response at the same conditions is composed by positive and negative responses. This means that the positive response of the rTEC should be due to the positive response of the electron density above the F-region maximum.

3.2 Basic Approach of the Model Construction

The basic idea of each global empirical TEC model which describes the response to the geomagnetic activity is to define a set of analytical expressions which describe the most probable TEC values at given geomagnetic activity index, day of the year, geographic location and LT. The investigations on the f_oF2 response to the geomagnetic activity (Muhtarov et al., 2002) indicated that this is a delayed response which can be satisfactorily modeled by assuming that the geomagnetic influence is imposed on the inertial system described by an inhomogeneous differential equation from a first order (Kutiev and Muhtarov, 2003). In the present study the cross-correlation analysis however indicated that the rTEC response to the geomagnetic activity has to be presented by a sum of two responses with different time delay constants and with different sign of the cross-correlation function. It is known also that during the recovery phase of the ionospheric storms with geomagnetic origin the ionospheric reaction continues some time after the geomagnetic storm attenuation. This phenomenon aggravates the relationship between the K_p-index and the ionospheric anomalies. In order to resolve this problem Muhtarov et al. (2002) suggested an approach for defining new modified function of K_p-index, based on the time delay constant from the cross-correlation analysis, with its variations closely resembling those of the relative f_oF2. Having in mind the above mentioned ideas Andonov et al. (2011) constructed regional rTEC model over North America and the similar approach will be used in the present study as well.

If we assume that the impact of the geomagnetic activity on the rTEC is accomplished by two mechanisms with different time delay constants then the variability of rTEC can be described as follows:

$$rTEC(t) \approx \left(f_{Ts}\left(Kp_{Ts}(t)\right) + f_{Tl}\left(Kp_{Tl}(t)\right) \right) f_{lt}(LT) f_{lon}(Lon) \qquad (12)$$

where the functions $f_{lt}(LT)$ and $f_{lon}(Lon)$ represent the dependence of the rTEC response on the LT and longitude at equal other conditions. The parameters Kp_{Ts} and Kp_{Tl} are the modified with the time delay constants respectively T_s and T_l values of the K_p-index. These modified parameters are solutions of the equations shown below and are obtained easily by a numerical integration:

$$T_s \frac{dKp_{Ts}(t)}{dt} + Kp_{Ts}(t) = Kp(t) \qquad (13)$$

$$T_l \frac{dKp_{Tl}(t)}{dt} + Kp_{Tl}(t) = Kp(t) \qquad (14)$$

The unknown functions f_{Ts} and f_{Tl} from (1) can be expressed by their Taylor series expansions while the dependences on the LT and longitude can be presented by a Fourier series as follows:

$$f_{Ts}\left(Kp_{Ts}\right) = \alpha_{0s} + \alpha_{1s} Kp_{Ts}(t) + \alpha_{2s} Kp_{Ts}(t)^2 + .\alpha_{3s} Kp_{Ts}(t)^3 + ...$$

$$f_{Tl}\left(Kp_{Tl}\right) = \alpha_{0l} + \alpha_{1l} Kp_{Tl}(t) + \alpha_{2l} Kp_{Tl}(t)^2 + \alpha_{3l} Kp_{Tl}(t)^3 ...$$

$$f_{lt}\left(LT\right) = \beta_0 + \sum_{i=1}^{4} \beta_i \cos\left(i\frac{2\pi}{24}LT - \varphi_i \right) \tag{15}$$

$$f_{lon}\left(Lon\right) = \gamma_0 + \sum_{i=1}^{6} \gamma_i \cos\left(i\frac{2\pi}{24}Lon - \psi_i \right)$$

Then the rTEC can be described as:

$$rTEC\left(Kp_{Ts}, Kp_{Tl}, LT, Lon\right) = \begin{pmatrix} \left(\alpha_{0s} + \alpha_{1s} Kp_{Ts}(t) + \alpha_{2s} Kp_{Ts}(t)^2 + \alpha_{3s} Kp_{Ts}(t)^3\right) + \\ \left(\alpha_{0l} + \alpha_{1l} Kp_{Tl}(t) + \alpha_{2l} Kp_{Tl}(t)^2 + \alpha_{3l} Kp_{Tl}(t)^3\right) \end{pmatrix} \times$$

$$\left(\beta_0 + \sum_{i=1}^{4} \beta_i \cos\left(i\frac{2\pi}{24}LT - \varphi_i \right) \right) \times \left(\gamma_0 + \sum_{i=1}^{6} \gamma_i \cos\left(i\frac{2\pi}{24}Lon - \psi_i \right) \right) \tag{16}$$

We note that the Fourier time series (third relation in (15)) includes the contribution of four harmonics, 24, 12, 8 and 6 hours, while the Fourier longitude series (fourth relation in (15)) includes the contribution of 6 harmonics, i.e. the contribution of zonal waves with zonal wavenumbers up to 6. It is worth noting that the numbers of the included components in the Fourier expansion series are defined experimentally. We accepted only the contribution of the above mentioned diurnal components and zonal waves because the addition of more components does not improve the model error.

The next important step is to find a functional dependence between the K_p and rTEC in order to clarify the number of terms in the Taylor series (first two relations in (15)). The most appropriate type of the functional dependence is defined empirically by following the approach described in Andonov et al. (2011). Some examples of the empirical dependences between the K_p and rTEC calculated for different months and geographical points which are denoted at the plots, are presented in Figure 20. It is evident that in all cases the functional dependence between K_p and rTEC is close to the cubic function. Due to this result in the Taylor series only the contribution of first four terms are included. Then the most probable values of the coefficients: α_{is}, α_{il}, β_i, γ_i, T_s and T_l from (15) have to be determined. This is a nonlinear optimizing task that can be solved by applying the "trial-and-error" method in a way that the best approximation in a sense of minimum least squares deviation to be assured. In order to solve the problem the following steps are made: (i) it is given a range of T_s changes from 0 to 10 hours with a time resolution of 1 hour and a range of T_l changes from 11 to 72 hours with a time resolution also of 1 hour; (ii) for each point of the built in this way grid the coefficients α_{is}, α_{il}, β_l and γ_i are found by using the method of least squares best fit, and (iii) the coefficients α_{is}, α_{il}, β_i, γ_i, T_s and T_l at which the best approximation (in a sense of minimum least squares deviation) is obtained are accepted as optimal coefficients for the model rTEC described by (16).

In the present study we accepted: (i) longitude and UT as independent variable quantities; the conversion to LT is a simple procedure, and (ii) at each modip latitude a separate model, described by (5), is constructed; the values of the model rTEC which do not belong to the 5° modip grid are obtained by an interpolation procedure that will be described later. The latter is done because if a latitudinal approximation is used first the number of model constants will increase and second an additional error will be introduced. The rTEC model described by (16) contains 820 constants and they are determined by least squares fitting techniques.
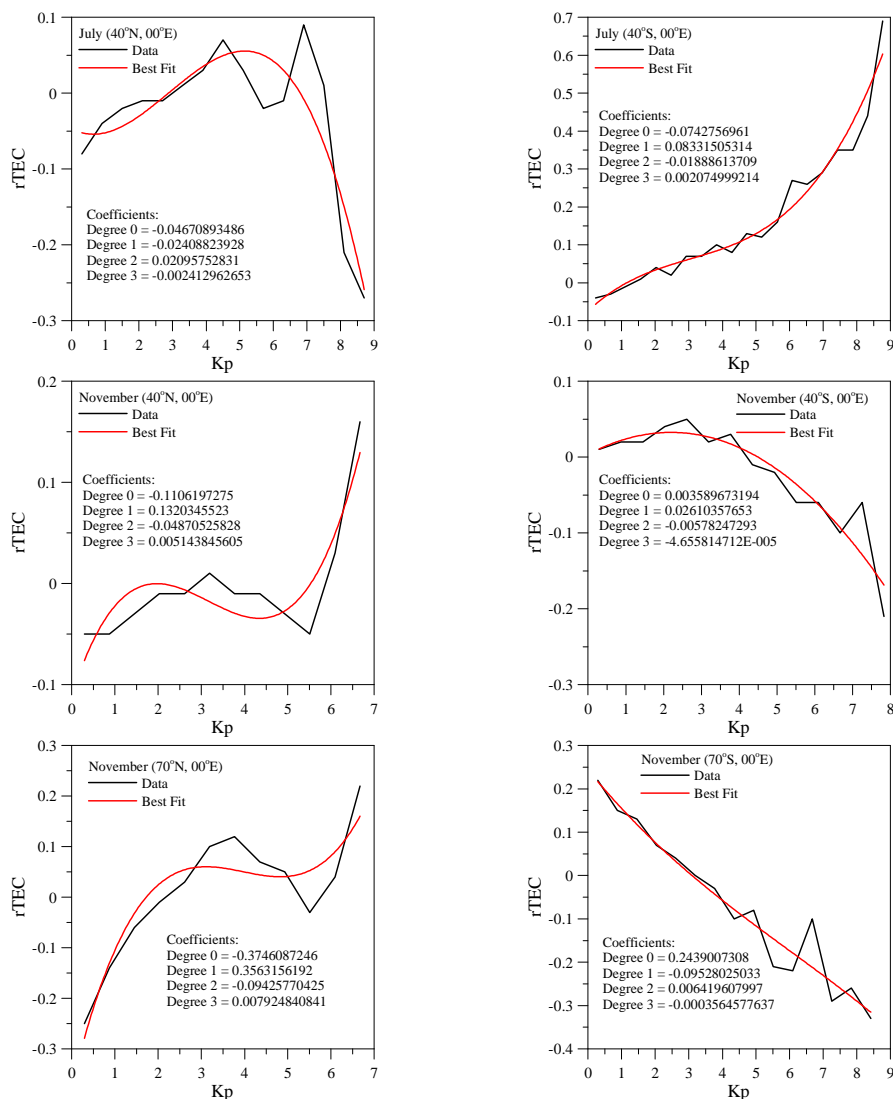
Figure 20 The empirical dependence between the K_p and rTEC calculated for different months and geographical points noted at the plots.

3.3 rTEC Model Results

In order to demonstrate how the model is able to describe the rTEC response to geomagnetic activity two geomagnetic storms observed at different seasons and solar activity conditions will be presented.
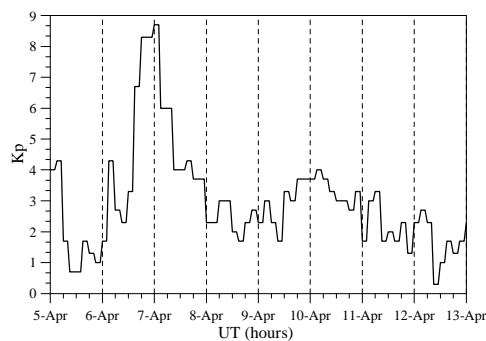
Figure 21a Temporal variability of the Kp-index during the geomagnetic storm in April 5-13, 2000.
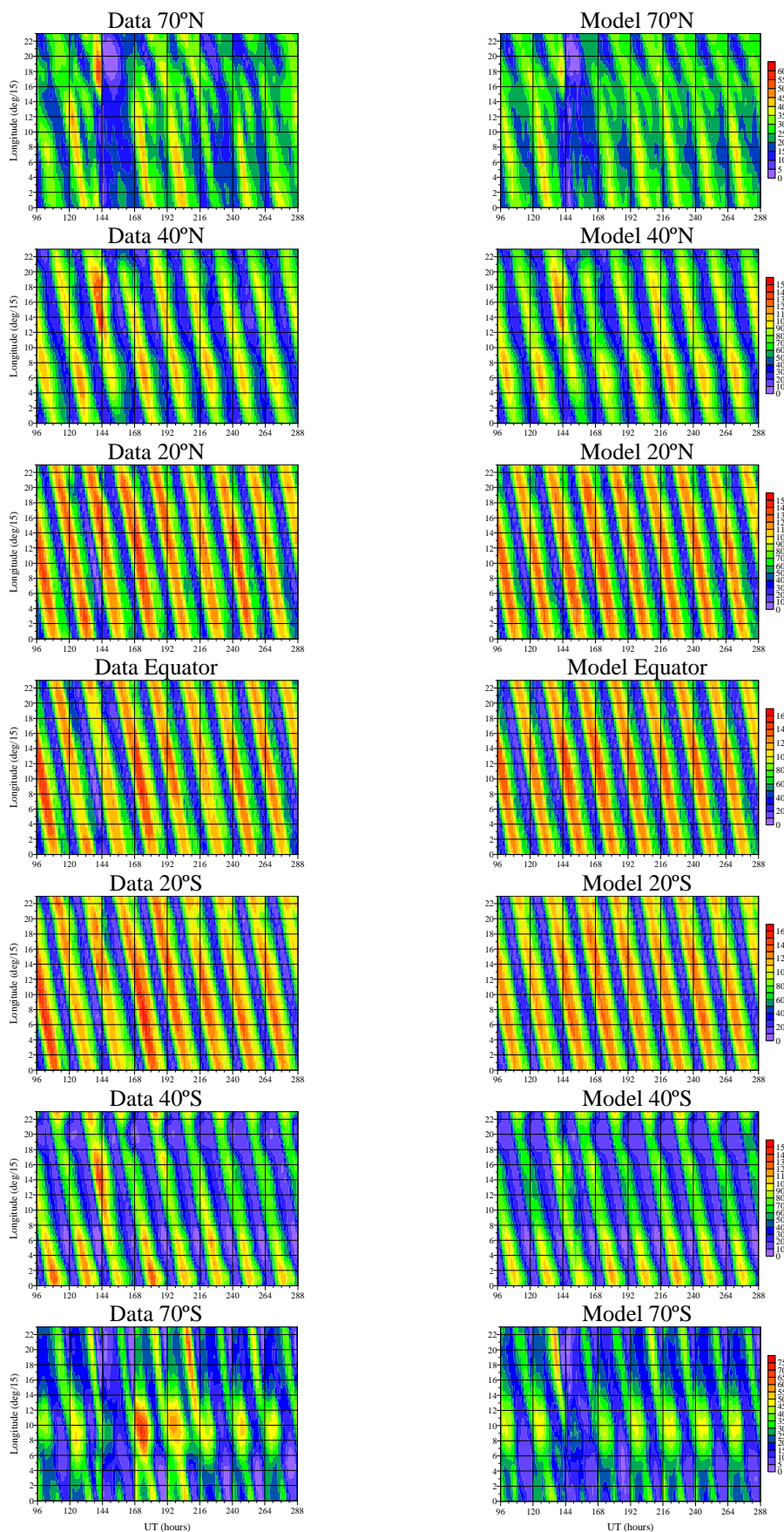
Figure 6b Comparison between the model (right column of plots) and observed (left column of plots) rTEC longitude-hour cross-sections for the considered geomagnetic storm at different modip latitudes noted above the plots.
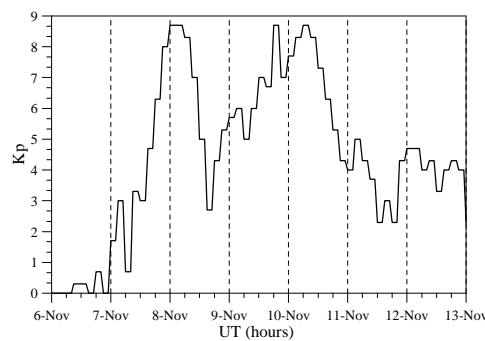
Figure 21a shows the temporal variability of the Kp-index during the geomagnetic storm in April 5-13, 2000, at high solar activity. The rapid increase of the Kp-index starts at around 12 UT on 6 April and reaches the largest values (close to 9) at midnight and early hours on 7 April; then it decreases to the undisturbed levels. Figure 21b presents the comparison between the model (right column of plots) and observed (left column of plots) rTEC longitude-hour cross-sections for the considered period of time, April 5-13, at different modip latitudes which are noted above the plots. We clarify that the longitude is presented by numbers define from longitude/15° while the time is in hours and it starts on 01 April 2000 at 00 UT. In order to facilitate the comparison between the model and data results the color scales are the same at the same modip latitudes. However as the rTEC response strongly depends on the modip latitude the color scales are different at different modip latitudes. The careful comparison between model and data plots reveals that the model overall well reproduces the real situation. It however underestimates the positive rTEC response at high latitudes in the second half of April 6 at 70°N i.e. almost simultaneously with the largest values of Kp-index and one day later positive response at 70°S. The model quite well reproduces the negative rTEC response in the second half of April 6 at 70°S when Kp-index rapidly increases. At middle latitudes, $\pm$40°, the model positive rTEC response is also slightly underestimated in the second half of April 6. The model rTEC response at tropical and equatorial latitudes comparatively well reproduces the data. It is worth noting that at all modip latitudes the model very well describes the longitude variabilities of the rTEC response. Most probably this is due to the large number of the zonal waves included in the model.


Figure 22a Temporal variability of the Kp-index during the geomagnetic storm in November 6-13, 2004.

Figure 22a presents the temporal variability of the Kp-index during the geomagnetic storm in November 6-13, 2004, i.e. during the declining phase of the solar cycle. This is more complex geomagnetic storm with two Kp-index amplifications which are far from each other of about two days. Figure 22b presents the comparison between the model (right column of plots) and observed (left column of plots) rTEC longitude-hour cross-sections for the period of time, November 6-13, again at different modip latitudes arranged in the same way as those in Figure 21b. In this case the rTEC responses to both Kp-index amplifications have to be considered. The model comparatively well reproduces the rTEC response related to the first Kp-index amplification at high latitudes, $\pm$70°, but underestimate that connected with the second Kp-index amplification. The temporal and longitudinal variability of the rTEC response at middle latitudes, $\pm$40°, is very well recreated; only the positive rTEC response on November 8 is slightly underestimated. Some slight underestimation of the rTEC response can be also distinguished at tropical and equatorial latitudes.

The above shown examples of two geomagnetic storms clearly indicate that the global empirical rTEC model describes quite well the ionospheric response to the geomagnetic activity at different solar cycle conditions. Each empirical model needs to be statistically evaluated. The main statistics based on the entire data set are presented here through the mean (systematic) error (*ME*), root mean squares error (*RMSE*) and the standard deviation error (*STDE*) usually accepted as the basic error characteristics of each model. In order to evaluate the main statistics of the model first the model TEC, where $TEC_{mod} = TEC_{med}(1+rTEC)$, i.e. this is a corrected 15-day median TEC with the model rTEC, is calculated. The following errors for the considered period of time (1 January 1999-31
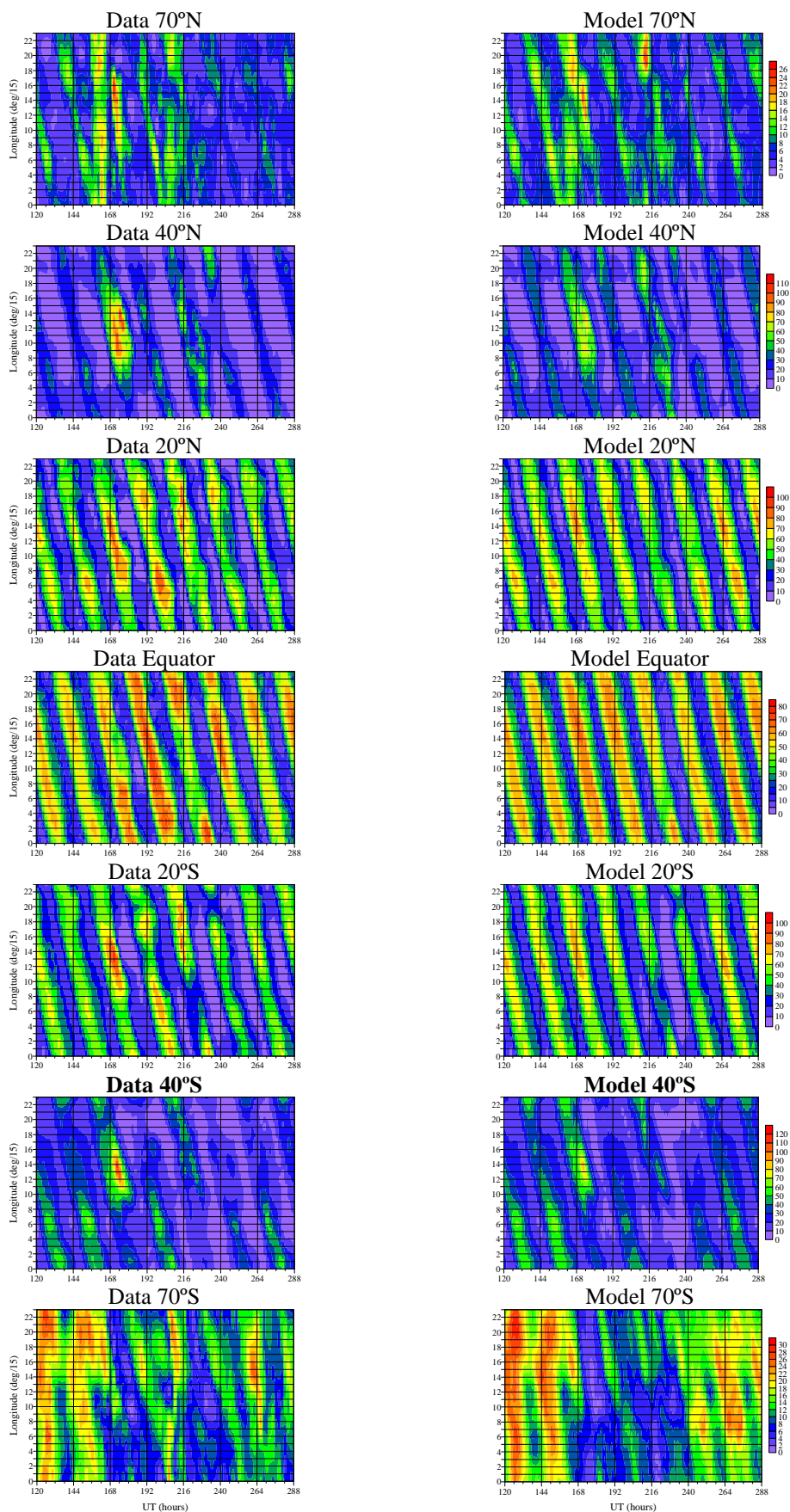
Figure 22b Comparison between the model (right column of plots) and observed (left column of plots) rTEC longitude-hour cross-sections for the considered geomagnetic storm at different modip latitudes noted above the plots.

December 2011) are obtained: *ME*=-0.204 TECU, i.e. the model fits to the CODE TEC data with small negative bias; then the *RMSE* and *STDE* have very close values, i.e. *RMSE*=4.592 and *STDE*=4.588.

The overall statistics of the model error can be defined more precisely by showing the dependence of *RMSE* on modip latitude and months. Figure 23 shows a modip latitude-month cross-section of the model *RMSE* calculated for the entire (January 1999 – December 2011) period of time. The largest *RMSE*, reaching 7.5 TECU, are observed at low latitudes where the equatorial ionospheric anomaly is developed; the crests are situated at around ±30° modip latitude. Some amplification of the *RMSE* can be noticed also around 70°S during the equinoxes; it reaches around 4 TECU. The largest errors are found mainly in the equinoxes and this could be due to both semiannual variability of the ionosphere and semiannual variability of the geomagnetic activity. We calculated also the *RMSE* for each month of the entire time interval (not shown result); as it is expected in advance the *RMSE* has larger values during high solar activity.
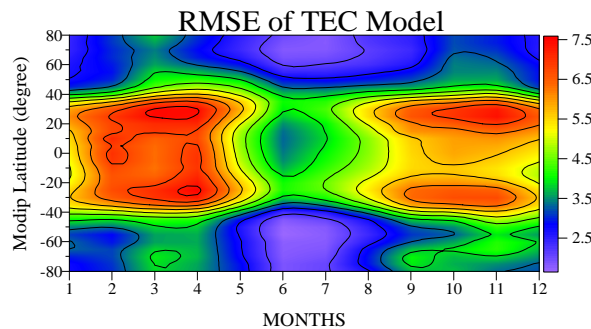

Figure 23 Modip latitude-month cross-section of the model *RMSE* calculated for the entire (January 1999 – December 2011) time interval.

3.4 Global TEC Maps

The basic aim of each global TEC model used for short-term prediction is to construct the global distribution of the TEC, i.e. to obtain global TEC maps, at given geomagnetic activity, day of the year and UT. The presented here rTEC model predicts the correction to the 15-day median values for each hour of the prediction period. The TEC value at a given hour is actually a corrected 15-day median TEC with the model rTEC. Then the TEC maps are constructed by interpolation of the TEC values from the used grid with a 5° step in modip latitude and 15° in longitude. The interpolation between obtained TEC values is done again by using Inverse Distance Method (Shepard, D., 1968). Then the modip frame is converted to geographical one. The TEC values assigned to both poles are found by interpolation between the known from the model points which have the highest northern and southern latitudes. The model maps are arrayed in terms of the coordinate system of geographical latitude from -90° to 90° at each 5° and longitude from -180° to 180° at each 5°.

Figure 24 presents a comparison between the model (right column of plot) and CODE TEC maps for November 8, 2004 geomagnetic storm at 00UT (upper row of plots), 06UT (second row of plots), 12UT (third row of plots) and 18UT (bottom row of plots). In order to facilitate the comparison the color scales at each pair of TEC maps (at one and the same UT) are the same. Due to the dependence of the TEC on the UT the color scales are not the same at different UT. In general there is significant similarity between the CODE and model TEC maps but there are differences as well. At 00 UT and 06 UT for example, the equatorial anomaly is underestimated by the model but the hemispheric asymmetry is quite well reproduced. At 12 UT and 18 UT the model densest part of the ionosphere is closer to the observations; some longitude structures, as for example the Weddell Sea Anomaly in the SH at 18 UT, can be reproduced well.
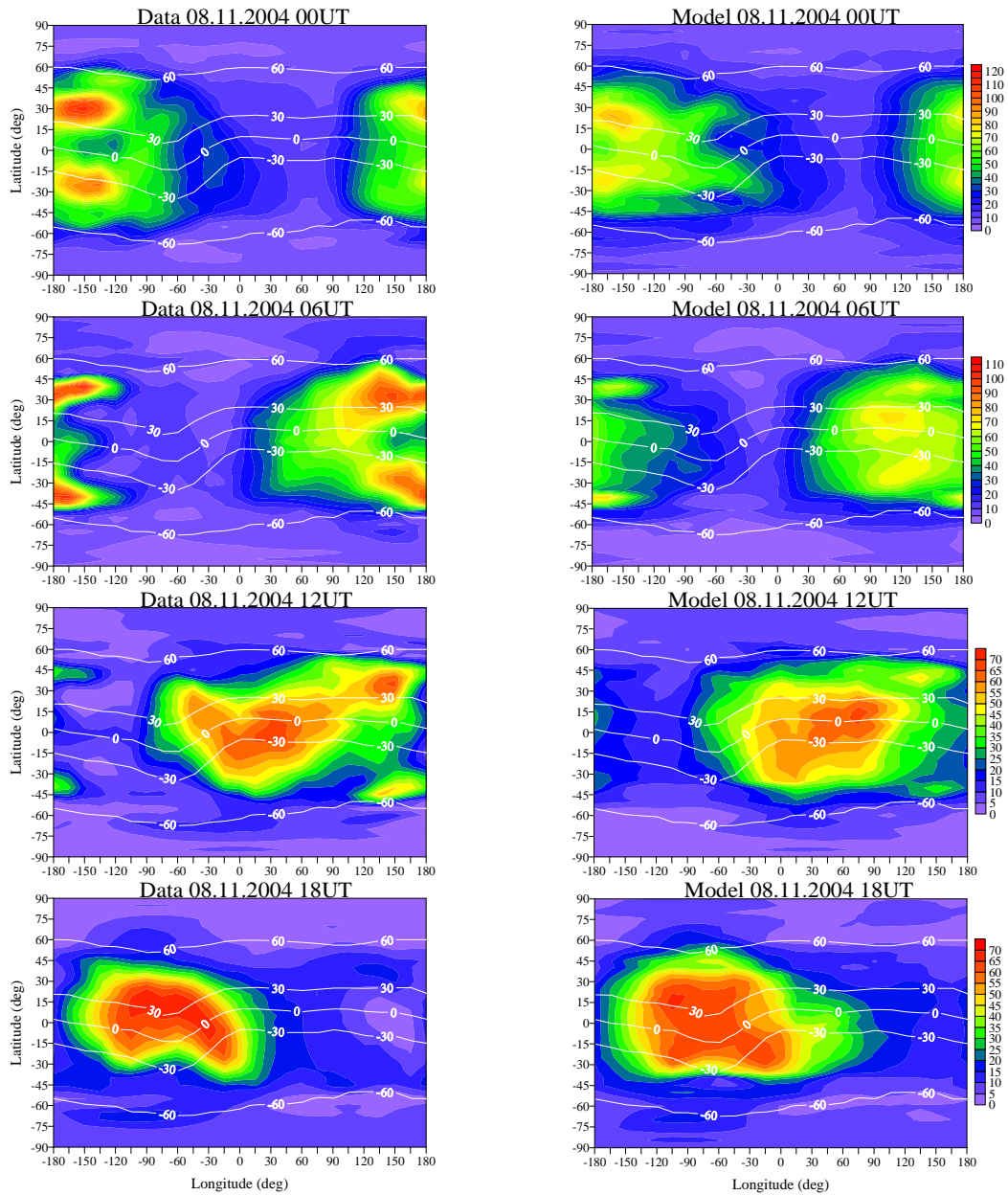
Figure 24 Comparison between the model (right column of plot) and CODE TEC maps for November 8, 2004 geomagnetic storm at 00UT (upper row of plots), 06UT (second row of plots), 12UT (third row of plots) and 18UT (bottom row of plots). The modip latitude is also marked by white line.

The above presented comparison between the model and CODE TEC maps revealed good similarity. This means that the constructed global rTEC model response to the geomagnetic activity can be successfully used for short-term (24 hours ahead) prediction.

3.5 Concluding comments and on-line implementation of the global model of TEC response to geomagnetic activity

Section 3 presented a global empirical TEC model response to geomagnetic activity described by the Kp-index (Mukhtarov et al., 2013c). It describes the geomagnetically forced changes of the TEC assuming that these changes at a given modip latitude depend mainly on Kp-index, LT and longitude. The geomagnetic changes are expressed by the relative deviation of TEC from its 15-day median, noted as rTEC. Therefore this model predicts the correction to the 15-day median values, rTEC, for each hour of the prediction period. The model offers TEC maps which depend on

geographic coordinates (5^ox5^o in latitude and longitude) and UT at given geomagnetic activity and day of the year.

The rTEC model contains 820 constants and they are determined by least squares fitting techniques. The comparison between the model and CODE TEC data at different solar cycle and season conditions demonstrated high degree of similarity. The very small systematic error (-0.204) and low *RMSE* (4.592 TECU) of the model characterized it as useful tool for describing the ionospheric TEC response to geomagnetic storms.

This model can be used for short-term prediction. For this purpose at a given day of the year, geographic location and UT the model needs as input parameter only the predicted Kp-index. This is a possible task because there are available models which predict the geomagnetic activity with a reliable accuracy. An example of such model is a MAK model described by Andonov et al. (2004). It provides online prediction of the K_p-index and is implemented on the web site: http://www.geophys.bas.bg/kp_for/kp_mod_bg.php.
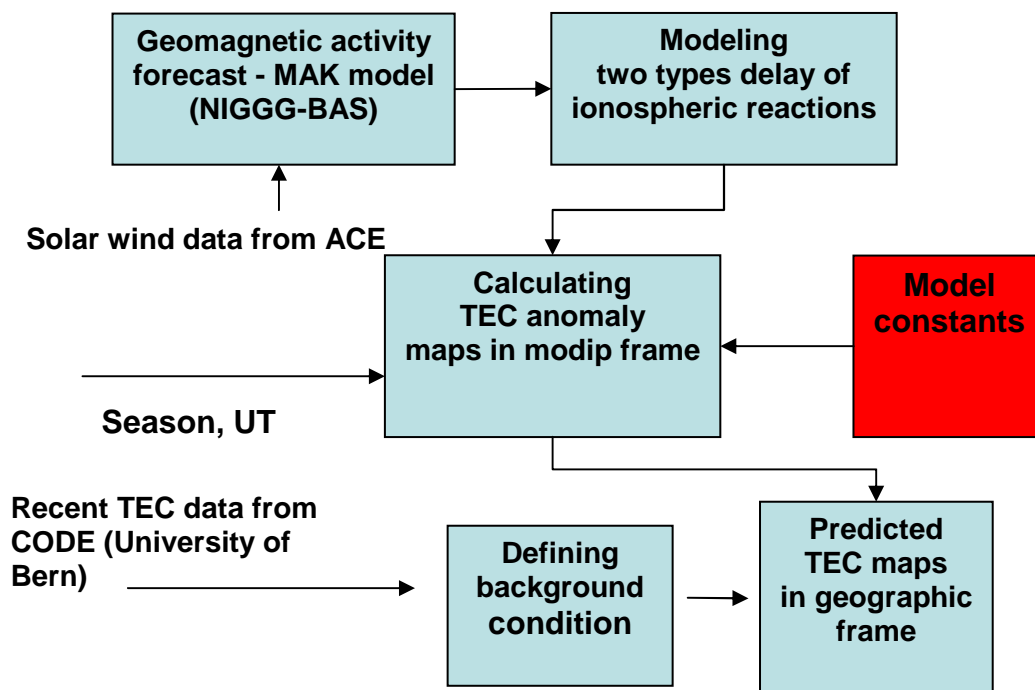
Building of the model
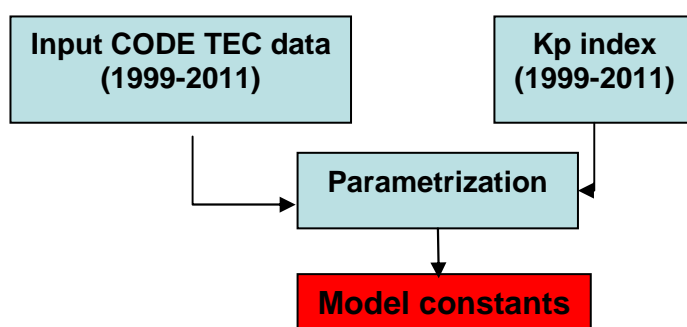
**Figure 25** The block chart of the global TEC model for short-time prediction

The online software of the model has been already implemented on the website (http://www.geophys.bas.bg/tec/page/tec_hourly_en.htm) and it is also still in testing mode. Figure 25 shows its block-chart. It will be officially implemented at the institute website when the paper Mukhtarov et al. (2013c) is published. The short-term TEC prediction particularly at strong geomagnetic storms will improve significantly the accuracy of the geodetic and navigation data which have increasing importance in resolving both scientific and practical tasks.

4. On-line demonstration of the TEC model results

The two TEC models have been officially implemented at the institute website since October 2013 when all three papers devoted to them were published in *J. Geophys. Res. - Space Physics*. They can be found at: http://www.geophys.bas.bg/tec/page/tec.html. At this web side besides the short-term (24 hours ahead) and long-term (a month ahead) prediction TEC maps produced by the TEC model response to geomagnetic activity and the background TEC model respectively there are also two example TEC maps, showing as a movie, demonstrating the strong sides of both models. The hourly median TEC maps for January 01, 2012 are shown where the development of the Weddell Sea Anomaly is clearly reproduced by the background TEC model. The geomagnetically forced TEC anomalies, expressed by the relative deviation of TEC from its 15-day median (*rTEC*) for October 29 - November 01, 2003 demonstrate the global TEC response to the famous Halloween geomagnetic storm. A detailed comparison between the data and model can be seen by a link there.

It has been already mentioned that the TEC model for short-term prediction needs as input parameter only the predicted Kp-index. In our case it is taken from the MAK model (Andonov et al., 2004), which provides online prediction of the K_p-index for the next six hours from the current time. Figure 26 shows how the MAK model works at the web site and how one of the last geomagnetic storm, 19 February 2014, is described there.
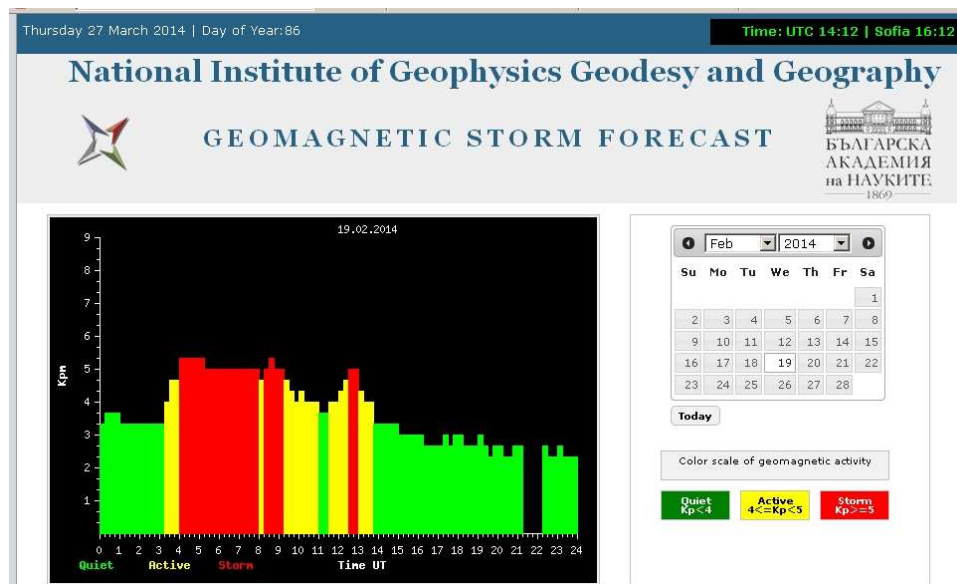
Figure 26 Geomagnetic Kp-index forecast based on the MAK model.

The strongest geomagnetic storm during the last 20 years is the Halloween one, 29-31 October 2003. The website presents both hourly maps of the models and those of the CODE data for the period of time 29 October-01 November 2003 when the geomagnetic storm takes place. Two types of maps are shown on the web site: rTEC and TEC. Figure 27 presents the comparison between the rTEC and TEC maps on 30 October 2003 at 22 UT (when the second Kp-index peak is seen) produced by the CODE data (left plot) and model results (right plot).
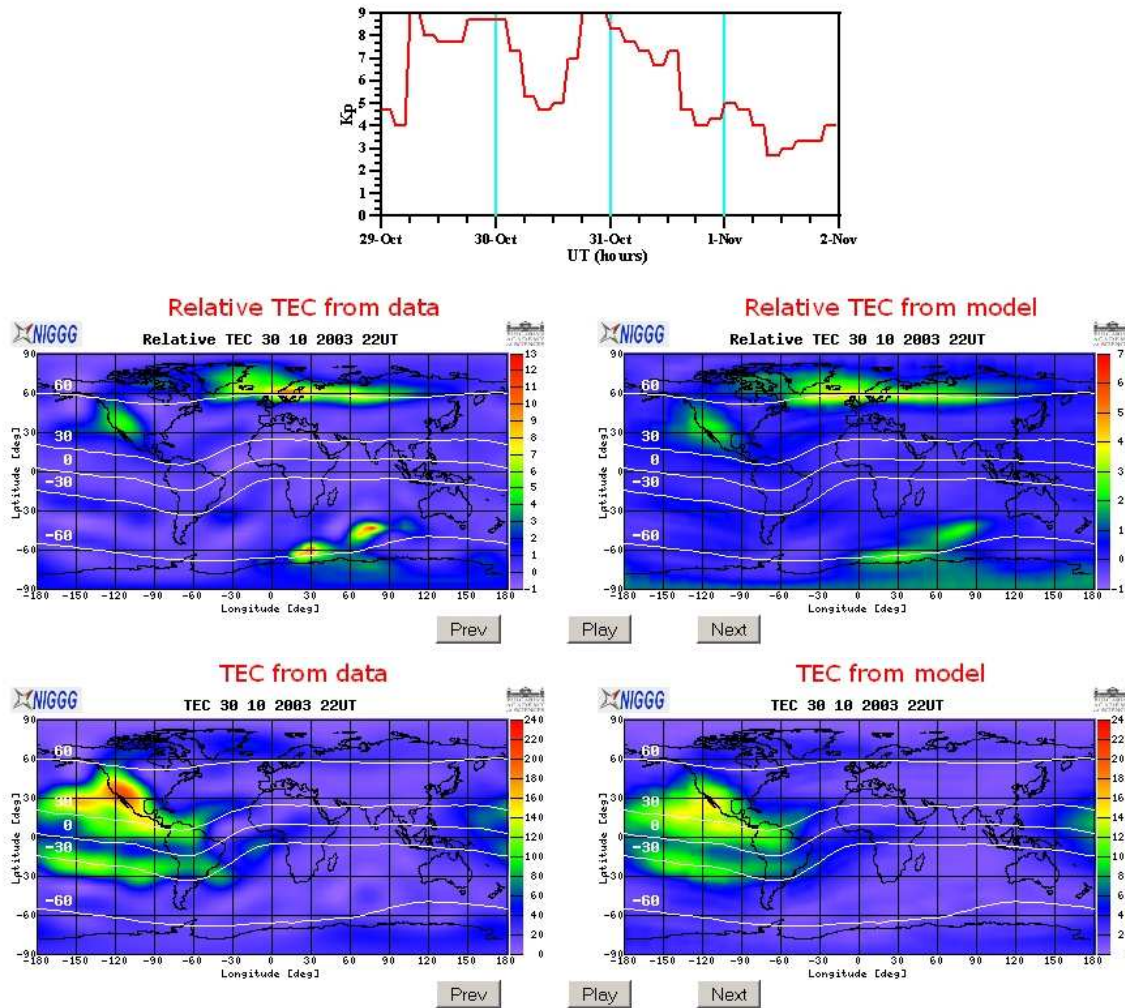
Figure 27 (upper plot) The Kp-index for 29 Oct-01 Nov 2003; comparison between the rTEC (upper row) and TEC maps (bottom row) between the CODE data (left column) and model results (right column).

The careful inspection of the two couples of maps shows a high degree of similarity; the model reacts to both positive and negative TEC anomalies. This indicates that the TEC model response to geomagnetic activity captures very well all: LT, modip latitude/longitude and seasonal dependences of the TEC response to strong geomagnetic storms like the Halloween one. The quantitative comparison however shows some underestimation of the magnitude of the TEC anomalies. Of course, this is a consequence of the fact that all empirical models predict an average response based on the data used for constructing the model. We have carefully assessed the ability of the model to reproduce and predict the TEC response at different conditions. It has been found that the model is able to capture well the TEC response even to moderate and minor geomagnetic storms when however the solar radio flux variability is low, or particularly when the ~27-day (~13.5-day also) oscillations are absent. This is related to the fact that the model predicts the correction to the 15-day median values, but these 15-day medians significantly suppress such oscillations.

Figure 28 presents an example of how the web site for both TEC models looks like for 26 March 2014. After the representation of the Weddell Sea Anomaly (upper left plot) and rTEC maps for Halloween geomagnetic storm (upper right plot), which demonstrate the ability of both models to reproduce different ionospheric events, then the short-term (for 27 March, middle plot) and long-term (for 26 April, bottom plot) prediction TEC maps are shown.

National Institute of Geophysics, Geodesy and Geography

Global empirical TEC models based on the CODE TEC data

The ionospheric total electron content (TEC) is a key parameter for describing the impact of the ionosphere on the propagation of radio signals. Understanding the variability of TEC is crucial for the operation of many applications, as navigation satellite systems like Global Positioning System (GPS), Global Navigation Satellite System (GLONASS), and the future Galileo system.
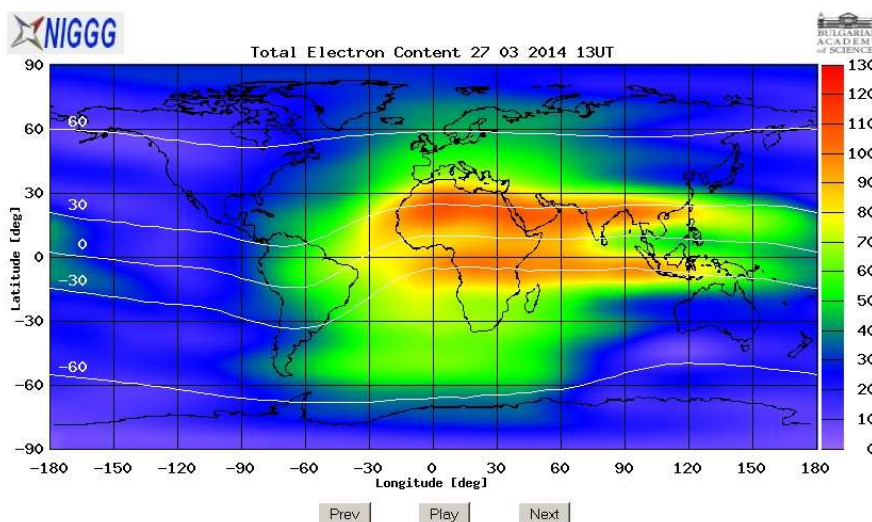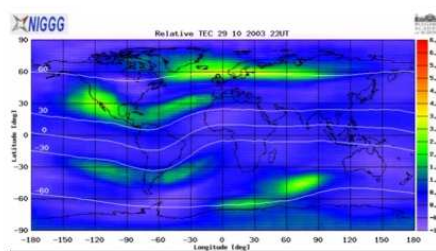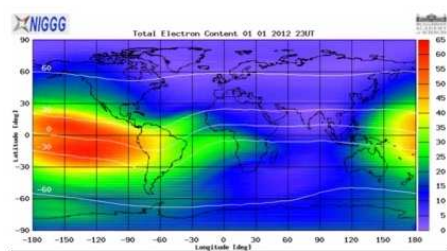
Two global empirical TEC models are built by using the Center for Orbit Determination of Europe (CODE) TEC data (ftp://ftp.unibe.ch/aiub/CODE/) for full 13 years, 1999-2011. The background TEC model (for details see the two PDF files, [PDF1], [PDF2]) offers 31-day running median TEC maps for a month ahead at a given UT. The TEC model response to geomagnetic activity (for details see the PDF file) presents a current and 24 hours ahead TEC maps.

The work on the TEC models was supported by the European Office of Aerospace Research and Development (EOARD), Air Force Office of Scientific Research, Air Force Material Command, USAF, under grant number FA8655-12-1-2057 to D. Pancheva (for contact).

1. Global empirical background TEC model	2. Global empirical model of TEC response to geomagnetic activity
The hourly median TEC maps for January 01, 2012 are shown where the development of the Weddell Sea Anomaly can be clearly reproduced by the background TEC model.	The geomagnetically forced TEC anomalies, expressed by the relative deviation of TEC from its 15-day median (rTEC) for October 29 - November 01, 2003 demonstrate the global TEC response to the famous Halloween geomagnetic storm. A detailed comparison between the data and model see HERE

See more...   See more...

Prev   Play   Next

Back

Prev   Play   Next
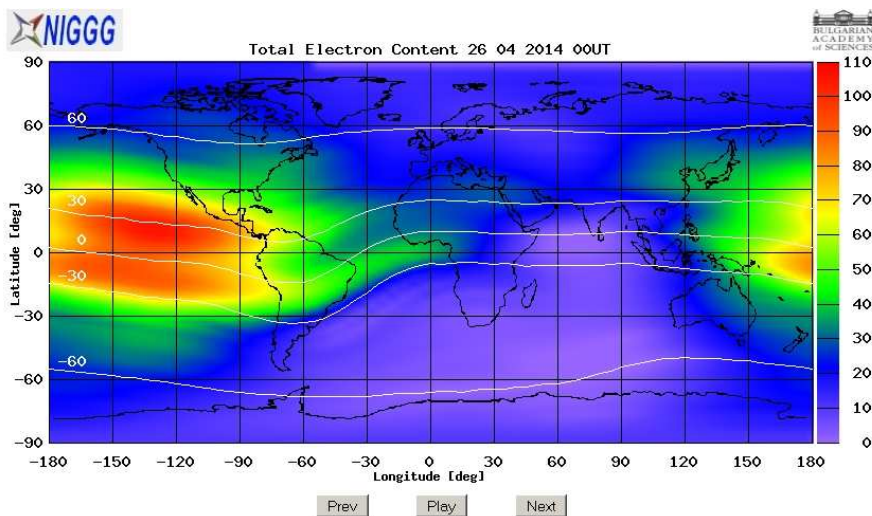
Back

Figure 28 Global empirical TEC models based on the CODE TEC data

Very recently a mobile version of both TEC models have been implemented and now the TEC model predictions have be seen by using tablets or smart phones. This was done in order to support advertizing the models.

5. An attempt to mitigate the global background TEC model's error by using regularly arriving new TEC data – a hybrid TEC model

The attempt for improving the quality of the long-term TEC forecast is based on the regularly arriving fresh CODE TEC data and the autocorrelation prediction of the error and the respective correction of the background model with the predicted error. Because this approach needs fresh data, i.e. new data which have not been used for constructing the model, it is called a hybrid method. The CODE TEC data, used for constructing the background TEC model, arrive daily with a delay of a few days toward the current date. As this model predicts the 31-day running median TEC values then reliable (measured) TEC data for a past period are available only for about 15 days from the date at which the prediction is made. If the time distance between the dates for which the prediction is made to that for which the reliable data for calculating the 31-day running median TEC value are available is denoted as *offset*, then the offset will be equal or larger than 15 days as it is composed by number of days between the current date and the date for which the prediction is made plus 15 days before the current date.

The suggested method will be demonstrated on the archival data. The main idea is based on the assumption that the time series of the model residuals are not composed only of random component but have also some time dependent component. Figure 29 shows the temporal variability of the model residuals calculated for points with longitude of 00°E and modip latitudes of 40°N (upper plot), 00° (middle plot), and 40°S (bottom plot) for 00 LT. The careful inspection of the plots reveals that the model residuals are correlated, i.e. each value is related to the neighbour ones. This circumstance provides an opportunity for predicting the model residuals in future moments on the base of the actual residuals in the past which are determined by comparison of the model values with the observations. The determination of the predicted residuals could provide a possibility for correcting the model values for some future moments.
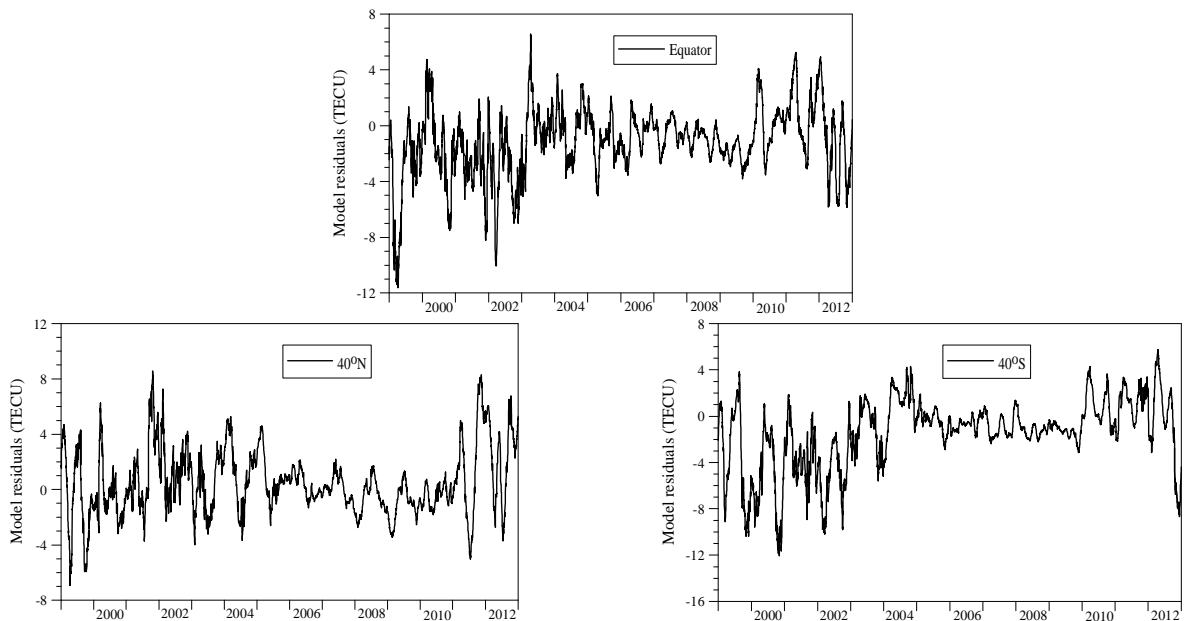
Figure 29 Temporal variability of the model residuals calculated for points with longitude of 00° and modip latitudes of 00° (upper plot), 40°N (left plot) and 40°S (right plot) for 00 LT.

The autocorrelation method for forecasting the error is based on the well-known theorem of Wiener–Hopf. For a stationary random process $x(t)$, for which the mathematical expectation, variance and autocorrelation function are known quantities then an unknown value of the process $x(t)$ at future moment t_f can be represented at minimum squares deviation as a linear combination of some sample of known values of the process $x(t)$ at the moments: t_1, t_2, ..., t_n. Then:

$$x(t_f) = \bar{x} + \sum_{i=1}^{n} \beta_i (x(t_i) - \bar{x}) \tag{17}$$

The coefficients β_i from (3) are a solution of the system of equations:

$$\sum_{p=1}^{n} \beta_p \rho(t_k - t_p) = \rho(t_f - t_k) \qquad k = 1,2,...,n \tag{18}$$

The normalized (by dispersion) autocorrelation function of the process $x(t)$, denoted by ρ, is present in the system of equations (18) and it is a function of time lag. The right part of the system of equations (18) contains the autocorrelations at time lags between the moment for prediction and the moments where there are known values. Hence the deviation of the prediction from the observations, based on this method, depends on the values of the autocorrelation coefficients at time lags corresponding to the distances between the moment for prediction and the moments for which the values of the process $x(t)$ ate known.

The simulations of the autocorrelation correction of the model's error will be demonstrated on the TEC data for the time period 2007-2012. The autocorrelation function of the deviations (residuals or errors) is calculated by using the model residuals for the period of time 1999-2006.
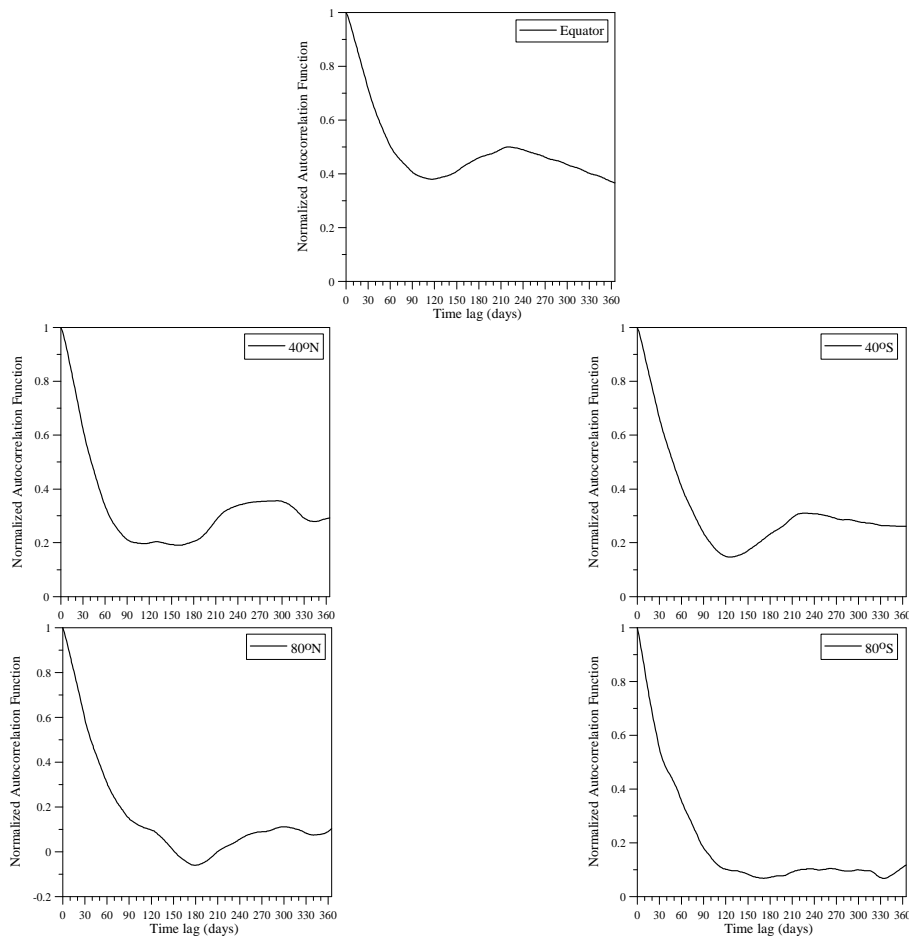

Figure 30 Normalized autocorrelation functions calculated for equator (uppermost plot) and at modip latitudes of: 40°N (left upper plot); 40°S (right upper plot); 80°N (left bottom plot) and 80°S (right bottom plot).

Figure 30 shows the normalized autocorrelation functions calculated for equator (uppermost plot) and at modip latitudes of: 40°N (left upper plot); 40°S (right upper plot); 80°N (left bottom plot) and 80°S (right bottom plot). The inspection of the autocorrelation functions reveals that a higher correlation of the model residuals is observed at lower modip latitudes than those at high modip latitudes. Values of the correlation coefficients around and above 0.5 are seen at time lags up to 60 days, i.e. an effective correction of the error is possible to occur if the offset is not more than two months.

The next step is to check how the length of the offset affects the correction approach. The validation procedure is done at offsets of 15, 30, 45, 60, 75 and 90 days. It actually presents a simulation of the predicted error in real conditions. The correction of the global background TEC values by the autocorrelation method for error prediction is demonstrated in Figure 31. It shows a comparison between the observed TEC (thin solid line), not corrected model TEC (thick solid line) and corrected model TEC (dashed line) at offsets of: 15 days (left upper plot), 30 days (right upper plot), 45 days (left bottom plot) and 60 days (right bottom plot) calculated for 30°N and 0°E at 12 UT. It is seen that if the offset is 15 days (i.e. to predict the error at the current day) the corrected model
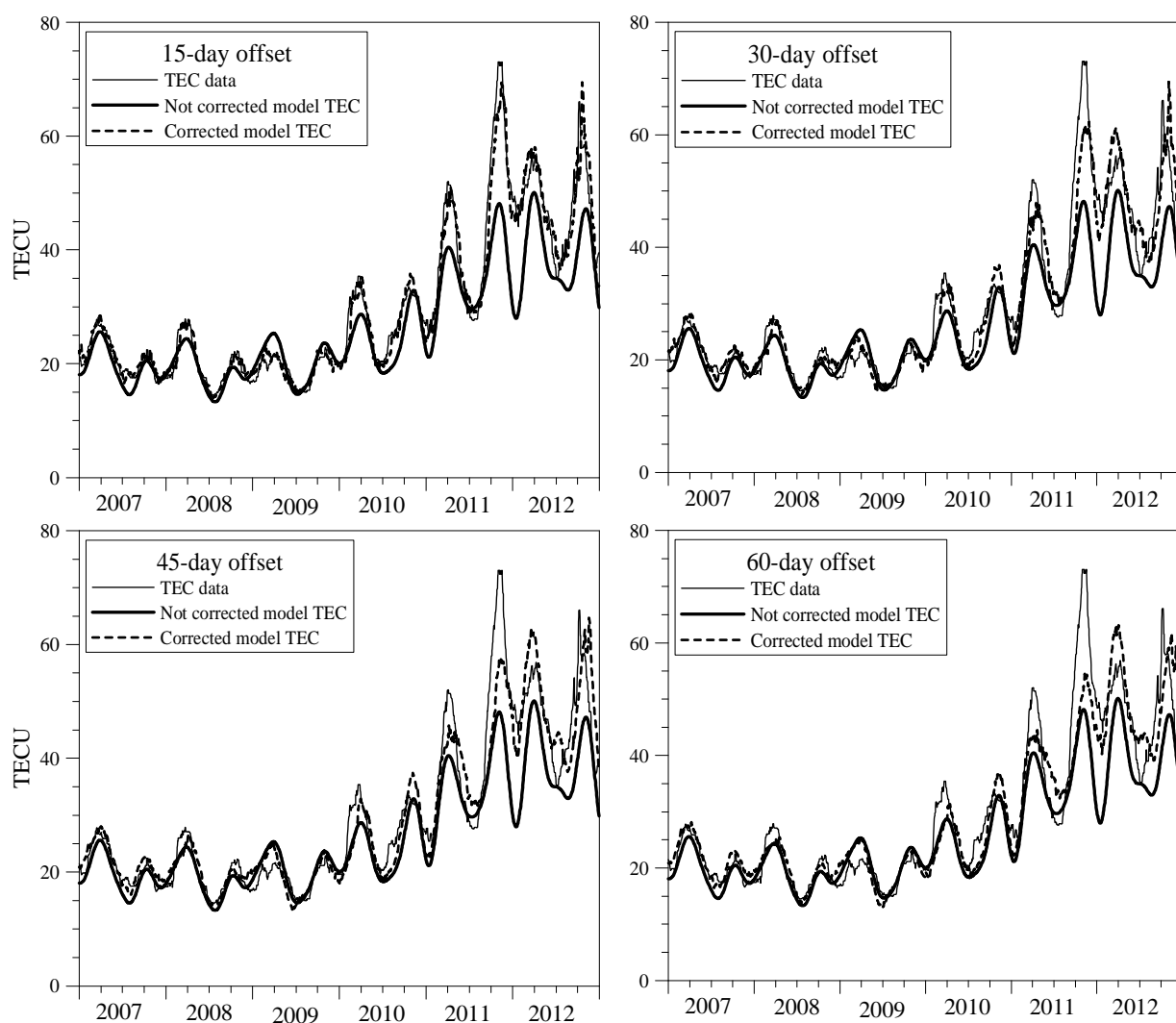

Figure 31 Comparison between the observed TEC data (thin solid line), not corrected model TEC (thick solid line) and corrected model TEC (dashed line) at offsets of: 15 days (left upper plot), 30 days (right upper plot), 45 days (left bottom plot) and 60 days (right bottom plot) calculated for 30°N and 0°E at 12 UT.

TEC almost coincides with the TEC data. With increasing the offset the difference between the corrected model TEC and the TEC data increases as the corrected model TEC values approach to values of the not corrected ones. The presented in Figure 31 examples clearly demonstrate the efficiency of the correction depending on the given offset.

The advantage of the hybrid model for long-term prediction with respect to the built by Mukhtarov et al. (2013a) background TEC model is illustrated by comparing of their *RMSE*. Figure 32 shows the comparison between the *RMSE* of the background TEC model (thick solid line) and that of the corrected TEC model (thin solid line with symbols) calculated for different offsets for the period of time 2007-2012. The found dependence of the *RMSE* on the offset support the earlier suggestion that the correction is really effective if the error prediction is made for a date with a distance up to 60 days from the date with real data. If we consider real conditions a prediction of a month ahead means that the offset is 45 days. In this case, the *RMSE* decreases from 3.2 TECU to 2.76 TECU. If we make a prediction for the current month then the offset is 15 days and the *RMSE* falls down to 1.52 TECU.
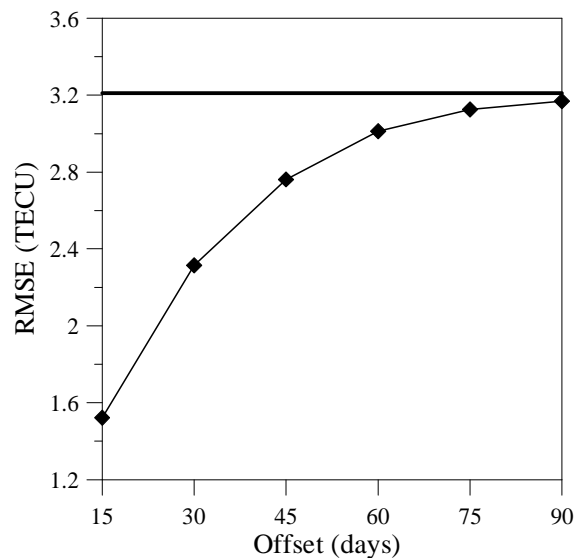
Figure 32 Comparison between the *RMSE* of the not corrected background TEC model (thick solid line) and corrected global TEC model (thin solid line with symbols) calculated for different offsets for the period for time 2007-2012.

The procedure for the correction of the model residuals is fully applicable to the real prediction of the global median TEC. When it is necessary to make TEC prediction for a date with large offset then the effectiveness of the correction asymptotically approaches to zero. This is due to the fact that that the right side of the system of equations (18) is inclined to zero and then the coefficients β_i from (17) become zero. If this happens however the quality of the median global TEC prediction does not get worse. The presented in this part a hybrid method is described in detail by Mukhtarov et al. (2014).

In conclusion it is worth noting that the hybrid model is fully applicable to the real prediction of the global median TEC. The hybrid model however is not an autonomous ionospheric TEC model and due to this it is not useful for numerous single frequency GPS applications that need additional information (as an autonomous ionospheric TEC model) for mitigating the ionospheric propagation error.

6. An attempt to assess the stratospheric impact on the TEC variability in winter

The last task proposed to be investigated in this project is related to the ionospheric response to anomalous atmospheric phenomena, like sudden stratospheric warming (SSW) events (Pancheva

and Mukhtarov, 2011b; Jin et al., 2013) that has been recently obtained. This finding has directed the attention of the researchers to the relationship between the TEC and stratospheric meteorological field (as temperature, geopotential height, neutral wind etc.) variabilities. Due to this the next step is to conduct a detailed research on this ionosphere-atmosphere relationship, particularly strong in winter, and to present an idea about a TEC model where the stratospheric impact is included. As the stratospheric meteorological fields are predicted with a few days ahead it is worth making an attempt to add also the stratospheric effect on the TEC variability in a model for short-time TEC prediction. We expect that some improvement of the TEC model, particularly during the SSW events, could be possible. In this part we will present only some research results that later could be incorporated for improving the global TEC model for short-term prediction.

The numerical simulations performed by Liu and Roble (2002) for the first time reported that the stratospheric warming is associated with the lower thermospheric warmings. Later this result was supported by the satellite measurements of the MIPAS/Envisat which indicated that the high latitude thermosphere between 120 and 140 km is really warmer during the major SSW in January 2009 (Funke et al., 2010). The temperature changes in the lower thermosphere, i.e. in the dynamo region, lead however to wind changes which through dynamo effect could have impact on the ionospheric plasma redistributions. This simple physical relationship was used by Pancheva and Mukhtarov (2011b) who for the first time reported a significant decrease of both mean electron density and the amplitude of the diurnal migrating component in the low latitude ionosphere during the major SSW in January 2009. To explain the observations seen in the satellite FORMOSAT-3/COSMIC electron density the author suggested a mechanism analogous to the so called ''disturbed dynamo'', but generated by the SSW event not by geomagnetic storms. Later the validity of this mechanism was supported by numerical simulations with the GSM TIP model reported by Klimenko et al. (2012).

The above results directed our attention to the temperature as a meteorological parameter that has to be used for searching correlation with the ionospheric TEC. For this purpose the satellite MLS-Aura temperature measurements and the CODE TEC data have been used. Before calculating the cross-correlation functions the seasonal courses were removed. This is done by using 31-day running means which were removed from the original data. The preliminary investigations concerning the choice of the most representative altitude and latitude for the stratospheric temperature revealed that the temperature at the altitude around 40 km and latitude of 60°N describes the most typical winter conditions. Due to this the cross-correlation with the global TEC has been done with this temperature for the boreal winter (October-March). The results are shown in Figure 33.
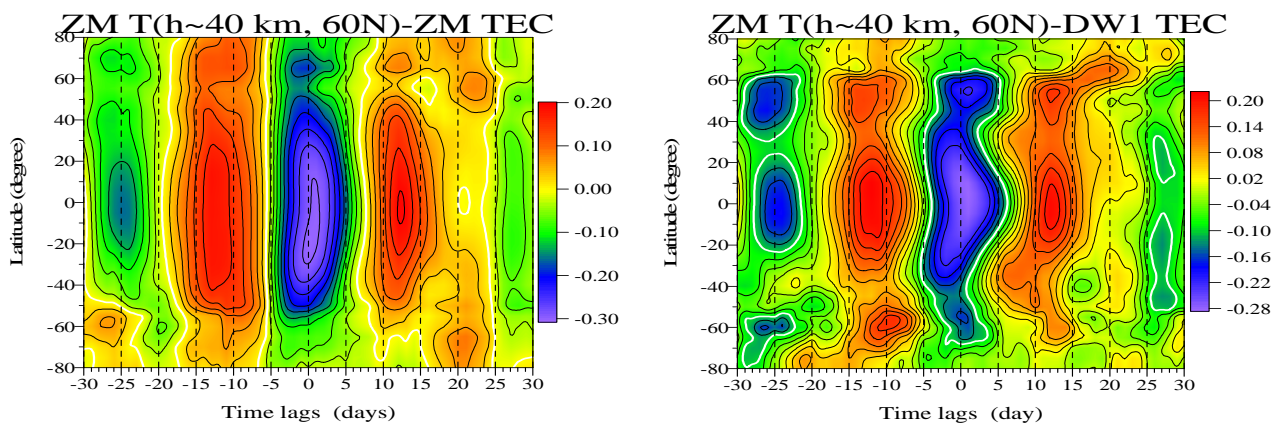
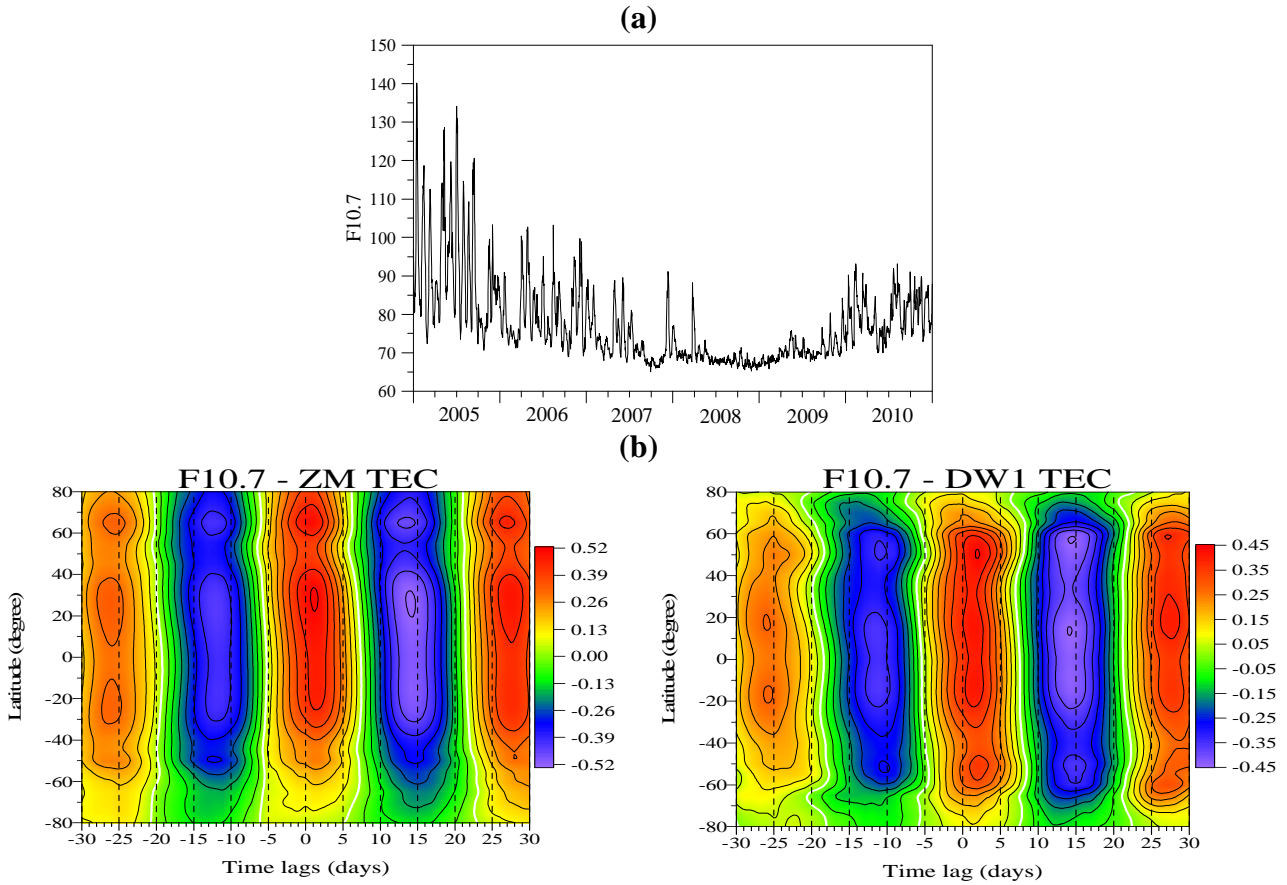**Figure 33** (left plot) Latitude structure of the cross-correlation functions between the ZM TEC and ZM temperature at latitude of 60°N and altitude of ~40 km; the same as the left plot but the cross-correlation is with the DW1 TEC.

The cross-correlation results support the observations reported by Pancheva and Mukhtarov (2011b) and the largest cross-correlation coefficients for ZM TEC and DW1 TEC are respectively -0.30 and

-0.28. According to the "Fisher's Z-transformation" test the obtained coefficients are above 95% confidence level, i.e. they are significant.

The main effect on the ionosphere however has the solar radiation represented by it proxy solar radio flux F10.7. The geomagnetic effect is excluded because we have already built a global TEC model response to geomagnetic activity and because the effect is not linear. Then the basic aim of this study is to find an approximate quantitative relationship between both effects on the ionospheric TEC, i.e. that of stratospheric temperature and F10.7, during period of low and middle solar activity. For this purpose we investigate the period of time 2005-2010. Figure 34 shows F10.7 for the period of time 2005-2010 (upper plot) and the latitude structures of the cross-correlation functions of F10.7 with ZM TEC (left plot) and DW1 TEC (right plot). The cross-correlations indicate the known positive relation between F10.7 and TEC and also the impact of 27-day oscillations.

Figure 34 **(a)** Daily values of F10.7 for the period of time 2005-2010; **(b)** Latitude structure of the cross-correlation functions of F10.7 with ZM TEC (left plot) and DW1 TEC (right plot).

The above obtained cross-correlation results have presented evidences for creating a linear regression TEC model where the impact of the stratospheric temperature at altitude of ~40 km and latitude of 60°N and the day-to-day variability of F10.7 on the main TEC decomposition components, i.e. ZM and DW1, is included. The model can be described by:

$$TEC_{zm}(mlat, day) = \alpha_{ZMTemp}(mlat)T_{60}(day - T_{ZMT}) + \alpha_{ZMSol}(mlat)F107(day - T_{ZMF}) + \alpha_{zm00}$$

$$TEC_{DW}(mlat, day) = \alpha_{DWTemp}(mlat)T_{60}(day - T_{DWT}) + \alpha_{DWSol}(mlat)F107(day - T_{DWF}) + \alpha_{DW00}$$

The regression coefficients and the respective time lags are defined by least squares best fit approach. Figure 35 (a) presents modip latitude dependence of the regression coefficients which describe ZM TEC (left plot) and DW1 TEC (right plot), while (b) shows modip latitude dependence

of the model RMSE (in TECU) calculated for ZM TEC (purple) and DW1 REC (magenta). The results indicated that this model is valid for the tropical region (±30 modip) where the equatorial anomaly is located and where the SSW response found by Pancheva and Mukhtarov (2011b) was the largest.
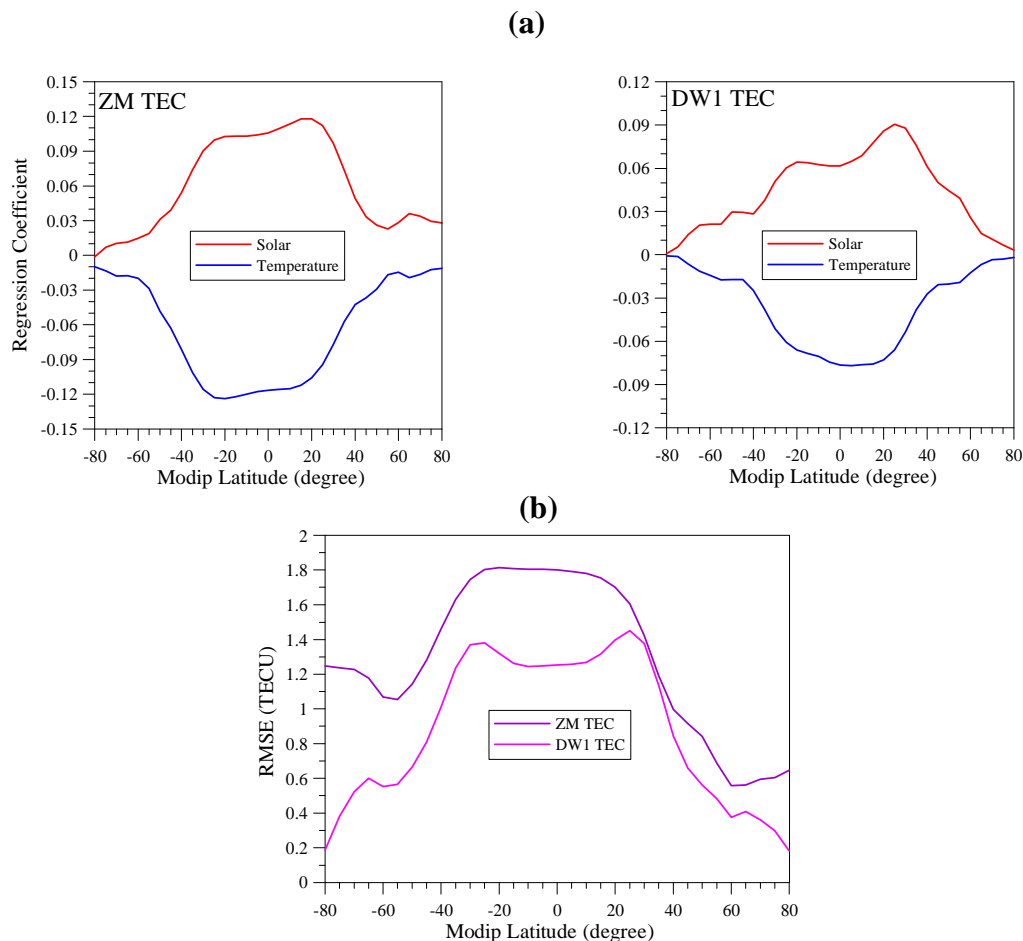
(a)

(b)

Figure 35 (a) Modip latitude dependence of the regression coefficients which describe ZM TEC (left plot) and DW1 TEC (right plot); **(b)** Modip latitude dependence of the model RMSE (in TECU) calculated for ZM TEC (purple) and DW1 REC (magenta).
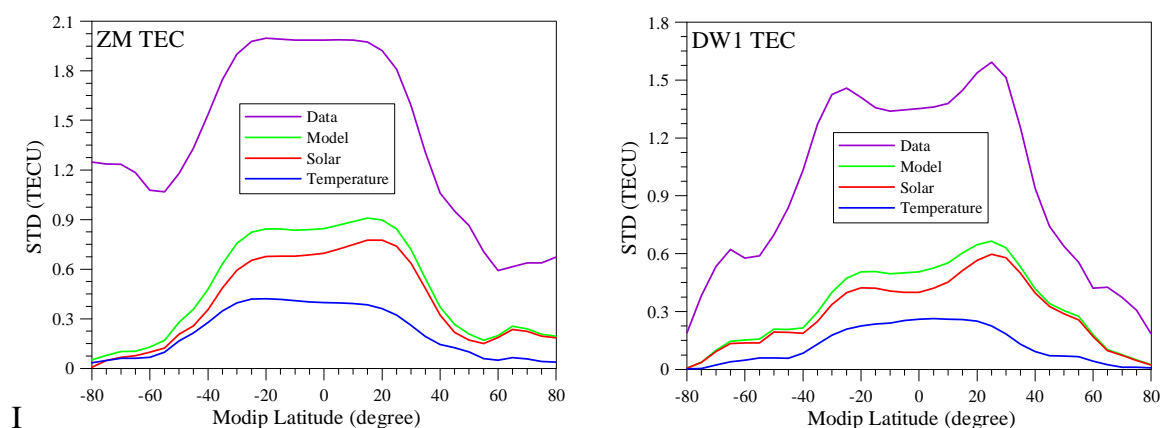
Figure 36 Modip latitude dependence of the standard deviations of ZM TEC (left plot) calculated from the CODE data (magenta), full model (green), solar part of the model (red) and temperature part of the model (blue); (right plot) the same as the upper plot but for the standard deviations of DW1 TEC.

In order to compare the regression model with the TEC data variability and also to assess the relative effectiveness of the temperature and F10.7 impact on the TEC variability we calculate the STD of all mentioned components. The results are presented in Figure 36. They reveal that: (i) the presented linear regression model describes almost half of the real variability of the global TEC and (ii) the stratospheric temperature (i.e. lower atmospheric forcing) impact is almost half of that from the F10.7 (i.e. external forcing related to the photo-ionization). In order to understand better the above conclusions we remind that the regression model includes only day-to-day variability of F10.7 and temperature (i.e. wind also). It is worth nothing that the forcing from below by tides and GWs is not considered. Having in mind also that the geomagnetic activity is not included in the model then it is understandable why the model can describe only half of the real TEC variability. The contribution of the temperature dependence to the TEC variability is only half of that related to F10.7 but is not negligible and have to be included in the modelling the global TEC.

7. Further steps

As a next step we propose to build a new global TEC model for short-term prediction where the impact of stratospheric temperature is included as well.

References

Andonov B., P. Muhtarov, and I. Kutiev (2004), Analogue model, relating Kp index to solar wind parameters, *J. Atmos. Sol.- Terr. Phys.*, 66, 927-932.

Andonov, B., P. Mukhtarov, and D. Pancheva (2011), Empirical model of the TEC response to the geomagnetic activity over the North American region, *Adv. Space Res.*, v. 48, pp. 1041-1048, doi:10.1016/j.asr.2011.05.007.

Funke, B., M. López-Puertas, D. Bermejo-Pantaleón, M. García-Comas, G. P. Stiller, T. von Clarmann, M. Kiefer, and A. Linden (2010), Evidence for dynamical coupling from the lower atmosphere to the thermosphere during a major stratospheric warming, *Geophys. Res. Lett.*, 37, L13803, doi:10.1029/2010GL043619

Huang, C.Y., S.H. Delay, P.A. Roddy, E.K. Sutton, and R. Stoneback (2012), Longitudinal structures in the equatorial ionosphere during deep solar minimum, *J. Atmos. Sol.-Terr. Phys.*, 90-91, 156-163, doi:10.1016/j. jastp.2012.04.012.

Jin, H., Y. Miyoshi, D. Pancheva, P. Mukhtarov, H. Fujiwara, and H. Shinagawa (2013), Response of migrating tides to the stratospheric sudden warming in 2009 and their effects on the ionosphere studied by a whole atmosphere-ionosphere model GAIA with COSMIC and TIMED/SABER observations, *J. Geophys. Res.- Space Physics*, v. 118, A10323, doi:10.1029/2012JA017650.

Korenkov, Y. N., et al. (2012), The global thermospheric and ionospheric response to the 2008 minor sudden stratospheric warming event, *J. Geophys. Res.,* 117, A10309, doi:10.1029/2012JA018018.

Kutiev I., P. Muhtarov, Lj. Cander, and M. Levy (1999), Short-term prediction of ionospheric parameters based on autocorrelation analysis, *Annali di Geofisica*, 42, 1, 121-124.

Kutiev, I. and P. Muhtarov (2001), Modeling of midlatitude F-region response to geomagnetic activity, *J. Geophys. Res.*, 106, A8, 15501-15510.

Kutiev, I. and P. Muhtarov (2003), Empirical modeling of global foF2 ionospheric response to geomagnetic activity, *J. Geophys. Res.*, 108, (A1), 1021, doi:10.1029/2001JA009134.

Liu, H.-L., and R. G. Roble (2002), A study of a self-generated stratospheric sudden warming and its mesospheric–lower thermospheric impacts using the coupled TIME-GCM/CCM3, *J. Geophys. Res.*, 107(D23), 4695, doi:10.1029/2001JD001533.

Lu, H., D. Pancheva, P. Mukhtarov, and I. Cnossen (2012), QBO modulation of transient planetary waves during Northern winter, *J. Geophys. Res. – Atmospheres*, v. 117, D09104, doi:10.1029/2011JD016901.

Muhtarov, P. and I. Kutiev (1998), Empirical modeling of ionospheric storms at midlatitudes. *Adv. Space Res.*, 22(6), 829– 835.

Muhtarov P. and I. Kutiev (1999), Autocorrelation method for temporal interpolation and short-term prediction of ionospheric data, *Radio Science*, 34, 2, 459.

Muhtarov, P., I. Kutiev, Lj. Cander, B Zolesi, G. de Franceschi, M. Levy, and M. Dick (2001), European ionospheric forecast and mapping, *Phys. Chem. Earth.*, 25, 5, 347-351.

Muhtarov, P., I. Kutiev, and L. Cander (2002), Geomagnetically correlated autoregression model for short-term prediction of ionospheric parameters, *Inverse Problems*, 18, 49-65.

Mukhtarov, P., Pancheva, D., and Andonov, B. (2009). Global structure and seasonal and interannual variability of the migrating diurnal tide seen in the SABER/TIMED temperatures between 20 and 120 km. *J. Geophys. Res.*, 114, A02309, doi:10.1029/2008JA013759.

Mukhtarov, P., Pancheva, D., and Andonov B. (2010a). Climatology of the stationary planetary waves seen in the SABER/TIMED temperatures (2002-2007). *J. Geophys. Res.*, 115, A06315, doi:10.1029/2009JA015156.

Mukhtarov, P., B. Andonov, C. Borries, D. Pancheva, and N. Jakowski (2010b), Forcing of the ionosphere from above and below during the Arctic winter of 2005/2006, *J. Atmos. Sol.-Terr. Phys.*, v. 72, pp. 193-205.

Mukhtarov, P. and Pancheva, D. (2011), Global ionospheric response to nonmigrating DE3 and DE2 tides forced from below, *J. Geophys. Res. – Space Physics*, v. 116, A05323, doi:10.1029/2010JA016099.

Mukhtarov, P. and D. Pancheva (2012), Thermosphere–ionosphere coupling in response to recurrent geomagnetic activity, *J. Atmos. Sol.-Terr. Phys.*, 90–91, 132–145.

Mukhtarov, P., D. Pancheva, B. Andonov, and L. Pashova (2013a), Global TEC maps based on GNSS data: 1. Empirical background TEC model, *J. Geophys. Res. – Space Physics*, v. 118, 4609–4617, doi:10.1002/jgra.50413.

Mukhtarov, P., D. Pancheva, B. Andonov, and L. Pashova (2013b), Global TEC maps based on GNSS data: 2. Model evaluation, *J. Geophys. Res. – Space Physics*, v. 118, 4594–4608, doi:10.1002/jgra.50412.

Mukhtarov, P., B. Andonov, and D. Pancheva (2013c), Global empirical model of TEC response to geomagnetic activity, *J. Geophys. Res. – Space Physics*, v. 118, 6666-6685, doi:10.1002/jgra.50576.

Mukhtarov, P., D. Pancheva, and B. Andonov: Hybrid model for long-term prediction of the ionospheric global TEC, *J. Atmos. Sol-Terr. Phys.*, 2014 (in press)

Pancheva D. and P. Mukhtarov (1996), A single-station spectral model of the monthly median F-region critical frequency, *Annali di Geofis.*, 39(4), 807-818.

Pancheva D. and P. Mukhtarov (1998), A single station spectral model of the monthly median foF2 and M(3000)F2, *Studia geophys. et geod.*, 42(2), 183-196, DOI: 10.1023/ A:1023361105552.

Pancheva, D.V., P.J. Mukhtarov and B.A. Andonov (2007), Zonally symmetric oscillations in the Northern hemisphere stratosphere during the winter of 2003/2004, *Geophys. Res. Lett.*, v.34, L04807, doi:10.1029/2006GL028666.

Pancheva, D., Mukhtarov, P., Andonov, B., Mitchell, N.J., and Forbes, J.M. (2009a). Planetary waves observed by TIMED/SABER in coupling the stratosphere-mesosphere-lower thermosphere during the winter of 2003/2004: Part 1, Comparison with the UKMO temperature results. *J. Atmos. Sol.-Terr. Phys.*, 71, 61-74.

Pancheva, D., Mukhtarov, P., Andonov, B., Mitchell, N.J., and Forbes, J.M. (2009b). Planetary waves observed by TIMED/SABER in coupling the stratosphere-mesosphere-lower thermosphere during the winter of 2003/2004: Part 2, Altitude and latitude planetary wave structure. *J. Atmos. Sol.-Terr. Phys.*, 71, 75-87,

Pancheva, D., Mukhtarov, P., and Andonov, B. (2009c). Global structure, seasonal and interannual variability of the migrating semidiurnal tide seen in the SABER/TIMED temperatures (2002-2007). *Ann. Geophys.*, 27, 687-703.

Pancheva, D., Mukhtarov, P., and Andonov, B. (2009d). Nonmigrating tidal activity related to the sudden stratospheric warming in the Arctic winter of 2003/2004. *Ann. Geophys.*, 27, 975-987.

Pancheva, D., Mukhtarov, P., Andonov, B., and Forbes, J.M. (2010a). Global distribution and climatological features of the 5-6-day planetary waves seen in the SABER/TIMED temperatures (2002-2007). *J. Atmos. Sol.-Terr. Phys.*, 72, 26-37.

Pancheva, D., Mukhtarov, P., and Andonov, B. (2010b). Global distribution, seasonal and interannual variability of the eastward propagating tides seen in the SABER/TIMED temperatures (2002-2007). *Adv. Space Res.*, 46, 257-274, doi:10.1016/j.asr.2010.03.026.

Pancheva, D. and P. Mukhtarov (2010), Strong evidence for the tidal control on the longitudinal structure of the ionospheric F-region, *Geophys. Res. Lett.*, v. 37, L14105, doi:10.1029/2010GL044039.

Pancheva, D. and P. Mukhtarov (2011a), Atmospheric tides and planetary waves: Recent progress based on SABER/TIMED, in IAGA Special Sopron Book Series 2, *Aeronomy of the Earth's Atmosphere and Ionosphere*, ed. M. Abdu and D. Pancheva, pp. 19-56, doi:10.1007/978-94-007-0326-1.

Pancheva, D. and P. Mukhtarov (2011b), Stratospheric warmings: The atmosphere-ionosphere coupling paradigm, *J. Atmos. Sol-Terr. Phys.*, v. 73, pp. 1697-1702, doi:10.1016/j.jastp.2011.03.066.

Pancheva, D. and P. Mukhtarov (2012a), Global response of the ionosphere to atmospheric tides forced from below: Recent progress based on satellite measurements, *Space Sci. Rev.*, v. 168(1-4), pp. 175-209, DOI:10.1007/s11214-011-9837-1.

Pancheva, D. and P. Mukhtarov (2012b), Planetary Wave Coupling of the Atmosphere-Ionosphere System during the Arctic Winter of 2008/2009, *Adv. Space Res.,* v. 50, pp. 1189-1203.

Pancheva, D. and P. Mukhtarov (2012c), Global Response of the Ionosphere to Atmospheric Tides Forced from Below: Recent progress Based on Satellite Measurements, in *Dynamic Coupling Between Earth's Atmospheric and Plasma Environments*, Bosinger, T., J. LaBelle, H.J. Opgenoorth, J.-P. Pommereau, K. Shiokawa, S. Solomon, and R.A. Treumann, (Eds.),v. 42, pp. 175-209, ISBN 978-1-4614-5676-6, Springer.

Pancheva, D., Y. Miyoshi, P. Mukhtarov, H. Jin, H. Shinagawa, and H. Fujiwara (2012), Global response of the ionosphere to atmospheric tides forced from below: Comparison between

COSMIC measurements and simulations by Atmosphere-Ionosphere Coupled Model GAIA, *J. Geophys. Res. – Space Physics*, v. 117, A07319, doi:10.1029/2011JA017452.

Pancheva, D., P. Mukhtarov and A.K. Smith (2013), Climatology of the migrating terdiurnal tide (TW3) in SABER/TIMED temperatures, *J. Geophys. Res. – Space Physics*, v. 118, doi:10.1002/jgra.50207.

Pancheva, D. and P. Mukhtarov (2014) Winter-time dependence of the global TEC on the stratospheric temperature and solar radiation, *Adv. Space Res.*, (submitted)

Rawer, K. (1963), In: Landmark, B. (Ed.), *Meteorological and Astronomical Influences on Radio Wave Propagation*, Pergamon Press, Oxford, 221–250.

Shepard, D. (1968), A two-dimensional interpolation function for irregularly-spaced data, *ACM '68 Proc.,* pp. 517 – 524, ACM New York, NY, doi:10.1145/800186.810616.